

https://dspace.org/

A systematic study on the use of the sol-gel synthetic method for lithium manganese oxide-based cathode materials

Muntswu, Zwivhuya

2024-09
University of the Witwatersrand, Johannesburg
https://hdl.handle.net/10539/45267

Muntswu, Zwivhuya. (2024). A systematic study on the use of the sol-gel synthetic method for lithium manganese oxide-based cathode materials. [Master's dissertation, University of the Witwatersrand, Johannesburg]. WIReDSpace. https://hdl.handle.net/10539/45267

Downloaded from a DSpace repository. https://dspace.org/

A systematic study on the use of the sol-gel synthetic method for lithium manganese oxide-based cathode materials



MSc Dissertation

By

Zwivhuya Muntswu

September 2024

UNIVERSITY OF THE WITWATERSRAND JOHANNESBURG 1922 2022

School of CHEMISTRY

Declaration

I declare that this dissertation is my own, unaided work. It is being submitted for the Degree of Master of Science at the University of the Witwatersrand, Johannesburg. It has not been submitted before for any degree or examination at any other University.

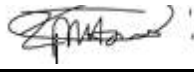

(Signature of candidate)

06 September 2024

Supervisor : Professor David G. Billing

Co-supervisor : Professor Caren Billing

Co-Supervisor : Professor Ernst E Ferg

Abstract

This dissertation investigated the synthesis of two lithium manganese oxide-based cathode materials ($Li_{1.03}Mn_{1.97}O_4$ and $LiAl_{0.4}Mn_{1.6}O_4$) using the sol-gel method and probing the phase transitions during the synthesis. The sol-gel synthetic method involved dissolving stoichiometric amounts of lithium nitrate, manganese nitrate hydrate, and citric acid in distilled water forming an aqueous solution. The starting precursor materials were dried at 140 °C which formed a crystalline phase of Δ-Aqua-S-citrato(2-)-manganese(II) with an orthorhombic crystal system and *P*222 space group.

The thermal behaviour of the precursor was explored to understand the effects of calcination/annealing temperatures. Thermal analysis of precursors prepared using nitrate salts with a 1:1 total metal ion to citric acid ratio displayed thermal stability to temperatures higher than 380 °C with the formation of a final metal oxide after 70% mass loss due to the decomposition of the organic and nitrate materials. However, when increasing the concentration of the complexing agent, an increase in material decomposition due to an increase in organic material is seen. The precursor materials prepared with a lower complexing agent concentration result in materials that have thermal instability when exposed to high temperatures. Thermal analysis of $Li_{1.03}Mn_{1.97}O_4$ and $LiAl_{0.4}Mn_{1.6}O_4$ prepared using acetate salts as starting materials shows material decomposition at high temperature of ~600 °C

Calcining both undoped and Al-doped nitrate precursors at moderate temperatures (380 °C to 500 °C) resulted in the formation of $Li_{1.03}Mn_{1.97}O_4$ and $LiAl_{0.4}Mn_{1.6}O_4$ with a pure cubic spinel structure and an *Fd*-3*m* space group, however, increasing the calcining temperature to 800 °C for the undoped nitrate-based precursor revealed an impurity phase formation relating to dilithium manganese oxide with a monoclinic crystal system. On the other hand, calcining acetate-based precursors at moderate temperatures (380 °C to 500°C) results in metal oxides with low crystallinity compared to metal oxides prepared with nitrate-based precursors. Calcining acetate-based precursors at 800 °C was more favourable since they form the desired metal oxides without any impurities which might imply structural phase stability at high temperatures.

The local and average crystallographic structures (via PDF and XRD respectively) of various nitrate-based metal oxides were investigated, where a good agreement between collected data and a calculated structural model revealed the formation of a cubic spinel structure of space group *Fd*-3*m*. $Li_{1.03}Mn_{1.97}O_4$ and $LiAl_{0.4}Mn_{1.6}O_4$ metal oxides were achieved from calcining precursors at moderate temperatures of 380 °C and 450 °C. The PDF high r-value signal displays a good fit which confirms to the average structure data information where the r-value signal which correspond to the local structure refinements have a minor discrepancy when fitted with a cubic spinel of space group *Fd*-3*m*.

Acknowledgement

- I acknowledge the support of my supervisors Prof David Billing, Prof Ernst Ferg and Prof Caren Billing for their amazing supervision, guidance, and support throughout the past years.
- Many thanks to my research group members for their guidance, advice and helpful discussions. Thank you Dr Sikhumbuzo Masina, Dr Gugulethu Nkala, Dr Mathias Kiefer.
- I thank the UYilo e-Mobility Technology Innovation Programme for their financial support.
- I would like to extend my gratitude to my mom, Mrs Gladys Muntswu, and dad, Mr Samuel Muntswu for your continuous support throughout this journey. Thank you.
- My brother Mr Thanyani Muntswu and your wife Mrs Sedzani Muntswu, thank you for always pushing me to work hard and continue to dream big.
- My siblings, Mr Rolivhuwa Muntswu, Miss Mukhethwa Muntswu and Miss Fulufhelo Muntswu, thank you for your support and wonderful memories we had. I am truly grateful.
- My cousin Mr Phathutshedzo Ndou, thank you for taking care of me over this years, you have always been a brother and a friend to me. I am thankful to you for always being there for me.

Table of contents

Declaration i

Abstract ii

Acknowledgement iii

Table of contents iv

List of figures vii

List of Tables x

List of Abbreviations xi

Chapter 1: Introduction 1

1.1. Project overview 1

1.2. Aims of the study 2

1.3. Dissertation outline 3

1.4. References 3

Chapter 2: Literature review 5

2.1. Introduction to lithium-ion batteries 5

2.1.1. Safety management system of LIBs 7

2.2. Cathode materials 9

2.2.1. The historical lithium cobalt oxide ($LiCoO_2$) 10

2.2.2. The interesting lithium manganese oxide ($LiMn_2O_4$) 11

2.2.3. The famous lithium-ion phosphate ($LiFePO_4$) cathode material 13

2.2.4. $LiFeSO_4F$ as cathode material 14

2.2.5. Effects of cationic doping on cathode materials 14

2.3. Synthetic methods 15

2.3.1. Sol-gel process 17

2.3.2. Solid-state method 19

2.3.3. Co-precipitation 20

2.3.4. Hydrothermal reaction 20

2.3.5. Spray pyrolysis 21

2.3.6. Combustion method 22

2.4. Flow cell design 23

2.5. References 24

Chapter 3: Experimental methods 30

3.1. Materials synthesis 30

3.2. Characterization techniques 31

3.2.1. Thermal analysis 31
3.2.2. Powder X-ray diffraction 32
3.2.3. Rietveld refinement and pair distribution function analysis 33
3.3. Theory on characterization techniques 34
3.3.1 Simultaneous thermal analysis 34
3.3.2. Powder X-ray diffraction (PXRD) 35
3.3.3. Synchrotron techniques 37
3.3.4. Rietveld refinement 38
3.3.5. Pair Distribution Function (PDF) 39
3.4. References 41
Chapter 4: A detailed investigation on the decomposition of the precursor materials 44
4.1. Investigation of precursors prepared using nitrate salts 44
4.1.1. Laboratory XRD of Undoped precursor 44
4.1.2. Laboratory XRD of Al-doped precursor. 48
4.1.3 STA analysis of Undoped starting material precursor 49
4.1.4. STA analysis of Al-doped starting precursor 53
4.1.5. The effect of calcining nitrate precursors at 270 °C and 300 °C 55
4.2. Investigation of precursors prepared using acetate salts 56
4.2.1. Laboratory XRD of precursors 56
4.2.2. STA analysis of precursors 57
4.2.3. The effect of calcining acetate precursors at 270 °C and 300 °C 58
4.3. Conclusion 59
4.5. References 60
Chapter 5: Understanding the effect of calcining precursors at various temperatures 62
5.1. Laboratory X-ray diffraction analysis of precursors calcined at moderate temperatures (up to 500 °C) 62
5.1.1. Undoped lithium manganese oxide prepared using metal nitrate salts 62
5.1.2. Al-doped lithium manganese oxide prepared using metal nitrate salts 69
5.1.3. Undoped and Al-doped lithium manganese oxide prepared using metal acetate salts . 73
5.2. Laboratory X-ray diffraction analysis of precursors calcined at high temperatures (600- 800 °C) 75
5.2.1. Undoped and Al-doped lithium manganese oxide prepared using metal nitrate salts .. 75
5.2.2. Undoped and Al-doped lithium manganese oxide prepared using metal acetate salts . 77
5.3. Conclusion 80
5.4. References 80
Chapter 6: Investigating crystallographic structure using local and average structure refinements 83

6.1. Synchrotron X-ray diffraction analysis of metal oxide produced at moderate temperatures 83
6.1.1. Undoped lithium manganese oxide 83
6.1.2. Al-doped lithium manganese oxide 85
6.2. Pair distribution function analysis 88
6.2.1. Undoped lithium manganese oxide PDF analysis 88
6.2.2. Al-doped lithium manganese oxide PDF analysis 91
6.3. Conclusion 92
6.4. References 93
Chapter 7: Conclusion 94
Appendices 96
Appendix 1: Furnace Calibration 96
Appendix 2: Flow cell design 98
References 101

List of figures

Figure 1.1: BMW i3 electric vehicle captured at OR Tambo international airport in South Africa during the launch of a charging station [3]. 1
Figure 2.1: Schematic presentation of lithium-ion battery illustrating the working principle of charging (purple) and discharging (red). 5
Figure 2.2: Ragone plot comparing different batteries in terms of specific power and energy (Adapted from [11]). 7
Figure 2.3: Different battery designs: (a.) Cylindrical cells, (b.) Prismatic cell, (c.) Button cells and (d.) pouch cells [17]. 8
Figure 2.4: Layered Crystal structure of $LiCoO_2$ with R-3m space group. 10
Figure 2.5: Crystal structure of $LiMn_2O_4$ with space group Fd-3m. 11
Figure 2.6: The pathways in which Li-rich layered oxide is formed from the spinel oxide structure with transition metal migration (TM) [32]. 12
Figure 2.7: An olivine $LiFePO_4$ crystal structure with Pnma space group. 14
Figure 2.8: Various synthesis methodologies used to manufacture cathode materials for lithium-ion batteries, (Adapted from [50]) 16
Figure 2.9: A schematic of the sol-gel method. (Adapted from [52]). 18
Figure 2.10: A typical schematic representation of the solid-state reaction method 19
Figure 2.11: Flow chart of the co-precipitation method 20
Figure 2.12: Schematic representation of the hydrothermal synthesis 21
Figure 2.13: Schematic representation of combustion synthesis. 22
Figure 2.14: An example of a flow-cell components diagram for variable temperature measurement showing how they fit [72]. 24
Figure 3.1: Schematic of how the sol-gel synthesis method was utilized. 30
Figure 3.2: PerkinElmer STA 6000 used for thermal analysis with the bottom right picture showing the compact furnace. 31
Figure 3.3: Empty crucible STA data heated from 30 °C to 800 °C at 5 °C/min in air. 32
Figure 3.4: Bruker D2 Phaser diffractometer and its front when opened. 33
Figure 3.5:Heat flow plots at different heating rates of 5 °C/min, 10 °C/min, and 15 °C/min with the endothermic peaks shown as negative heat flow and exothermic peaks shown as positive heat flow [3]. 35
Figure 3.6: Schematic representation of information content of a powder pattern [7]. 37
Figure 3.7: Schematic representation of Synchrotron technique. 38
Figure 3.8: Schematic representation of converting powder diffraction data to the pair distribution function. (a) Integration data, (b) normalized scattering intensity S(Q), (c) normalised reduced total scattering structure function F(Q), and (d) atomic pair distribution function (PDF) G(r) with Q being the scattering vector. Adapted from [25]. 40
Figure 4.1: Powder X-ray diffraction patterns of precursors for undoped lithium manganese oxide prepared using nitrate salts and differing $[M_T]$:[Cit] as indicated. Major discrepancies between the patterns are indicated by ★ and ▲. 45
Figure 4.2: Chemical structure of Δ-Aqua-S-citrato(2-)-manganese(II) [4]. 46
Figure 4.3:Rietveld refinement of the precursor with $[M_T]$:[Cit] = 1:1.667. The pattern obtained from the experimental data (yobs) is shown in blue, the calculated model (ycalc) in red, and difference plot which represents the difference between the observed and the calculated model (yobs-ycalc) in black. The tick marks in green shows the calculated peak positions correspond to orthorhombic phase for Δ-aqua-S-citrato(2-)-manganese(II). 46
Figure 4.4:Rietveld refinements of precursors with $[M_T]$: [Cit] of (a.) 1:1, (b.) 1:0.833, (c.) 1:0.667 and (d) 1:0.5. The tick marks correspond to orthorhombic phase for Δ-aqua-S-citrato(2-)-manganese(II). The peak indicated by ★ corresponds to that in Fig. 4.1. 47
Figure 4.5: Powder X-ray diffraction patterns of the dried precursor of Al-doped lithium manganese oxide. 49

Figure 4.6: DTA (red) and TGA (blue) plots of the precursor for undoped lithium manganese oxide with [M_T]:[Cit] = 1:1.667. 50
Figure 4.7: DTA and TGA plots of the precursors for undoped lithium manganese oxide synthesised with [M_T]:[Cit] of (a) 1:1, (b) 1:0.833 and (c) 1:0.667. 52
Figure 4.8: DTA and TGA plots of Al-doped lithium manganese oxide precursors synthesised with [M_T]:[Cit] of (a) 1:1.667 (b) 1:1 and (c) 1:0.667. 54
Figure 4.9: X-ray diffraction patterns of nitrate-based precursors prepared using [M_T]:[Cit] = 1:1 calcined at (a) 270 °C and (b) 300 °C for 5 hours in air with │ being the tick marks for lithium manganese oxide spinel structure. 55
Figure 4.10: Rietveld refinement of a dried acetate-based precursors with [M_T]:[Cit] = 1:1 for (a.) undoped and (b.) Al-doped precursors. The tick marks correspond to orthorhombic phase for Δ-aqua-S-citrato(2-)-manganese(II). 57
Figure 4.11: DTA and TGA plots for acetate-based precursors synthesised using [M_T]: [Cit] = 1:1 as for (a) undoped and (b) Al-doped precursors. 58
Figure 4.12: X-ray diffraction patterns of acetate-based precursors prepared using [M_T]: [Cit] = 1:1 and calcined at (a) 270 °C and (b) 300 °C for 5 hours in air. 59
Figure 5.1: PXRD diffractograms of $Li_{1.03}Mn_{1.97}O_4$ prepared with 1: 1.667 [M_T]: [Cit] by calcining the precursor at different temperatures for 5 hours in the air. 63
Figure 5.2: PXRD diffractograms of $Li_{1.03}Mn_{1.97}O_4$ prepared with 1: 1 [M_T]: [Cit] calcined at different temperatures for 5 hours in the air. 64
Figure 5.3: Rietveld refinement fitting the $Li_{1.03}Mn_{1.97}O_4$ cubic spinel crystal structure (space group Fd-3m) to the XRD patterns for samples with [M_T]:[Cit] = 1:1 calcined at (a) 380 °C, (b) 400 °C, (c) 450 °C and (d) 500 °C in air. 65
Figure 5.4: The Rietveld refinement of $Li_{1.03}Mn_{1.97}O_4$ with space group Fd-3m synthesised using [M_T]:[Cit] = 1:1; Rwp= 1.13, Rexp=1.04 and GOF= 1.09. 67
Figure 5.5: Rietveld refinement fitting the $Li_{1.03}Mn_{1.97}O_4$ cubic spinel crystal structure (space group Fd-3m) to the XRD pattern for samples with [M_T]:[Cit] = 1:1.667 calcined at (a) 380 °C, (b) 400 °C, (c) 450 °C and (d) 500 °C in air 68
Figure 5.6: The samples prepared using [M_T]:[Cit] of 1:0.833 and 1:0.667 heated to 380 °C and calcined for 5 hours in air. 69
Figure 5.7: PXRD patterns of $LiAl_{0.4}Mn_{1.6}O_4$ prepared with [M_T]:[Cit] of 1:1.667, 1:1 and 1:0.667 calcined at different temperatures for 5 hours in the air. 70
Figure 5.8: Rietveld refinements fitted with $LiAl_{0.4}Mn_{1.6}O_4$ cubic spinel crystal structure (space group Fd-3m) to the XRD pattern for [M_T]:[Cit] of (a) 1:0.667, (b) 1:1 and (c) 1:1.667 sample calcined at 380 °C in air. 71
Figure 5.9: Rietveld refinements fitted with $LiAl_{0.4}Mn_{1.6}O_4$ cubic spinel crystal structure (space group Fd-3m) to the XRD pattern for [M_T]:[Cit] of (a) 1:0.667, (b) 1:1 and (c) 1:1.667 samples calcined at 450 °C in air. 72
Figure 5.10: Rietveld refinement of $LiAl_{0.4}Mn_{1.6}O_4$ with space group Fd-3m; Rwp = 1.18, Rexp = 1.09 and GOF = 1.08. The precursor made with [M_T]:[Cit] = 1:1 was calcined at 380 °C for 10 hours. 73
Figure 5.11: Rietveld refinement of $Li_{1.03}Mn_{1.97}O_4$ calcined at (a) 400 °C and (b) 500 °C, and of $LiAl_{0.4}Mn_{1.6}O_4$ calcined also at (c) 400 °C and (d) 500 °C for [M_T]:[Cit] = 1:1 using the cubic spinel crystal structure (space group Fd-3m). 74
Figure 5.12: Rietveld refinement of $Li_{1.03}Mn_{1.97}O_4$ prepared with [M_T]:[Cit] = 1:1 and calcined at (a) 600 °C, (b) 700 °C and (c) 800 °C in air prepared with nitrate precursor. 75
Figure 5.13: Rietveld refinement of $LiAl_{0.4}Mn_{1.6}O_4$ prepared with [M_T]:[Cit] = 1:1 and calcined at (a) 600 °C, (b) 700 °C and (c) 800 °C in air prepared with nitrate precursor. 76
Figure 5.14: Rietveld refinement of $Li_{1.03}Mn_{1.97}O_4$ prepared with [M_T]:[Cit] = 1:1 and calcined at (a) 600 °C, (b) 700 °C and (c) 800 °C in air prepared with acetate precursor 78
Figure 5.15: Rietveld refinement of $LiAl_{0.4}Mn_{1.6}O_4$ prepared with [M_T]: [Cit] = 1: 1 and calcined at (a) 600 °C, (b) 700 °C and (c) 800 °C in air prepared with acetate precursor 79
Figure 5.16: Comparison of diffraction patterns for $Li_{1.03}Mn_{1.97}O_4$ prepared using acetate and nitrate salts and calcined at 800 °C for 5 hours in air. 80

Figure 6.1: Diffraction patterns of $Li_{1.03}Mn_{1.97}O_4$ prepared with a [M_T]:[Cit] = 1:1 and calcined at 380 °C or 450°C for 5 hours in the air, with (a.) SPXRD and (b.) Laboratory XRD data. Peaks indicated by ▲ highlight some of the peaks which are barely visible by lab XRD, but are clearly visible by SXRD. 84
Figure 6.2: Rietveld refinements of $Li_{1.03}Mn_{1.97}O_4$ prepared with [M_T]: [Cit] =1: 1 and calcined at (a) 380 °C and (b) 450 °C displaying the cubic spinel crystal structure (space group *Fd-3m*). 85
Figure 6.3: Diffractograms of $LiAl_{0.4}Mn_{1.6}O_4$ prepared with [M_T]: [Cit] = 1:1 and calcined at 380 °C or 450 °C for 5 hours in the air with (a.) SPXRD and (b.) Laboratory XRD, with ★ representing undefined peaks. 86
Figure 6.4: Rietveld refinements of the diffraction patterns for $LiAl_{0.4}Mn_{1.6}O_4$ prepared with [M_T]:[Cit] of 1:1 and calcining the precursor at (a) 380 °C, (b) 450 °C. The peak indicated by ★ corresponds to that in Fig. 6.3 87
Figure 6.5: Small box refinements of PDF data for $Li_{1.03}Mn_{1.93}O_4$ prepared from [MT]:[Cit] = 1: 1 with space group Fd-3m of a cubic spinel crystal structure with samples calcined at (a) 380 °C, and (b) 450 °C. The absence of phase correction on the peaks means they are displayed ~0.4 Å lower than the structural values. 90
Figure 6.6: Small box refinements of $LiAl_{0.4}Mn_{1.6}O_4$ prepared from 1:1 total metal ion to citric acid ratio with space group Fd-3m of a cubic spinel crystal structure with samples calcined at (a) 380 °C, (b) 450 °C, the absence of phase correction on the peaks are displayed ~0.4 lower than the structural values. 92
Figure A1: Tube furnace calibration curve showing the true values (Set temperature) and ideal values (desired temperature) 97
Figure A2.1: A flow-cell design used with associated components/ parts [1]. 98
Figure A2.2: Flow cell Block 1 design 99
Figure A2.3: Flow cell Block 2 design 99
Figure A2.4: Flow cell rod design 100
Figure A2.5: A flow cell design incorporating the block designs and a rod 100

List of Tables

Table 2.1:Comparison of various synthesis routes for cathode materials [50]. 17
Table 4.1: The [M_T]:[Cit] used to prepare undoped precursor materials using the sol-gel method. 44
Table 4.2: Refined structural parameters of the undoped precursor material Rwp, Rexp and GOF are the statistical fit parameters described in chapter 3 section 3.3.4.. 48
Table 4.3: The [M_T]:[Cit] used to prepare Al-doped precursor materials using the sol-gel method. 49
Table 4.4: Refined structural parameters of acetate-based precursor materials with [M_T]:[Cit] = 1:1 fitted using the Δ-aqua-S-citrato(2-)-manganese(II) system with space group *P*222..... 56
Table 5.1: Refined room temperature structural parameters of $Li_{1.03}Mn_{1.97}O_4$ using the cubic spinel model (space group Fd-3m). Samples were produce using [M_T]:[Cit] = 1:1 and calcining the precursors at various temperatures. 66
Table 5.2: Refined room temperature structural parameters of calcined $Li_{1.03}Mn_{1.97}O_4$ (synthesised using [M_T]:[Cit] = 1:1.667) using the cubic spinel model (space group *Fd*-3*m*). 67
Table 5.3: Refined room temperature structural parameters of $LiAl_{0.4}Mn_{1.6}O_4$ calcined at 380 and 450 °C fitted using the cubic spinel model (space group *Fd*-3*m*). 72
Table 5.4: Refined room temperature structural parameters of calcined metal oxides of $Li_{1.03}Mn_{1.97}O_4$. and $LiAl_{0.4}Mn_{1.6}O_4$ with space group *Fd*-3*m*. 73
Table 5.5: Refined room temperature structural parameters of calcined metal oxides of $Li_{1.03}Mn_{1.97}O_4$. and $LiAl_{0.4}Mn_{1.6}O_4$ with space group *Fd*-3*m* of a cubic model. 77
Table 5.6: Refined room temperature structural parameters of calcined metal oxides of $Li_{1.03}Mn_{1.97}O_4$ and $LiAl_{0.4}Mn_{1.6}O_4$ with space group *Fd*-3*m* of a cubic model. 79
Table 6.1: Lattice parameters and crystallite size of 1:1 [M_T]: [Cit] calcined at various temperatures obtained from Rietveld refinements. 85
Table 6.2: Lattice parameters and crystallite size of 1:1 [M_T]: [Cit] obtained from Rietveld refinements. 87
Table 6.3: Lattice parameters and crystallite size of 1:1 total metal ion to citric acid ratio of $Li_{1.03}Mn_{1.97}O_4$. .. 91
Table 6.4: Lattice parameters and Rw for $LiAl_{0.4}Mn_{1.6}O_4$ synthesised using 1:1 total metal ion to citric acid ratio. 91

List of Abbreviations

$[M_T]$:[Cit]	: Concentration of total metal ion to citric acid ratio
DTA	: Differential thermal analysis
EXAFS	: Extended X-ray absorption fine structure
EV	: Electric vehicle
GOF	: Goodness of fit
LIB	: Lithium-ion battery
LMO	: $LiMn_2O_4$
PDF	: Pair distribution function
PXRD	: Powder X-ray diffraction
SPXRD	: Synchrotron powder X-ray diffraction
STA	: Simultaneous thermal analysis
TGA	: Thermal gravimetric analysis
VT-PXRD	: Variable temperature X-ray diffraction
XRD	: X-ray diffraction

Chapter 1: Introduction

1.1. Project overview

Research in battery materials is a major focus area as this is a key to access to energy which remains one of the biggest obstacles in world's energy-sustainability. Energy storage devices can help maintain the supply and demand of energy for electric vehicles (Fig.1.1) as well as for electric grid applications. Many studies have been aimed at low-cost battery materials containing earth-abundant elements which must be efficient and stable so that can be used towards solving energy crisis. The global atmospheric carbon dioxide (CO_2) levels have been steadily increasing as human industrialisation and energy usage have increased, however, efforts have been made towards CO_2 mitigation/ decarbonisation which has led to the development of electric vehicles (EVs) [1, 2].



Figure 1.1: BMW i3 electric vehicle captured at OR Tambo international airport in South Africa during the launch of a charging station [3].

Lithium-ion batteries currently have an unmatched combination of high energy and power density at this stage, making them the most popular technology of choice for hybrid/full electric vehicles [4]. When expanding the applications (such as portable electronics, cell phones, laptops, solar power backup storage) of state-of-the-art lithium-ion batteries, these have resulted in ongoing efforts to reduce the manufacturing, formulation and raw material costs [5]. Studies have shown that development of cobalt-free lithium manganese oxides as cathode materials is one of the greatest developments as these materials have the potential to reduce the manufacturing cost of the overall cathode materials. Manganese based oxides

have gained a lot of interest as the amount of manganese available in South Africa (about 80 % of the world reserves) is sufficient to power a global fleet of automobiles hence the continuous research to improve its application [5].

1.2. Aims of the study

The broad aim of this project is to successfully synthesize lithium manganese oxide as well as understanding the effect of adding a dopant (Al) on its structure. The starting materials used are carefully selected due to their sustainability (by using earth-abundant elements) and cost-effective options and the sol-gel synthetic route will be explored. Part of the study will be to carefully track the effect of calcination temperature on the phase formed when the precursor (dried gel) materials are exposed to different temperatures using simultaneous thermal analysis (a combination of thermal gravitational analysis and differential thermal analysis) and powder X-ray diffraction, where a high degree of reproducibility can be achieved to understand the characteristics of the transition stages during the synthesis process of typical commercial cathode materials. More specifically the objectives are:

- To investigate the conditions used in the sol-gel synthesis for producing $Li_{1.03}Mn_{1.97}O_4$ and $LiAl_{0.4}Mn_{1.6}O_4$ when using metal nitrate or acetate salts as starting materials.
- To study the effect of using Al as dopant with regards to the structural stability and phase purity of product.
- To investigate the structural changes and crystallographic characteristics when calcining the cathode materials in the temperature range from 380 to 800 °C and compare the results when using metal nitrate and acetate salts as starting materials.
- To assess the local and average structure characteristics of the final product formed at moderate temperatures (i.e. 380 and 450 °C).
- To investigate the optimum total metal ion to citric acid concentration ratio used. The drive is to enable in-situ variable temperature X-ray diffraction measurements using capillaries thus the minimum decomposition/mass loss is required.

In this project, undoped and Al-doped precursors and final products of lithium manganese oxide with cubic spinel structure will be studied by ex-situ powder X-ray studies. Aluminium was used as a dopant since this has been commonly used to enhance the structural and thermal stability of the material. The sol-gel synthetic method will be investigated using different starting materials which include the metal nitrate or acetate salts of interest while using citric acid as a complexing agent. Nitrate salts have the potential to form these oxide materials at moderate temperatures which might reduce the cost of the cathode material due to its high solubility in water and can decompose at moderate temperatures (i.e. 500 °C).

Lithium manganese oxide of a spinel structure has the stoichiometry of $LiMn_2O_4$, which is one of the common materials for lithium-ion cells. In this project we will synthesize cathode materials with a slightly Li-rich form, $Li_{1.03}Mn_{1.97}O_4$, and a doped form, $LiAl_{0.4}Mn_{1.6}O_4$. These stoichiometric ratios will be used as they have been reported to retain the same crystal

structure as $LiMn_2O_4$ and revealed a stable electrochemical performance with Al-dopant used due to its ability to form cathode material that have phase stability when calcined at high temperatures [6].

1.3. Dissertation outline

This dissertation mainly focuses on understanding the synthesis method of the spinel-based lithium manganese oxide while tracking the phase transitions during the product formation:

- **Chapter two** is aimed at reviewing the literature on lithium-ion battery cathode materials as well as raise awareness on the importance of safety measures that need to be understood before producing lithium-ion batteries. Different cathode materials and the effects of using dopants have been addressed while unpacking different synthetic methods that can be utilized when preparing lithium-ion battery cathode materials.
- **Chapter three** introduces the materials preparation steps that include the experimental procedure and the synthetic method that was explored when preparing these cathode materials for lithium-ion batteries. The detailed background information on the materials characterization techniques that have been used was discussed, introducing the simultaneous thermal analysis, powder X-ray diffraction techniques, and high-resolution synchrotron X-ray diffraction and pair distribution function.
- **Chapter four** investigates the starting material precursor (the dried gel) by utilizing powder X-ray diffraction of different metal oxides, followed by the thermal analysis which is aimed at explaining the direct relationship between the chemistry of the precursor and the phase formation of the lithium manganese oxide materials by analysing how the material decomposes to form its final metal oxide material.
- **Chapter five** examines the powder X-ray diffraction of the final metal oxide following the simultaneous thermal analysis results, where the cathode materials were calcined at different temperatures to study the effects of calcination temperatures on the formation and stability of the material.
- **Chapter six** looks at the synchrotron X-ray diffraction of calcined materials as well as the pair distribution function, thus the relationship between the local and average structure of these metal oxides were considered.
- **Chapter seven** discusses the overall conclusions of this work and also looks at some proposed future work.

1.4. References

[1] O. A. M. Akinbami, S. R. Oke, and M. O. Bodunrin, “The state of renewable energy development in South Africa: An overview,” *Alexandria Engineering Journal,* vol. 60, no. 1, pp. 5077-5093, 2021.

[2] R. Lindsey, “Climate change: Atmospheric Carbon Dioxide,” 7 October 2021. [Online]. Available: http://www.climate.gov/media/13611. [Accessed 2 February 2022].

[3] H. Philander, “press BMW group,” Press release, 1 November 2019. [Online]. Available: http://www.press.bmwgroup.com/south-africa/article/detail/T0302281 EN/airports-compony-south-africa-and-bmw-south-africa-launch-electric-vehicle-charging-stations?language=en. [Accessed 22 March 2022].

[4] G. Zubi, R. Dufo-Lopez, M. Carvalho and G. Pasaoglu, “The lithium-ion battery: State of the art and future perspectives,” *Renewable and Sustainable Energy Reviews,* vol. 89, no. 1, pp. 292-308, 2018.

[5] N. Nitta, F. Wu, T. J. Lee, and G. Yushin, “Li-ion battery materials: present and future,” *Materials Today,* vol. 18, pp. 252-264, 2015.

[6] P. Singh, A. Sil, M. Nath and S. Ray, “Preparation and characterization of lithium manganese oxide spinel $Li_{1.03}Mn_{1.97}O_4$ doped with Mg and Fe,” *Physica B,* vol. 34, pp. 622-628, 2010.

Chapter 2: Literature review

2.1. Introduction to lithium-ion batteries

The demand for energy storage devices has grown steadily over the years as e-mobility solutions (i.e. electric cars, buses, motorbikes, e.t.c), portable devices and light duty electronics are being developed. The research in electro-chemical energy storage devices (fuel cells, batteries, and supercapacitors) is increasing to balance the rise in the amount of sustainable power demand for the next generation applications [1, 2].

Batteries are broadly classified into two types namely: primary (non-rechargeable) and secondary (rechargeable) batteries. In primary batteries, the electrochemical reaction is irreversible and leads to the disposal of the battery after discharge with alkaline Leclanche cells and zinc chloride cells as examples. Secondary batteries are referred to as "rechargeable" where their electrochemical reaction can be reversible upon applying a reverse current shown in Fig 2.1 [3].

Cells (the smallest unit of a battery) consists of two electrodes: the cathode (positive) and the anode (negative), that are separated by an electrolyte and a separator (Fig.2.1). The separator provides the battery with internal insulation that prevents the battery from short-circuiting, and the electrolyte enables the direct flow of ions from cathode to anode while preventing the direct flow of electrons between the electrode materials [4]. These batteries produce electrical current when the anode and the cathode are connected by an external circuit allowing the electrons to migrate from the anode to the cathode electrode [4].

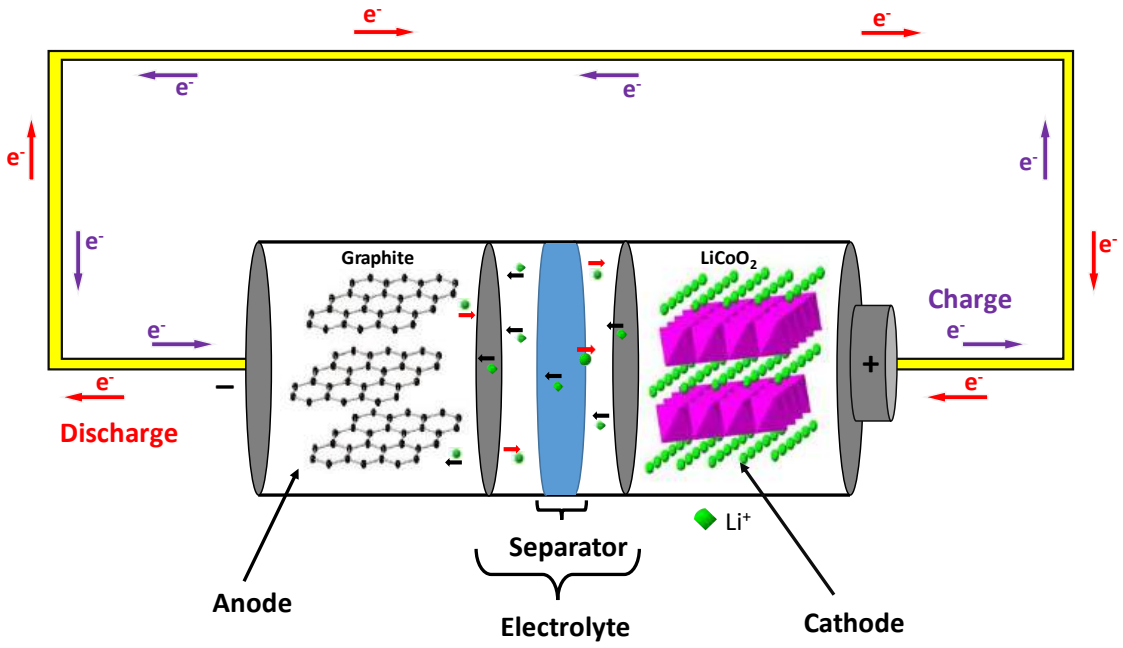

Figure 2.1: Schematic presentation of lithium-ion battery illustrating the working principle of charging (purple) and discharging (red).

Research into the lithium-ion battery (LIB) chemistry commenced in 1912 after G.N. Lewis presented the primary cells and were first commercialized in the 1970s. The initial development of rechargeable LIBs failed due to safety issues caused by the reactivity of lithium metal that was utilised as the anode in the cell, however, successive improvements eventually lead to the implemented technology of secondary batteries. This includes John B. Goodenough discovering $LiCoO_2$ (lithium cobalt oxide) cathode material, as well as Rachid Yazami discovering graphite as the anode material with a solid electrolyte material that led to the initial commercialization of rechargeable batteries in 1991 by Sony and Asahi Kasei using a lithium prismatic battery design [5].

Lithium-ion batteries are devices that generate electrical energy from chemical energy through an electrochemical redox reaction. During the discharging state of LIBs, lithium ions are extracted from the cathode which then pass through the separator to the anode where these ions get intercalated into the anode material (where intercalation is the insertion of ions into a layered structure). The cathode itself is also an intercalation material and is thus the host system which stores guest (mobile) ions that can be injected and removed from the host system reversibly. In LIBs, Li-ions are the guest ions with the host network consisting of transition metal oxides, metal chalcogens and polyanion compounds [6].

A wide range of materials have been explored for their use as cathode and anode electrodes in LIBs, where these materials are often separated by a microporous polymer separator which is usually polyethylene. This, together with the electrolyte that can be used in these batteries, must be an electrical insulator and have a high ionic conductor as they enable the movement of ions while disabling electrons from passing through to prevent short circuits [7].

Lithium is the lightest of all metals with an atomic mass of 6.941 g/mol, however, it has the greatest electrochemical potential which makes its use in the fastest-developing battery chemistries possible. LIBs are reshaping our daily lives, with many devices relying on the use of LIBs, such as electric vehicles, mobile devices, etc. [8].

The Ragone plot (Fig.2.2) shows that LIBs have outperformed other secondary battery chemistries such as nickel-cadmium (Ni-Cd), lead-acid, and nickel-metal hydride (Ni-MH) when comparing their specific power and energy. Specific energy is the energy that is collected per unit mass and specific power is described as the rate at which energy can be transferred per unit mass. High-energy storage devices are able to store a large amount of energy which makes them sophisticated devices and they transfer energy fast enough for applications such as electric vehicles [9].

When assessing batteries based on their performance, high specific energy density and power delivery capabilities where this batteries will be able to store larger amounts of energy and be able to release high amounts of energy quicker, another parameter is the long cycle life which is the amount of charge-discharge that the battery can complete before losing the performance, hence the longer the cycle life the longer the battery will last since there are more cycles it will be able to complete. Batteries with high specific capacity are also being

assessed since these measures the amount of energy batteries can store energy and have the ability to provide more power to devices (in milliampere hours or mAh) [10].

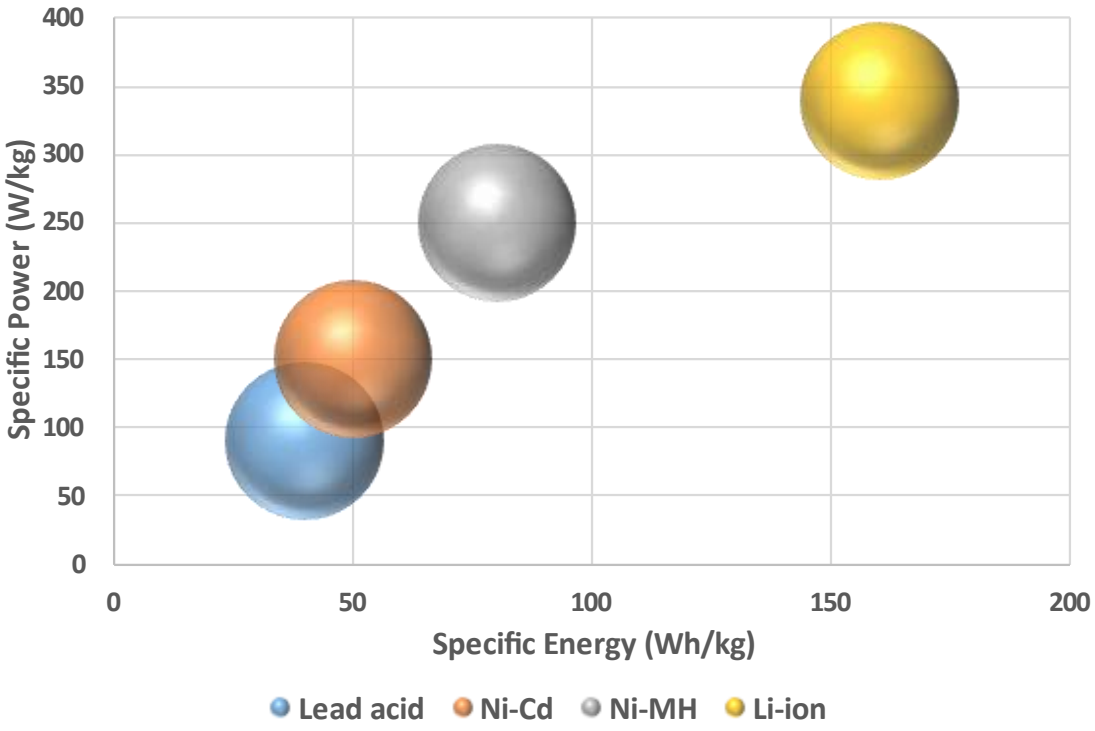

Figure 2.2: Ragone plot comparing different batteries in terms of specific power and energy (Adapted from [11]).

2.1.1. Safety management system of LIBs

The development of LIBs was delayed due to safety concerns as these batteries have relatively unstable chemistries which have caused serious threats and led to several products being recalled by manufacturers. Several thermal runaways have been reported in the literature which include an incident involving Samsung's Galaxy Note 7 catching fire and exploding, a Tesla vehicle battery catching fire, and the Boeing 787 Dreamliner battery problems [12].

It was reported that the Samsung's Galaxy Note 7 explosion was caused by an ultrathin separator that was damaged easily by an outer pressure on the positive electrode causing the battery to short circuit [13]. The incident which led to a Tesla vehicle catching fire happened when the vehicle collided with metal debris that punctured the cover and the battery pack. This debris penetrated through the polymer separators and directly connected the cathode and anode materials causing the battery to short circuit. The Boeing 787 incident happened after leakage of a flammable battery fluid from the plane's main LIB which then caused an explosion [14, 15].

The above-mentioned incidents have been the driving force for recent developments on improving the safety of LIBs, and the prevention of lithium dendrite formation as these have also caused thermal runaway. These issues have been mitigated by different approaches such

as the development of solid-state electrolytes, polymers with high melting points to increase thermal integrity of the separator, and mixing the flame retardants with graphite in a form of polymer binders [16, 13].

In addition, battery designs have also been explored to improve the safety, with some of the battery packages feature cooling functions such as thermal management systems (which involve circulating air or liquid) and the use of phase change materials (such as paraffin wax) to regulate temperature to avoid temperature fluctuations [12]. Li-ion cells are built in many different configurations and shapes such as prismatic, button, pouch, and cylindrical cells (Fig.2.3) [17].



Figure 2.3: Different battery designs: (a.) Cylindrical cells, (b.) Prismatic cell, (c.) Button cells and (d.) pouch cells [17].

Prismatic cells are rectangular and can be produced into a relatively thin envelope-type shape. These types of cells are made of layering the coated anode and cathode films that are wrapped into a suitable stacked arrangement and can be packed to fit into thin electronic devices such as cell phones and tablets [18]. Prismatic cells are usually made by fitting the cell content into an external hard casing and are often used in large systems such as electric vehicles and grid storage backup systems. The cell housing is made of aluminium or hard plastics and their cell capacity ranges between 20-50 Ah [17].

Button cells, also known as coin cells, are in compact designs and can be used in portable devices such as rechargeable watches, car keys, and hearing aids [19]. Button cells are small and cheap to build; they also achieve higher voltage after stacking several cells in series. Rechargeable coil cells are also commonly used by research facilities that develop or investigate electrochemical properties [17].

The most commonly used packaging style for both primary and secondary cells are cylindrical cells as they offer good mechanical stability and are relatively easy to manufacture. The typical applications for these cells are laptops, power tools, and medical instruments as they can be built to different sizes and placed in series and parallel configurations [9]. The well-known Tesla electric vehicle uses the conventional cylindrical cell where each vehicle battery pack can have more than 7000 cells. Although cylindrical cells have less ideal stacking capabilities, the space provided between the cells allows for better thermal management [18].

Pouch cells offer a flexible, simple, and lightweight solution to battery pack designs. These types of batteries are most efficient in space usage with an average of 90-95% packing efficiency [17], and they are currently used in many applications such as drones, electric vehicles, grid storage systems, and hobby gadgets. These cells do not have a standard design which makes it easier for the manufacturers to create designs that can accommodate their purpose. Pouch cells can have an extreme swelling concern; however, scientific data have shown that to mitigate this, it is best not to stack pouch cells on top of each other but rather lay them flat or allow spaces in between the cells [17].

2.2. Cathode materials

This research focuses on the cathode material of lithium manganese oxide which then looked at adding cation doping on its structure. The required specifications for preparing cathode material and their successful use in lithium-ion batteries include the following [20]:

1. The host structure must have the ability to intercalate a large quantity of lithium ions to provide high energy capacity.
2. The oxide materials should be cheap, chemically stable, and non-toxic.
3. In order to provide long cycle life, structural changes that occur during intercalation and deintercalation should be as small as possible.
4. To provide a high discharge voltage, the discharge reaction must have large negative Gibbs free energy.
5. A high lithium chemical diffusion coefficient resulting in high power density must be present in the structure of the cathode material must have.
6. The handling of materials should be easy.

To date it remains a challenge to find a suitable material that satisfies all these conditions.

Different cathode materials have been explored, and some of these materials have improved energy density and stability [20]. As previously mentioned, intercalation compounds have two properties that make them unique, firstly the guest ions are mobile between the sites in the host network, and secondly, the host material is involved in the electron transfer system as it contains transition metal ions that have variable oxidation states which can donate and accept electrons. The typical intercalation compounds for commercial LIBs cathode materials

have displayed different crystallographic structures such as spinel, layered, olivine, and tavorite structures [21].

2.2.1. The historical lithium cobalt oxide ($LiCoO_2$)

Lithium cobalt oxide, $LiCoO_2$, with an α-$NaFeO_2$ structure, was the first successfully commercialized type of layered oxide-based structure used as an active intercalation cathode material (Fig.2.4). In this structure, cobalt and lithium are situated in the octahedral sites occupying alternate layers which forms a hexagonal symmetry [22]. $LiCoO_2$ is an attractive cathode material mainly due to its high theoretical volumetric capacity of 1363 mAh cm^{-3} and high theoretical specific capacity of 274 mAh g^{-1}, as well as good capacity cycling performance [23].

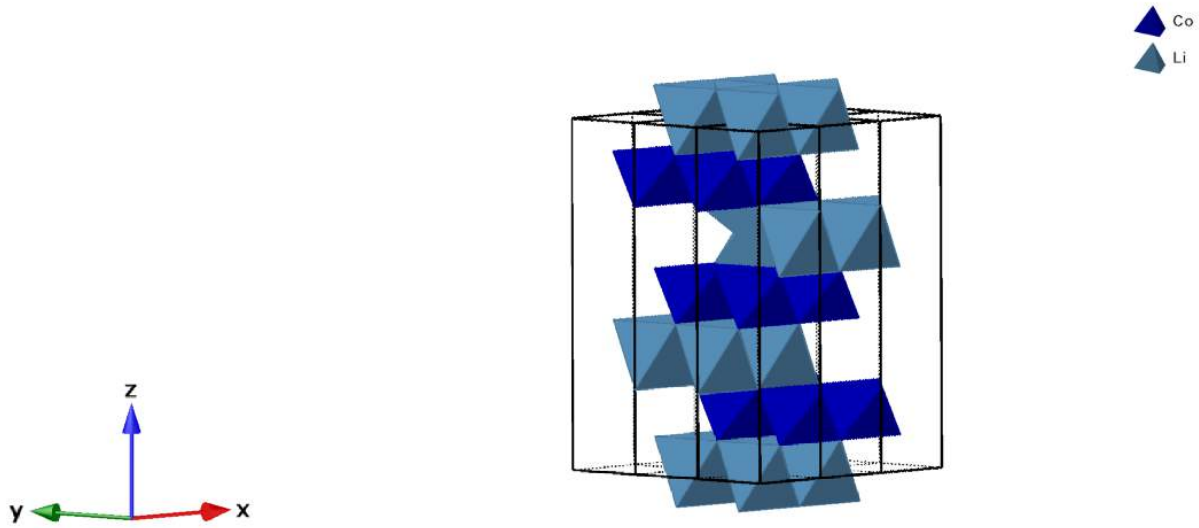

Figure 2.4: Layered Crystal structure of $LiCoO_2$ with *R*-3*m* space group.

The main constraints of batteries with $LiCoO_2$ materials are due to their thermal instability and a rapid loss of capacity at high current rates. The thermal instability of the active material relates to the exothermic release of oxygen when heating the $LiCoO_2$ oxide as the temperature rises over 140 °C as described by Jhu *et al*. [24]. The released oxygen then moves to the organic-based electrolyte (dimethyl carbonate and ethylene carbonate) which propagates thermal decomposition to the extent where the cell can explode [8]. Thermal runaways frequently occur due to the intercalation cathodes; it has been noticed that $LiCoO_2$ has the lowest thermal stability when compared to other commercialized cathode materials [25].

$LiCoO_2$ is relatively more expensive when compared with other metal oxides used as cathode materials due to the cost of cobalt [26]. Despite the cost, cobalt is a key component of many batteries. However, mining of cobalt has raised global concerns which include the abuse of human rights and the condition of labourers in the Democratic Republic of Congo which

supplies about 6% of the world's cobalt, with China and Zambia being other countries that supply cobalt [27].

The increasing global demand for LIBs has been opening doors for researchers to investigate other elements that can actively replace cobalt in cathode materials while maintaining the performance of the battery. Various metals (like Ni, Mn, Al, Fe, and Cr) have been considered as dopants or partial replacements for cobalt in the layered structure. In addition, coating of $LiCoO_2$ metal oxides with Al_2O_3, B_2O_3, TiO_2, ZrO_2, and carbon has been reported to improve the material stability and performance characteristics even in the course of deep cycling due to the chemical and mechanical stability of materials used for coating [23].

2.2.2. The interesting lithium manganese oxide ($LiMn_2O_4$)

Another cathode material that is used in lithium-ion cells is lithium manganese oxide, $LiMn_2O_4$ (LMO), which has been considered an interesting cathode material as it has replaced $LiCoO_2$ due to its environmental friendliness and low cost [28, 29, 30]. $LiMn_2O_4$ occurs in different forms where the three-dimensional cubic spinel structure is mostly used in the lithium-ion cells. The space group of this cubic spinel is *Fd*-3*m* with the oxygen ions are on the 32(*e*) site, while the Li and Mn cation occupying the 8(*a*) and 16(*d*) sites respectively as presented (Fig.2.5).

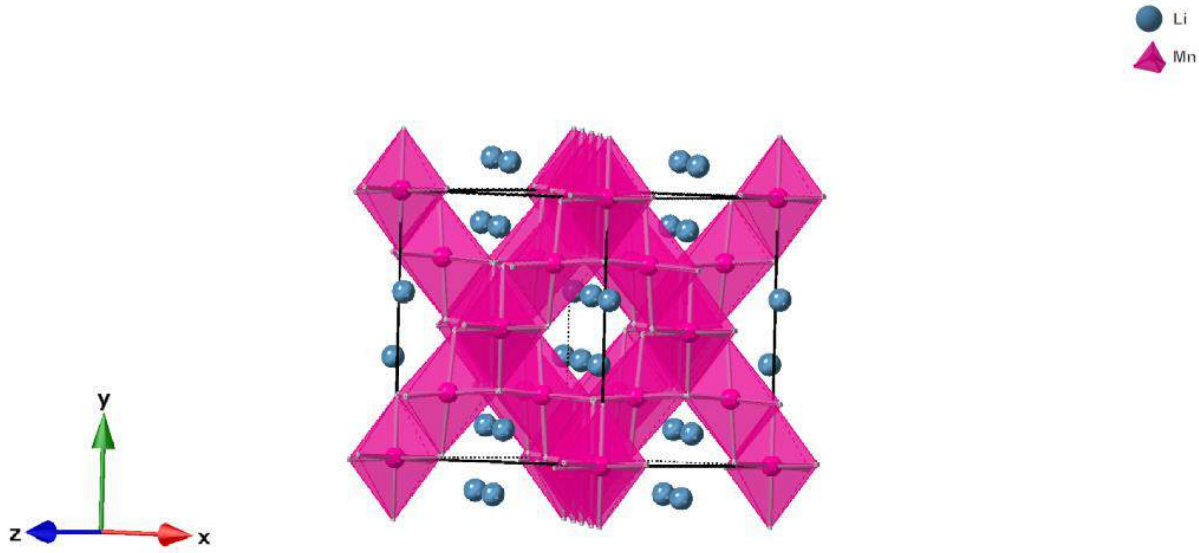

Figure 2.5: Crystal structure of $LiMn_2O_4$ with space group *Fd*-3*m*.

$LiMn_2O_4$ can achieve the future demand and low cost due to the relative abundance of Mn, environmentally friendliness, and thermally stable lithium-ion batteries with high energy and high-power density [31]. However, these cathode materials suffer from inadequate long-term cyclability that originates from the irreversible side reactions with the electrolyte. It has been noted that cationic doping partially substitutes some of other Mn ions in the parent $LiMn_2O_4$ which is effective for a better cycle life of the 4 V range. By utilizing nanoparticles to improve rate performance due to better electronic transport and shorter Li^+ diffusion lengths [31].

Further to the spinel structure, the lithium-rich manganese oxide, is a promising cathode material which exhibit high voltage and specific capacity that exceeds 250 mAh g^{-1} at a cheaper rate [32]. The commercialization of these materials has been delayed due to the major voltage decay that arises during prolonged cycling, this voltage decay is caused by (i) the formation of Li_2O, (ii) the localization of Oxygen 2*p* electron holes and (iii) a phase transition of a layered to spinel, the thermodynamic phase stability of lithium-inserted 3*d*-transition metal oxides have been lacking which also causes voltage decay in the metal oxide [33]. It was observed that the cobalt-free $Li[Li_{0.2}Ni_{0.2}Mn_{0.6}]O_2$ layered material provides a high capacity due to the interplay of cationic and anionic redox activity. In the lithium-rich oxides where Li ions are dominant, leading to the Li excess phase such as $Li_{1+x}Mn_{2-x}O_4$ (x= 0, 0.125), lithium antisite is formed by replacing some Mn ions on the 16d sites, the excess Li^+ in the structure was found to increase the diffusion of lithium ions by introducing mobile lithium ion, because of the substitution of Mn^{3+} by Li^+ in the structure [34].

$Li_{0.4}Mn_{0.6}O_{1.6}$ of a cubic spinel with space group (*Fd*-3*m*) is thermodynamically stable at a low concentration of Li content of about 0.00 ≤[Li] < 0.4. When increasing the Li concentration between the range of 0.4 <[Li]< 1.2, it leads to three coexisting phases containing Li-rich layered phase with *C*2/*m* space group, the spinel type phase of space group *Fd*-3*m* and rock salt type with the similar *Fd*-3*m* space group. However, further addition of Li content (1.2 <[Li]< 1.52) results in a stable monoclinic layered phase with a *C*2/*m* space group (Fig 2.6). There is evidence that spinel to layered phase transition occurs during a high lithiation reaction which causes the layered cathode material to change its structure to rock salt type and then to Li-poor spinel phases due to the release of oxygen and lithium which is the main factor for voltage decay during the cycling of the battery [32, 35].

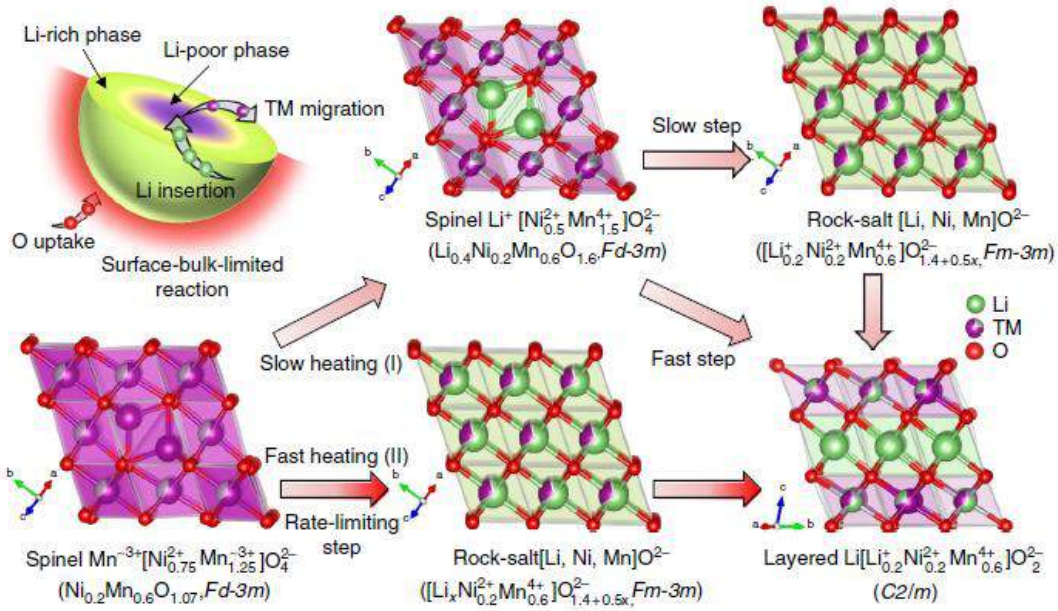

Figure 2.6: The pathways in which Li-rich layered oxide is formed from the spinel oxide structure with transition metal migration (TM) [32].

The manganese cation (Mn^{3+}) has a high spin and a strong magnetic moment, which is a Jahn-Teller distortion effect that results in a tetragonal deformation in the surrounding oxygen environment [31]. As lithium is fully ionized (as Li^{+}) in these materials, the addition and removal of the Li^{+} ions from the structure during discharge and charge cycles, respectively, requires that electron transfer out of and into the manganese oxide host occurs, respectively, by changing the valence state of the Mn ion and thereby maintaining charge neutrality. Li *et al.* [36] reported that the Jahn-Teller effect occurs as there is multiple valences of Mn (Mn^{3+} and Mn^{4+}) in $LiMn_2O_4$ with an average distance of 3.5 Å. As the concentration of Mn^{3+} increases during a discharging cycle, the distortion effect becomes notable and causes a significant breakdown in the crystal lattice during capacity cycling [31, 20].

Different methods have been used to enhance $LiMn_2O_4$ stability which includes, reducing Mn^{3+} content by cationic doping and surface coating, e.t.c. The effective way to change the valence in the lattice is through cationic doping at the Mn site which can also increase the stability of material during charging and discharging cycles. Al, Mg, Zn Co and others have been used to enhance the stability of $LiMn_2O_4$, Chen *et al.* [37] has reported that Al doping has been found to be effective in the suppression of Jahn Teller distortion effect during charging and discharging cycles and enhanced the electrochemical performance of $LiMn_{2-x}Al_xO_4$ (x= 0.05, 0.10 and 0.16).

Ando *et al.* [38] reported that $LiMn_2O_4$ metal oxide is sensitive to high operating temperatures and voltage. Therefore, it is critical to produce pure $LiMn_2O_4$ with homogeneous particle size distribution to enhance the morphology and structural properties (with smaller particle sizes having relatively large surface area to volume ratio which improves the Li-ion diffusion), hence when synthesizing pure metal oxides, the first priority is to control the reaction conditions such as temperature and mixing starting material at the right stoichiometric ratios. Solid state synthetic method is commonly used to produce a pure and homogeneous $LiMn_2O_4$ at high temperatures. Sol-gel, hydrothermal and co-precipitation synthetic method has been explored when producing $LiMn_2O_4$. Hwang *et al.* [39] reported that sol-gel method produces homogeneous, and high purity spinel $LiMn_2O_4$ and $LiAl_xMn_{2-x}O_4$ (x= 0.05, 0.15).

2.2.3. The famous lithium-ion phosphate ($LiFePO_4$) cathode material

Another commercialized cathode material is lithium iron phosphate, $LiFePO_4$, with an olivine structure which is known for its thermal stability and high-power capabilities. In $LiFePO_4$, the Fe^{2+} and Li^{+} occupy octahedral sites while P^{3-} occupies tetrahedral sites in a slightly distorted hexagonal close-packed oxygen array (Fig.2.7) [40].

$LiFePO_4$ is relatively cheap compared with other cathode materials, however, the major disadvantages of these types of cathode materials are their lower average cell potential and poorer electronic and ionic conductivity. Significant improvements in the performances of $LiFePO_4$ was achieved due to the reduction of material's particle size in combination with

carbon coating and cationic doping with elements such as Y (yttrium) and Nb (niobium) [11]. Lithium manganese phosphate oxide, $LiMnPO_4$, is a novel material in the group of olivine structures, where it offers a slightly higher voltage when compared to $LiFePO_4$ with specific capacity (~170 mAh/g), these $LiMnPO_4$ suffers from lower conductivity [41].

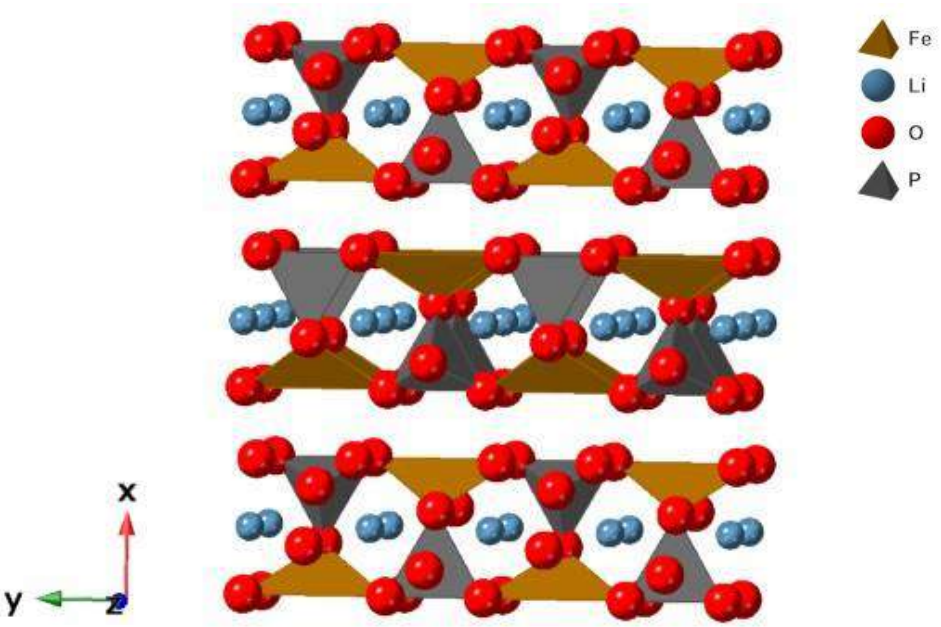

Figure 2.7: An olivine $LiFePO_4$ crystal structure with *Pnma* space group.

2.2.4. $LiFeSO_4F$ as cathode material

$LiFeSO_4F$ (LFSF) is an alternative class of cathode materials which have high cell voltage and acceptable specific capacity. LFSFs are the most interesting class of materials as they have superior ionic and electronic conductivity, therefore they do not require carbon coating or cathode materials in a form of nano-sized particles to improve their conductivity [42]. LFSF-type materials can undergo charge and discharge cycles at a very high rates with a specific capacity of ~148 mAh/g and they have the potential of being cost-effective since they are synthesized from abundant resources, however, these materials have not been commercialized as yet [43].

2.2.5. Effects of cationic doping on cathode materials

The performance of cathode materials can be improved by utilizing dopants; however, the effects of doping result in a complicated interpretation as there is an interrelation between the microstructure and morphology. In a variety of cathode materials, aluminium is the most commonly used dopant which have shown excessive improvements. In general, a small dopant concentration of aluminium results in decreased capacity of the electrode material, since, unlike the transition metal ions it displaces, Al^{3+} cannot be further oxidized [44]. The addition of aluminium to $LiCoO_2$ leads to an increased lattice parameter thereby facilitating

lithiation and delithiation. When doping $LiMn_2O_4$ with aluminium, these have resulted in an improved materials capacity retention during cycling at high discharge currents. The observed effects of using Al^{3+} have led to improved electrode kinetics, structural modification, and microstructural effects [44].

Various dopants such as ruthenium, chromium, and zinc have been explored as they have different properties and results. Ruthenium has been used as a dopant on spinel-type materials such as $LiMn_2O_4$ and $LiMn_{1.5}Ni_{0.5}O_4$ [45]. The beneficial effect of utilizing ruthenium has been related to the stabilization of the crystal structure as well as the contribution of the Ru^{4+}/Ru^{5+} redox couple. Chromium can also be used as a dopant in the above-mentioned materials as it forms stable spinel-type structure, while reducing the ordering of lithium ions in $LiMn_2O_4$ [46].

Doping with zinc has resulted in the stabilization of a crystal structure and improved the performance of $LiFePO_4$ and $LiMn_2O_4$. Zinc is also beneficial if it is added through a coating of ZnO. However, zinc dopant is not beneficial on $LiNiO_2$, where rather co-doping with cobalt improves its performance and stabilizes the crystal structure or reduce the dissolution of the electrode [47].

Titanium is another dopant that is used in both layered and spinel structures [46]. TiO_2 is doped to reduce dissolution of the electrode in the electrolyte, however, the degradation of the TiO_2 can lead to a decrease in the cell potential [47]. When doping cathode materials with zirconium, a similar effect on cathode performance as titanium has been observed. Zirconium is therefore primarily used to stabilize the layered crystal structure and can also be used in $LiFePO_4$ to increase lattice parameters. Zirconium is doped as a ZrO_2 or $Zr(OBu)_4$ coating to reduce the reaction between the electrolyte and the cathode material on both layered and spinel structures. Another dopant used for improving the performance of the phosphate electrodes is magnesium. This dopant increases the lattice parameter and also facilitates the lithiation-delithiation cycle and stabilizes the crystal structure [48].

2.3. Synthetic methods

Different synthetic methods were developed and used to manufacture cathode materials used in LIBs including the sol-gel method, solid-state reaction, co-precipitation, Spray-pyrolysis, combustion method, and many others (Fig.2.8). This synthesis methods have definite influence on the morphology (surface texture, grain size, size distribution, crystallinity, and cationic ordering) and electrochemical properties (initial discharge, cyclability and capacity retention rate) of the synthesized cathode materials, these can also be directly affected by the synthesis method utilized [49]. The synthesis procedure must be easily applied on the industrial scale, in order for the material commercially viable. Table 2.1 lists the advantages and disadvantages of applying various techniques to synthesize cathode materials.

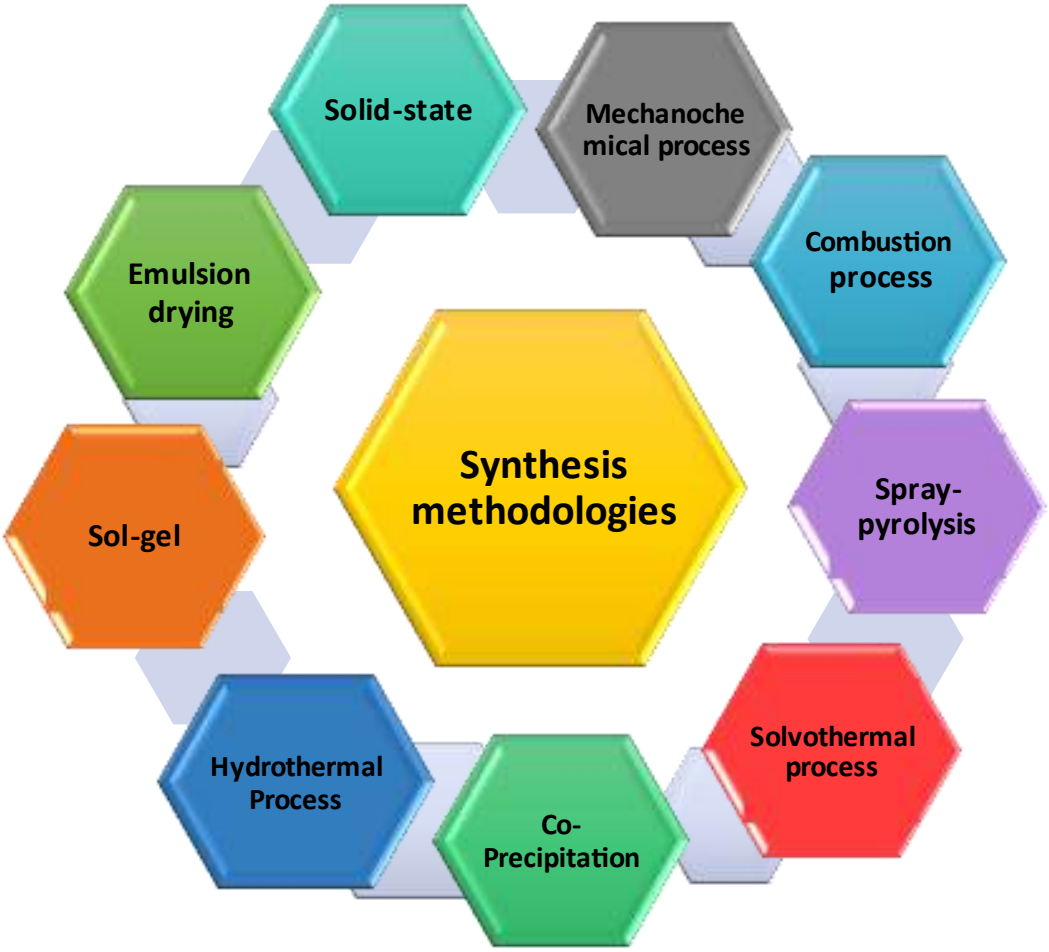

Figure 2.8: Various synthesis methodologies used to manufacture cathode materials for lithium-ion batteries, (Adapted from [50])

Table 2.1: Comparison of various synthesis routes for cathode materials [50].

Synthesis method	Advantages	Disadvantages
Sol-gel method	• Uniform particle distribution • Synthesise at lower temperatures • High crystallinity of synthesized materials • Homogeneous mixing of precursors • Short calcination period	• Excessive quantity of gas released
Solid-state reaction	• Easy process • Easy to apply to industrial level	• Synthesis requires high temperatures • High energy consumption • Non-uniform particle distribution
Co-precipitation	• High crystallinity	• Large particle distribution
Hydrothermal method	• High reaction yield • Lower synthetic temperatures	• Expensive equipment for synthesis
Spray-pyrolysis	• High-purity products • Rapid reaction rate • Easy to control the particle size	• Waste of precursor solution • Low deposition rate
Combustion method	• Short heat treatment • No additional calcination stages	• Hard to control phase and morphology

2.3.1. Sol-gel process

The sol-gel method has been commonly Adapted for synthesizing cathode materials as it ensures uniform particle distribution and excellent purity, while promoting the good control of the microstructures and the ease of compositional adjustment. Most sol-gel synthesis use acetate or nitrate salts as starting material precursors while utilizing succinic acid, ascorbic acid, poly-acrylic acid and citric acid as a chelating agent, chelating agent is used to form a stable ring like structure with the metal ion while enhancing its stability [51].

The sol-gel process happens via hydrolysis and condensation of the metal oxide precursors, at the hydrolysis step the transformation of the precursors forms a sol from a fully homogeneous starting material that has been completely dissolved in a solvent of interest under a constant heating environment, as the heating continues, the condensation step starts to kick in which then ultimately forms a gel. After the gel formation, a thermal drying such as an oven is required to dry the gel which becomes a powder (precursor), this powder will then be calcined in the furnace to form the final metal oxide (Fig.2.9) [52].

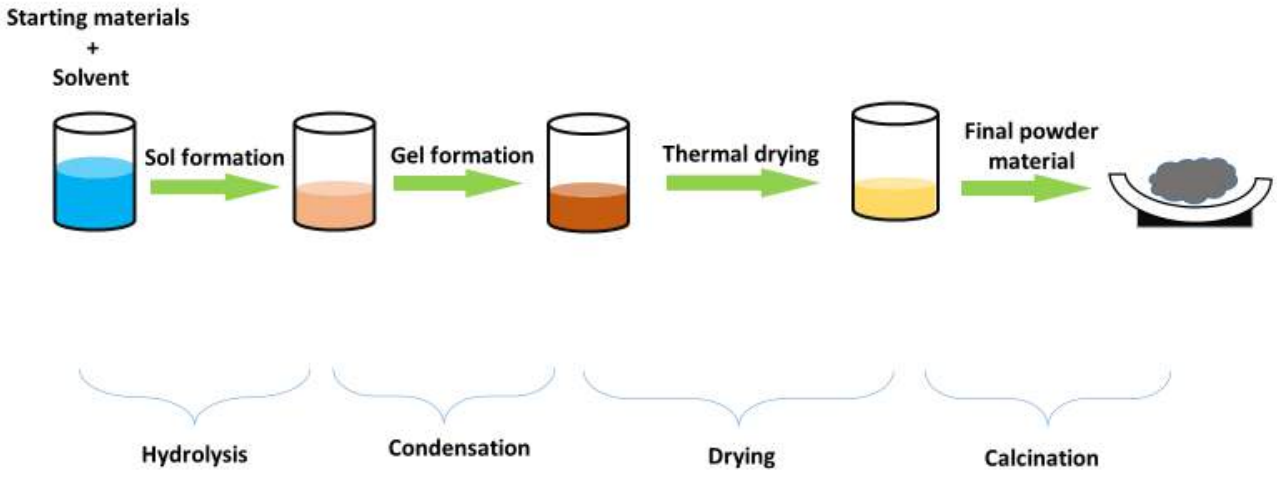

Figure 2.9: A schematic of the sol-gel method. (Adapted from *[52]*).

The process of sol-gel has been applied in thin-film coating, powder synthesis, and modification of electrode/electrolyte interfaces. The precursors that are synthesized via the sol-gel method provide chemical homogeneity and they are perfect for multi-layer structure formation while achieving a desirable microstructure for cell electrodes with small grain sizes, high porosity, and large surface area [53].

Citric acid is an organic molecule that has been commonly used in sol-gel chemistry, since it has three carboxylic acid molecules which can dissociate and chelate all the ions in the solution. This acid has been successfully used as a complexing agent with the advantage of low cost [54]. In a normal synthesis, aqueous solutions of metal salts are blended with citric acid to form a gel while the addition of ammonia and/or ethylene diamine adjusts the pH and improves the cation binding to the citrate (uniformity and stability of the metal nitrate solution depend on the pH) [55].

When metal-citric gels are exposed to heat, decomposition of the organic components occur between 300-400 °C which depends on the metal ion. In addition, the sol-gel method can be utilized to synthesize metal oxides in crystalline and amorphous forms with a better material homogeneity [56]. This synthetic route was explored by Jeong *et al.* [57] when synthesising lithium manganese oxide using acetate salts as starting material.

2.3.2. Solid-state method

The solid-state synthetic method has been a widely utilized method for obtaining various cathode materials because it is a facile process and can be applied on the industrial scale with ease. The most critical stages in the solid-state reaction are the constant mixing of precursors and the heat treatment [51]. The synthesis begins with mixing the starting precursors by ball milling/ grinding to achieve a homogenous mixture which is then pelletized and calcined, and then annealed to improve the structural stability and induce particle size growth (Fig.2.10.). This method has exhibited several drawbacks such as non-uniform particle size, high energy consumption, poor crystallinity with larger particles and lower electrochemical performance [58].

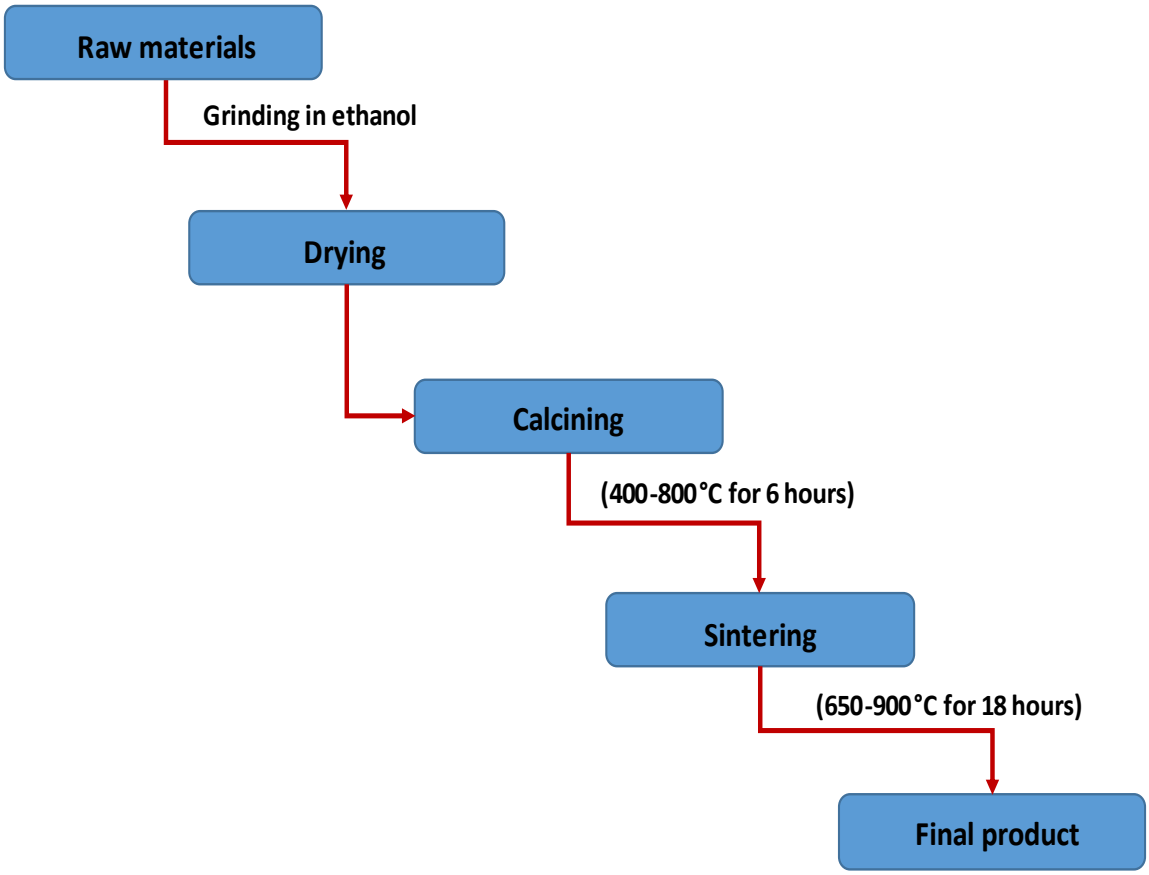

Figure 2.10: A typical schematic representation of the solid-state reaction method

Solid state reaction is commonly used to prepare $LiFePO_4$ cathode materials as this synthesis method can obtain an ordered crystal structure simply. In general, Li_2CO_3, $LiOH.H_2O$, or CH_3COOLi are utilized as lithium sources, with $FePO_4.2H_2O$ and $Fe(CH_3COO_2)_2$ utilized as iron sources. $(NH_4)_2HPO_4$ or $NH_4H_2PO_4$ are mostly used as phosphorus sources when preparing $FePO_4$ where the electrochemical performance varies due to the raw material used during preparations [59].

2.3.3. Co-precipitation

The co-precipitation method has been explored as it provides highly crystalline materials with uniform particle distribution, small particle size, and a reduced synthesis time while utilizing low energy consumption to achieve good yields with high purity. In this method, lithium and manganese salts are dissolved in water, the mixture is then heated at constant heat until a precipitate is formed, during this process, the mixture is filtrated, washed, and then dried under argon flow, and the residue is then subjected to heat treatment (Fig.2.11) [60].

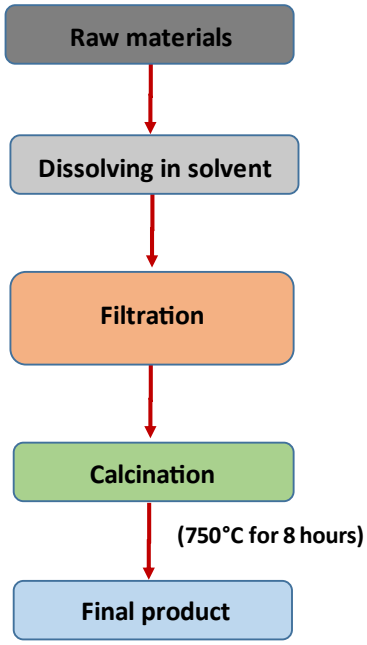

Figure 2.11: Flow chart of the co-precipitation method

The co-precipitation method is complex, and its reaction utilizes transition metal salts such as $NiSO_4.6H_2O$, $MnSO_4.H_2O$, and NH_3 as complexing agents, while NaOH is used to maintain high pH solutions ~9.8 or higher [61]. However, this method has low removal efficiency and can produce toxic sludges, as it is easy to produce side phases. Disruptions to the structure properties can also occur if care was not taken to prevent the oxidation of readily oxidizable metal ions. The reaction temperature is limited to ~60°C as higher temperatures can lead to higher densities and larger particle sizes [62].

2.3.4. Hydrothermal reaction

The hydrothermal synthesis route has been widely utilized in the preparation of advanced nanomaterials in electronics, ceramics, and biomedical applications as it exhibits better nucleation control, high purity, low energy consumption, and uniform particle distribution and it can be utilized as a one-step hydrothermal reaction process. This process is carried out in a closed system called autoclave which is a Teflon lined stainless steel that allows different

environmental conditions with controlled temperature and pressure for a chemical reaction to occur [63].

Hydrothermal reaction begins when precursors are mixed with the exact stoichiometric amounts in the aqueous solution, which is then dried in an autoclave at a temperature higher than 100°C and then cooled to room temperature followed by repeated washing and filtering, the obtained precipitate can then be dried at elevated temperatures (400-750°C) under argon or N_2 atmosphere (to carbonize the carbon sources) to obtain the final product (Fig.2.12). The solution temperature is an important parameter in hydrothermal synthesis as the particle size, reaction rate, ionization degree, and crystalline structures are all temperature dependent [50].

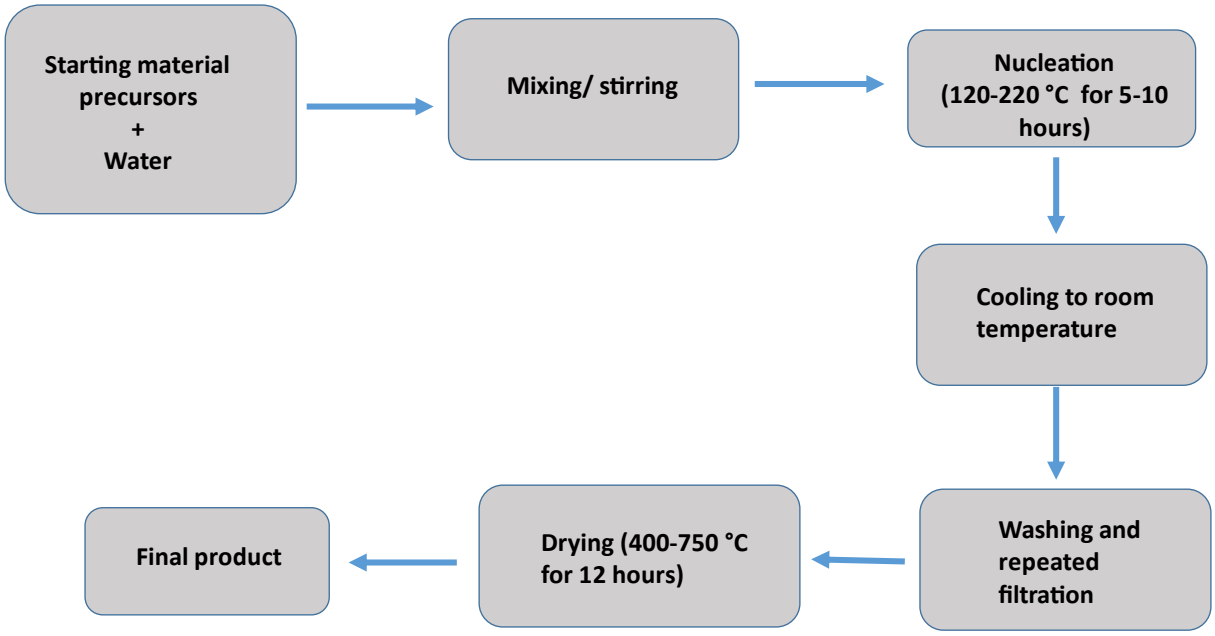

Figure 2.12: Schematic representation of the hydrothermal synthesis

Although, the hydrothermal method is a solution-based process that depends on the solubility changes and chemical reactions of materials under controlled pressure and temperature in a sealed container, this method requires expensive autoclaves and have safety issues due to high operating pressure [64].

2.3.5. Spray pyrolysis

The spray pyrolysis method is convenient for producing fine particles, and good quality, well-crystalized materials within a short time. The particle sizes obtained through spray pyrolysis method are in narrower range when compared to those produced using solid-state reactions. The synthesis process is quick, easy, straight forward and controllable; however, it requires high evaporation rates and is more suitable for drying heat-sensitive materials [65].

Spray pyrolysis uses a slurry or liquid mixture that is sprayed through a nozzle which is rapidly dried in air or nitrogen (if the solvent/ liquid is flammable or oxygen-sensitive). In this

technique, very fine controlled droplets are dispensed using a spray nozzle or atomizers and this is a critical step as the droplets act as the nucleation centres and evolved as crystallized pure particles. The synthesis starts with spraying droplets solution in the furnace that is set at temperature around 400-600 °C by carried gas, which rapidly dries the droplets into powders that are collected and annealed at high temperatures of 700-800 °C [50]. The spray-pyrolysis method can be affected by synthesis parameters such as the heating rate of the droplets, the type of precursor, and the material homogeneity and polymeric agents in the initial solution [66, 67]

2.3.6. Combustion method

Another synthetic method is the combustion method which is favourable when producing nanomaterials with good crystallinity and high surface area. The combustion method can be exercised in two ways: the thermal explosion mode and high-temperature synthesis (self-propagation). The self-propagation is non-explosive method which forms a lot of gases that can appear as flames and the temperature can go up to 1300°C where the nitrate salts decompose into metal oxides (Fig.2.13). In a combustion reaction, the precursor solution is mixed with the organic fuel until the mixture ignites causing the combustion reaction to take place which results in dry, crystalline fine powder particles, this is regarded as the explosive method.

The thermal explosion mode produces materials by exothermic combustion synthesis which is a time-saving and easy method. This method mainly uses lithium nitrate and hydrated manganese nitrated (nitrate salts) as raw materials to produce a homogeneous mixture while citric acid and urea are used as fuel. However, the exothermic nature of the reaction can lead to an explosion if not controlled. The major consequences of using the combustion method are mainly the lack of controlling the phase and morphology of the product.

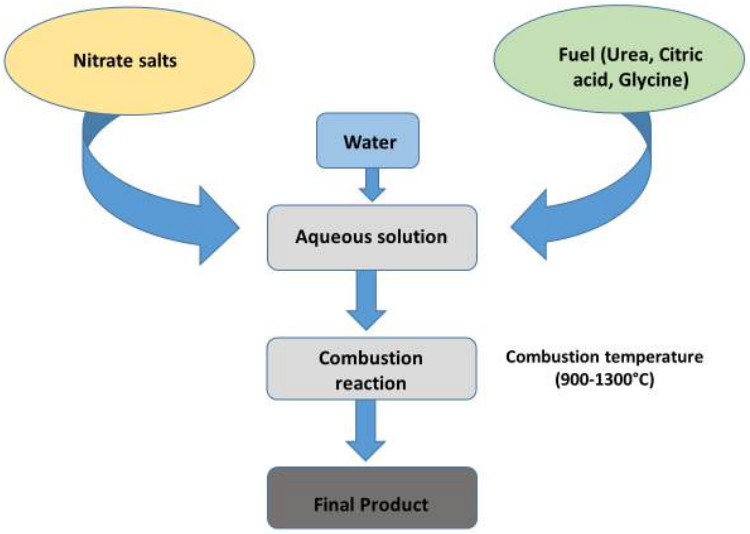

Figure 2.13: Schematic representation of combustion synthesis.

Another method is the solution combustion method (SCM) which is the most favoured wet synthetic method. A wet synthesis route is cost-effective and has easy control over particle composition and size where chemicals react in the solution phase with precursors. This method has produced materials that have homogeneously distributed micro-size particles to give an improved capacity performance [68].

2.4. Flow cell design

Modern diffraction techniques allow for *in-situ* variable temperature measurements. This is useful when there is an interest in understanding the synthesis of the cathode material. For example, when using the sol-gel method, phase transitions of the intermediate gel materials can be tracked as a function of increasing temperature as they react to produce their final active phase. There is an increasing appreciation of performing experiments having temperature control over both the sample and atmosphere even at high temperatures [69].

Temperature is the most explored environmental variable for non-ambient conditions at which materials are to be used (i.e. batteries, over 100 °C as well as below 0 °C), to study the structure-property relationships. The development of materials in energy storage devices needs an understanding of how ions interact with each other in the material through *in-situ* studies. However, the lack of experimental infrastructure that enables the study of materials at non-ambient conditions while the instrument remains suited to perform X-ray scattering experiments is a problem [70].

Sample holders or cells to be used for different sample-environments can be designed for X-ray diffraction and spectroscopy *in-situ* measurements which include the capillary-based, hydrothermal, and gas-loading reaction cells that can be designed for specific experiments [71]. The portable, easy-to-use, and compact sample cell (flow-cell) that allows the control of environmental parameters with the aim of reaching high temperatures of up to 1273 K (Fig.2.14) has been designed. This flow cell is a new way for variable temperature measurements that are based on a capillary sample geometry which is fitted using standard Swagelok where the sample environments can be exposed to a range of gas and fluid environments under flow conditions as well as controlling the input atmosphere [70]. The actual flow cell is designed without any the X-ray beam contributing to the background scattering [72].

The flow-cell has the advantage over conventional variable temperature studies where the cell can be able to do experiments using area detectors that include angle coverage to improve the signal-to-noise ratio. These allows high-resolution powder diffraction experiments and the ability to perform pair distribution function (PDF) measurements on 2θ scanning detectors [72].

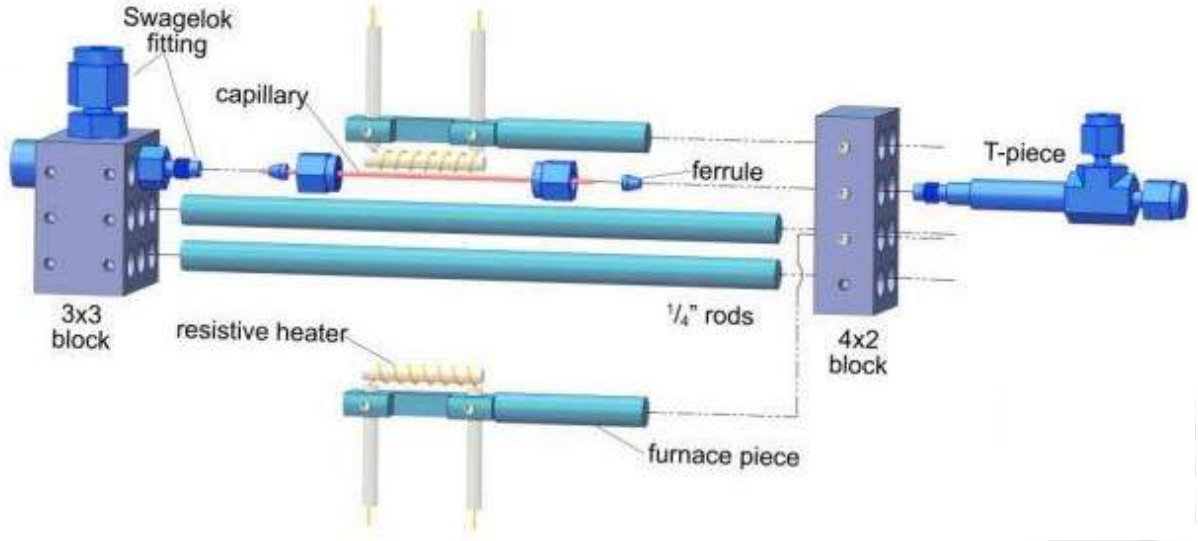

Figure 2.14: An example of a flow-cell components diagram for variable temperature measurement showing how they fit [72].

2.5. References

[1] R. Borah, F. R. Hughson, J. Johnston and T. Nann, "On battery materials and methods," *Materials Today Advances,* vol. 6, pp. 100046-100057, 2020.

[2] S. Koohi-Fayegh and M. A. Rosen, "A review of energy storage types, applications and recent developments," *Journal of Energy Storage,* vol. 27, pp. 101047-101073, 2020.

[3] J. G. Kim, B. Son, S. Mukherjee, N. Schuppert, A. Bates, O. Kwon, M. J. Choi, H. Y. Chung and S. Park, "A review of lithium and non-lithium based solid state batteries," *Journal of Power Sources,* vol. 282, pp. 299-322, 2015.

[4] R. Faria, P. Marques, R. Garcia, P. Moura, F. Freire, J. Delgado and A. T. Almeida, "Primary and secondary use of electric mobility batteries from a life cycle perspective," *Journal of Power Sources,* vol. 262, pp. 169-177, 2014.

[5] B. Schumm, "Development Of Batteries," Britannica articles, 7 January 2010. [Online]. Available: https://www.britannica.com/technology/battery-electronics/Development-of-batteries. [Accessed 4 December 2020].

[6] Y. Miao, P. Hynan, A. Von Jouanne and A. Yokochi, "Current Li-ion battery technologies in electric vehicles and opportunities for advancements," *Energies,* vol. 12, pp. 1073-1093, 2019.

[7] A. Eftekhari, "Low voltage anode materials for lithium-ion batteries," *Energy Storage Materials,* vol. 7, pp. 157-180, 2017.

[8] M. Broussely and G. Archdale, "Li-ion batteries and portable power source prospects for the next 5–10 years," *Journal of Power Sources,* vol. 136, pp. 386-394, 2004.

[9] R. A. Powers, “Advances and trends in primary and small secondary batteries,” *IEEE AES Systems Magazine,* vol. 1, pp. 32-36, 1994.

[10] C. M. Hayner, X. Zhao and H. H. Kung, “Materials for rechargeable lithium-ion batteries,” *Annual Review of Chemical and Biomolecular Engineering,* vol. 3, pp. 445-471, 2012.

[11] Y. Meesala, A. Jena, H. Chang and R.-S. Liu, “Recent advancements in Li-ion conductors for all-solid-state Li-ion batteries,” *ACS Energy Letter,* vol. 2, pp. 2734-2751, 2017.

[12] K. Liu, Y. Liu, D. Lin, A. Pei and Y. Cui, “Materials for lithium-ion battery safety,” *Journal of Materials Chemistry A,* vol. 4, pp. 1-11, 2018.

[13] T. O. Ely, D. Kamzabek and D. Chakraborty, “Batteries safety: recent progress and current challenges,” *Frontiers in Energy Research,* vol. 7, no. 71, pp. 1-24, 2019.

[14] B. Dipert, “Samsung Galaxy Note 7: Explosion diagnosis and prevention,” 3 January 2017. [Online]. Available: https://www.edn.com/samsung-galaxy-note-7-explosion-diagnosis-and-prevention/. [Accessed 12 April 2021].

[15] S. Taranovich, “Boeing 787 and Lithium Ion battery failure,” 17 January 2013. [Online]. Available: https://www.edn.com/boeing-787-and-lithium-ion-battery-failure/. [Accessed 12 April 2021].

[16] S. Taranovich, “Lithium-ion battery fires: 7 solutions for improved safety,” 30 September 2016. [Online]. Available: https://www.edn.com/lithium-ion-battery-fires-7-solutions-for-improved-safety/. [Accessed 12 April 2021].

[17] U. Battery, “Types of battery cells; cylindrical cell, button cell, pouch cell,” 30 June 2011. [Online]. Available: https://batteryuniversity.com/learn/article/types_of_battery_cells. [Accessed 20 May 2021].

[18] G. Lighting , “Lithium-ion batteries part I: general overview and 2019 update,” *Technical Notes,* vol. 1, no. 30, pp. 1-12, 2019.

[19] M. Greenwood, M. Wentker and J. Leker, “A bottom-up performance and cost assessment of lithium-ion battery pouch cells utilizing nickel-rich cathode active materials and silicon-graphite composite anodes,” *Journal of Power Sources Advances,* vol. 9, pp. 100055-100063, 2021.

[20] m. Wakihara, “Lithium manganese oxide with spinel structure and their cathode properties for lithium ion battery,” Journal of *Electrochemisry ,* vol. 73, no. 5, pp. 328-335, 2005.

[21] B. E. Murdock, K. E. Toghill and N. Tapai-Ruiz, “A perspective on the sustainability of cathode materials used in lithium-ion batteries,” Journal of *Advanced energy materials,* vol. 11, pp. 1-17, 2021.

[22] Y. Idemoto, J. W. Richardson, N. Koura, S. Kohara and C.-k. Loong, “Crystal structure of (Li_xKI_{1-x}) (x = 0, 0.43, 0.5, 0.62, 1) by neutron powder diffraction analysis,” *Journal of Physics and Chemistry of Solids,* vol. 59, no. 3, pp. 363-376, 1998.

[23] N. Nitta, F. Wu, J. T. Lee and G. Yushin, “Li-ion battery materials: present and future,” *Materials Today,* vol. 18, no. 5, pp. 252-264, 2015.

[24] C.-Y. Jhu, Y.-W. Wang, C.-Y. Wen and C.-M. Shu, "Thermal runaway potential of $LiCoO_2$ and $Li(Ni_{1/3}Co_{1/3}Mn_{1/3})O_2$ batteries determined with adiabatic calorimetry methodology," *Journal of Applied Energy,* vol. 100, pp. 127-131, 2012.

[25] Z. Chen, W. Zhang and Z. Yang, "A review on cathode materials for advanced lithium ion batteries: microstructure designs and performance regulations," *Nanotechnology,* vol. 31, pp. 1-36, 2020.

[26] A. Chen, "Elon Musk wants cobalt out of his battery- here's why that's a challenge," 21 June 2018. [Online]. Available: https://www.theverge.com/2018/6/21/17488626/elon-musk-cobalt-electric-vehicle-battery-science. [Accessed 20 May 2021].

[27] J. Campbell, "Why Cobalt Mining in the DRC Needs Urgen tAttention," 29 October 2020. [Online]. Available: https://www.cfr.org/blog/why-cobalt-mining-drc-needs-urgent-attention. [Accessed 20 May 2021].

[28] Y. Huang, Y. Dong, S. Li, J. Lee, C. Wang, Z. Zhu, W. Xue, Y. Li and J. Li, "Lithium manganese spinel cathodes for lithium-ion batteries," *Advanced Energy Materials,* vol. 11, pp. 2000997-20001018, 2021.

[29] M. M. Thackeray, M. F. Mansuetto, D. W. Dees and D. R. Visser, "The thermal stability of lithium-manganese-oxide spinel phases," *Journal of Materials Bulleti,* vol. 31, no. 6, pp. 133-140, 1996.

[30] B. Xu and D. Qian, "$LiMn_2O_4$ cathode material for lithium ion batteries," *Journal of Metallurgy and Materials Science,* vol. 45, no. 3, pp. 341-346, 2006.

[31] S. K. Mishra and G. Ceder, "Structural stability of lithium manganese oxides," Journal of *Physical Review B,* vol. 59, no. 9, pp. 6120-6130, 1991.

[32] W. Hua, S. Wang, M. Knapp, S. J. Leake, A. Senyshyn, C. Richter, M. Yavuz, J. R. Binder, C. P. Grey, H. Ehrenberg, S. Indris and B. Schwarz, "Structural insights into the formation and vltage degradation of lithium and manganese rich layered oxides," *Nature Communications,* pp. 1-11, 2019.

[33] P. Rozier and J. M. Tarascon, "Review—Li-rich layered oxide cathodes for next-generation li-ion batteries: chances and challenges," *Journal of The Electrochemical Society,* vol. 162, no. 14, pp. 2490-2499, 2015.

[34] J. Zheng, S. Myeong, W. Cho, P. Yan, J. Xiao, C. Wang, J. Cho and J.-G. Zhang, "Li- and Mn-rich cathode materials: challenges to commercialization," *Advanced energy materials,* vol. 7, pp. 1601284-1601311, 2017.

[35] H. Zheng, X. Han, W. Guo, L. Lin, Q. Xie, P. Liu, W. He, L. Wang and D.-L. Peng, "Recent developments and challenges of Li-rich Mn-based cathode materials for high-energy lithium-ion batteries," *Materials Today Energy,* vol. 18, pp. 100518-100535, 2020.

[36] X. Li, Y. Xu and C. Wang, "Suppression of Jahn–Teller distortion of spinel $LiMn_2O_4$ cathode," *Journal of Alloys and Compounds,* vol. 479, pp. 310-313, 2009.

[37] M. Chen, R. Wu, S. Ju, X. Zhang, F. Xue and W. Xing, "Improved performance of Al-doped $LiMn_2O_4$ ion-sieves for Li^+ adsorption," *Microporous and Mesoporous Materials,* vol. 261, pp. 29-34, 2018.

[38] K. Ando, T. Matsuda and D. Imamura, "Degradation diagnosis of lithium-ion batteries with a $LiNi_{0.5}Co_{0.2}Mn_{0.3}O_2$ and $LiMn_2O_4$ blended cathode using dV/dQ curve analysis," *Journal of Power Sources,* vol. 390, pp. 278-285, 2018.

[39] B. J. Hwang, R. Santhanam, D. G. Liu and Y. W. Tsai, "Effect of Al-substitution on the stability of $LiMn_2O_4$ spinel,synthesized by citric acid sol–gel method," *Journal of Power Sources ,* vol. 102, pp. 326-331, 2001.

[40] H. Raj and A. Sil, "Effects of carbon coating on electrochemical performance of $LiFePO_4$ cathode materialfor Li-ion battery," *Journals of Ionics,* vol. 24, pp. 2543-2553, 2018.

[41] J. Hu, W. Huang, L. Yang and F. Pan, "Structure and performance of the $LiFePO_4$ cathode material: from the bulk to the surface," *Journal of Nanoscale,* vol. 12, pp. 15036-15044, 2020.

[42] S. C. Chung, P. Barpanda, S.-i. Nishimura, Y. Yamada and A. Yamada, "Polymorphs of $LiFeSO_4F$ as cathode materials for lithium ion batteries – a first principle computational study," *Journal of Physical chemistry,* vol. 14, pp. 8678-8682, 2012.

[43] S. Lee and S. S. Park, "Comparative study of tavorite and triplite $LiFeSO_4F$ as cathode materials for lithium ion batteries: structure, defect chemistry, and lithium conduction properties from atomistic simulation," *The Journal for Physical Chemistry C,* vol. 118, no. 24, pp. 12642-12648, 2014.

[44] A. Dianat, N. Seriani, M. Bobeth and G. Cuniberti, "Effects of Al-doping on the properties of Li–Mn–Ni–O cathode materials for Li-ion batteries: an ab initio study," *Journal of Materials Chemistry,* vol. 1, pp. 9273-9280, 2013.

[45] D. Yan-huai and Z. Ping, "Effect of Mg and Co co-doping on electrochemical properties of $LiFePO_4$," *Transactions of Nonferrous Metals Society,* vol. 22, pp. 153-156, 2012.

[46] J. W. Fergus, "Recent developments in cathode materials for lithium ion batteries," *Journal of Power Sources,* vol. 195, pp. 939-954, 2010.

[47] D. R. SIMON, "Characterization of $Li_4Ti_5O_{12}$ and $LiMn_2O_4$ spinel materials treated with aqueous acidic solutions," *Journal of Materials Engineering,* vol. 1, no. 1, pp. 1-155, 2007.

[48] A.-H. Marincas and P. Ilea, "Enhancing lithium manganese oxide electrochemical behavior by doping and surface modifications," *Coatings,* vol. 11, pp. 456-488, 2021.

[49] J. Xiao, W. Xu, D. Choi and J.-G. Zhang, "Synthesis and characterization of lithium manganese phosphate by a precipitation method," *Journal of Electrochemical Society,* vol. 157, no. 2, pp. 142-147, 2010.

[50] N. Bensalah and H. Dawood, "Review on synthesis characterizations and electrochemical properties of cathode materials for lithium ion batteries," *Journal of Material Science & Engineering,* vol. 5, no. 4, pp. 1-21, 2016.

[51] A.-H. Marincas, F. Goga, S.-A. Dorneanu and P. Ilea, "Review on synthesis methods to obtain $LiMn_2O_4$ based cathode materials for Li-ion batteries," *Jounarl of Solid State Electrocemistry,* pp. 1-25, 2020.

[52] A. E. Danks, S. R. Hall and Z. Schnepp, "The evolution of 'sol–gel' chemistry as a technique for materials synthesis," *Royal Society of Chemistry,* vol. 9, pp. 91-113, 2016.

[53] M. Parashar, V. K. Shukla and R. Singh, "Metal oxides nanoparticles via sol–gel method: a review on synthesis, characterization and applications," *Journal of Materials Science,* vol. 31, no. 37, pp. 3729-3749, 2019.

[54] W. Li, X. Zhang, W. Lang, J. Si, J. Yang and L. Li, "The effect of chelating agent on synthesis and electrochemical properties of $LiNi_{0.6}Co_{0.2}Mn_{0.2}O_2$," *Journal of Applied Sciences,* vol. 554, no. 2, pp. 1-8, 2020.

[55] T. V. Satyavani, A. S. Kumar and P. S. Rao, "Methods of synthesis and performance improvement of lithium iron phosphate for high rate Li-ion batteries: A review," *Engineering Science and Technology, an International Journal,* vol. 19, pp. 178-188, 2015.

[56] M. Breedon, P. Spizzirri, M. Taylor, J. du Plessis, D. McCulloch, J. Zhu, L. Yu, Z. Hu, C. Rix, W. Wlodarski and K. Kalantar-zadeh, "Synthesis of nanostructured tungsten oxide thin films: a simple, controllable, inexpensive, aqueous sol-gel method," *American Chemical Society,* vol. 10, pp. 430-439, 2010.

[57] E. D. Jeong, S.-w. Moon, H.-M. Lee, M.-S. Won, J.-H. Yoon, P. Deog-Su and Y.-B. Shim, "Synthesis of lithium manganese oxide by a sol-gel method and its electrochemical behaviors," *Journal of the Korean Electrochemical Society,* vol. 6, no. 4, pp. 229-235, 2006.

[58] J. Liu, W. Qiu, L. Yu, G. Zhang, H. Zhao and T. Li, "Studies on the low-heating solid-state reaction method to synthesize $LiNi_{1/3}Co_{1/3}Mn_{1/3}O_2$ cathode materials," *Journal of Power Sources,* vol. 174, pp. 701-704, 2007.

[59] X. Jiang, Y. Sha, R. Cai and Z. Shao, "The solid-state chelation synthesis of $LiNi_{1/3}Co_{1/3}Mn_{1/3}O_2$ as a cathode material for lithium-ion batteries," *Journal of Materials Chemistry A,* pp. 1-9, 2015.

[60] D. Huang, J. Yan and X. Zuo, "Co-precipitation kinetics, microstructural evolution and interfacial segregation in multicomponent nano-precipitated steels," *Materials Characterizations,* vol. 155, pp. 109786-109800, 2019.

[61] A. N. Yazid and C. Y. Joon, "Co-precipitation synthesis of magnetic nanoparticles for efficient removal of heavy metal from synthetic wastewater," *AIP Conference Proceedings,* pp. 020019-1-020019-10, 2019.

[62] T. Entwistle, E. Sanchez-Perez, G. J. Murray, N. Anthonisamy and S. A. Cussen, "Co-precipitation synthesis of nickel-rich cathodes for Li-ion batteries," *Energy Reports,* vol. 11, pp. 67-73, 2022.

[63] S. Yadav and A. Sharma, "Importance and challenges of hydrothermal technique for synthesis of transition metal oxides and composites as supercapacitor electrode materials," *Journal of Energy Storage,* vol. 44, pp. 103295-103311, 2021.

[64] S. Yadav and A. Sharma, “Importance and challenges of hydrothermal technique for synthesis of transition metal oxides and composites as supercaopacitor electrode materials,” *Journal for Energy Storage,* vol. 44, pp. 103295-103311, 2021.

[65] C. D. Synders, E. E. Ferg, J. Schuelein and H. Loewe, “A review of using spray pyrolysis through sol-gel materials in the synthesis of cathode materials for lithium-ion batteries,” *South African Journal of Chemistry,* vol. 69, pp. 1-13, 2016.

[66] S. H. Park, S. W. Oh, S. T. Myung, Y. C. Kang and Y. K. Sun, “Effect of synthesis condition on $LiNi_{1/2}Mn_{3/2}O_4$ cathode material for prepared by ultrasonic spray pyrolysis method,” *Journal of Solid State Ionics,* vol. 176, no. 5-6, pp. 481-486, 2005.

[67] C. S. Yudha, S. U. Muzayanha, M. Rahmawati, H. Widiyandari, W. Sutopo, M. Nizam, S. P. Santosa and A. Purwanto, “Fast production of high performance $LiNi_{0.815}Co_{0.035}O_2$ cathode material via urea assisted flame spry pyrolysis,” *Energies,* vol. 12, no. 11, pp. 2757-2812, 2020.

[68] M. Kebede, M. Phasha, N. kunjuzwa, M. Mathe and K. I. Ozoemena, “Solution-combustion synthesized aluminium-doped spinel ($LiAl_xMn_{2-x}O_4$) as a high-performance lithium-ion battery cathode material,” *Journal of Applied Physics,* vol. 121, pp. 51-57, 2015.

[69] D. O'Nolan, G. Huang, G. E. Kamm, A. grenier, C.-H. Liu, P. K. Todd, A. Wustrow, G. T. Tran, D. Montiel, J. E. Neilson, S. J. Billinge, P. J. Chupas, k. S. Thornton and K. W. Chapman, “A thermal approach to variable temperature measurements resolved in space,” *Journal of Applied Crystallography,* vol. 53, pp. 662-670, 2020.

[70] H. W. Wyckoff, M. Doscher, D. Tsernoglou, T. Inagmi, L. N. Johnson, K. D. Hardman, N. M. Allewell, D. M. Kelly and F. Richards, “Design of a diffractometer and flow cell system for x-ray analysis of crystalline proteins with applications to the crystal chemistry of ribonuclease-S,” *Journal of Molecular Biology,* vol. 27, pp. 563-578, 1967.

[71] P. Ferrer, I. Silva, J. Rubio-Zuazo, B. F. Alfonso, C. Trobajo, S. Khainakov, J. R. Garcia, S. Garcia-Granda and G. R. Castro, “A flow-through reaction cell for in situ X-ray diffraction and absorption studies of heterogeneous powder-liquid reactions and phase transformations,” *Journal of Synchrotron Radiation,* vol. 19, pp. 93-100, 2011.

[72] P. I. Chupas, K. W. Chapman, C. Kurtz, J. C. Hanson, P. L. Lee and C. P. Grey, “A versatile sample-environment cell for non-ambient X-ray scattering experiments,” *Journal of Applied Crystallography,* vol. 41, pp. 822-824, 2008.

Chapter 3: Experimental methods

3.1. Materials synthesis

The sol-gel (Fig.3.1) method was used to synthesize the spinel phase of $Li_{1.03}Mn_{1.97}O_4$ by dissolving stoichiometric amounts of $LiNO_3$ and $Mn(NO_3)_2.H_2O$ in distilled water and adding citric acid with various concentrations of total metal ion to citric acid ratio (1: 1.667, 1: 1, 1: 0.883 and 1: 0.667) forming an aqueous solution. The aqueous solution was heated to 80 °C, while stirring constantly, until the gel was formed. The gel was dried in the furnace for 5 hours at 140 °C, cooled to room temperature and then ground using an agate pestle and mortar until a homogeneous fine powder was obtained. The precursor powder was further analysed using thermal analysis and X-ray diffraction where the final product was analysed using *ex-situ* X-ray diffraction *(ex-situ* measurements as a function of calcination temperature).

$LiAl_{0.4}Mn_{1.6}O_4$ was also prepared in the same way as described above, with the addition of $Al(NO_3)_3.9H_2O$ in the right stoichiometric amount, the precursor material and final product was analysed using the same techniques used for the undoped materials.

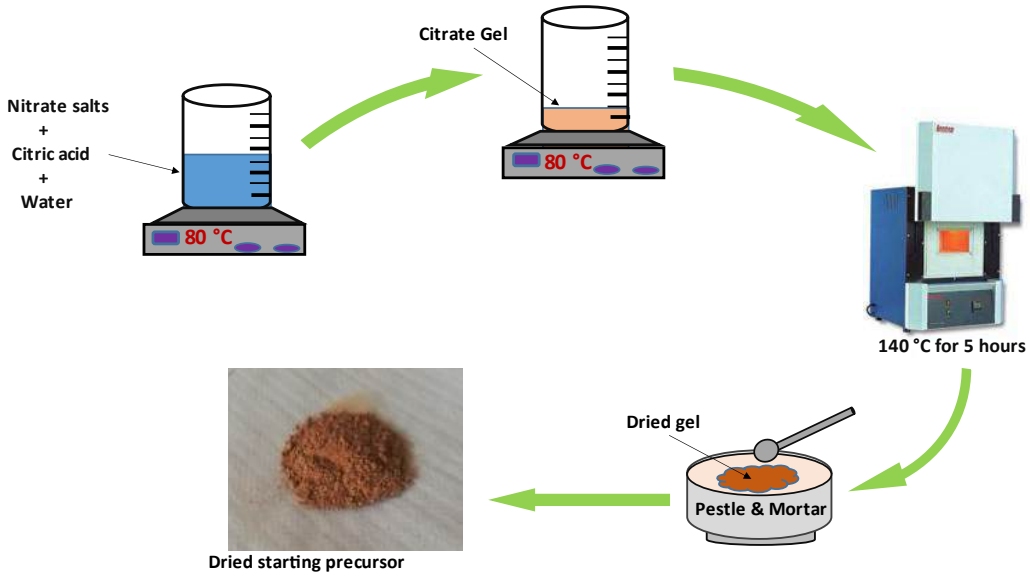

Figure 3.1: Schematic of how the sol-gel synthesis method was utilized.

Thermal decomposition and heat flow profiles of the dried precursor powders were examined to gain insight into the thermal behaviour using simultaneous thermal analysis (STA) that incorporates thermal gravimetric analysis (TGA) coupled with differential thermal analysis (DTA). Based on results from the thermal analysis, the dried precursor gel was calcined in the muffle furnace for 5 hours to produce the final spinel lithium metal oxide cathode material. *Ex-situ* X-ray diffraction techniques were then used to build an understanding of the phase

behaviour and structural insights of these materials as a function of temperature, where materials were heated to a certain temperature, cooled to room temperature and then measure the X-ray diffraction which were analysed using Rietveld refinement.

3.2. Characterization techniques

3.2.1. Thermal analysis

Thermal decomposition and heat flow profiles of dried powder samples were examined by a simultaneous thermal analysis (thermal gravimetric analysis (TGA) coupled with differential thermal analysis (DTA)) using a Perkin Elmer STA 6000 instrument (Fig.3.2) that was designed with a "SaTurnA" sensor, a cutting-edge technology sensor that provides excellent accuracy. The instrument has a highly compact furnace with improved temperature regulation and control. The STA 6000 only allows a small amount (between 10 mg to ~30 mg) of sample to be used for accurate measurements of weight loss and heat flow throughout the heating and cooling cycle where a small alumina crucible was used as it allows high-temperature analysis (± 1000 °C). Temperature calibration on the instrument was performed before measuring the data by melting the indium standard in the alumina crucible. After the calibration, experiments were generally carried out in air at a slow heating rate of 5 °C/min from 30 °C to 800 °C and then cooled in the same way, the data collected were then analysed using the Pyris software. The thermal analysis technique is very useful to study phase diagrams in conjunction with X-ray diffraction to track material phases/ structural changes as a function of temperature.

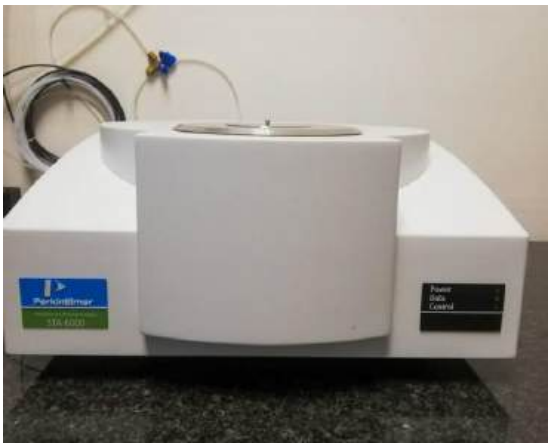

PerkinElmer STA 6000



STA 6000 Furnace

Figure 3.2: PerkinElmer STA 6000 used for thermal analysis with the bottom right picture showing the compact furnace.

In this project, the empty alumina crucible was always first heated from 30 °C to 800 °C and then cooled to room temperature before each sample analysis. Fig.3.3 for example shows a mass loss of ~0.4% which is used to account for any changes within the system itself (without the sample) as a function of temperature. The empty crucible data was subtracted from the actual data when the material was included so as to get the material information alone (by excluding the empty crucible contribution).

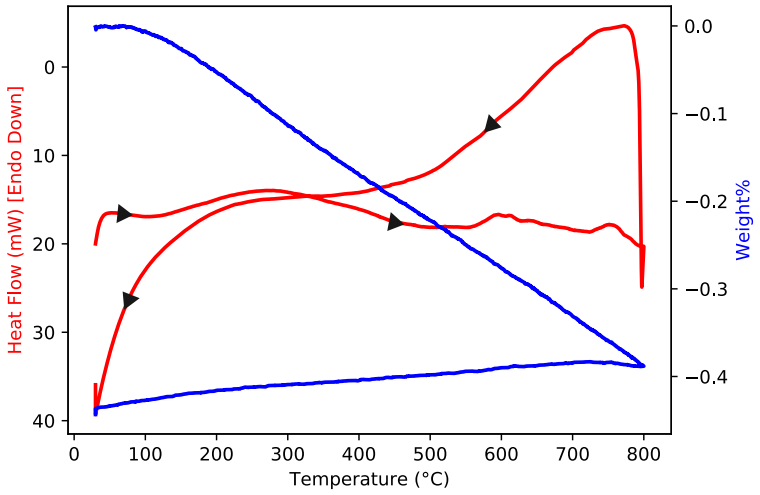

Figure 3.3: Empty crucible STA data heated from 30 °C to 800 °C at 5 °C/min in air.

3.2.2. Powder X-ray diffraction

3.2.2.1. Laboratory X-ray diffraction

A Bruker D2 Phaser diffractometer (Fig.3.4) was used to measure room temperature powder X-ray diffraction patterns using a Bragg-Brentano geometry. The sample was prepared by packing a powder into the cavity of a sample holder and then positioned in the instrument. Co radiation (λ = 1.78897 Å) and the Fe filter were used, these instrument uses Bruker Lynxeye PSD detector which measures an angular range of 5° 2θ and a 2.5° primary and secondary beam Soller slits with 360° rotational sample stage. The instrument is controlled by Bruker Diffract.Commander software. All measurements were done at room temperature in this project, and measurements were taken from 10° to 90° 2θ at 0.4°/step with no spin for 1 hour.

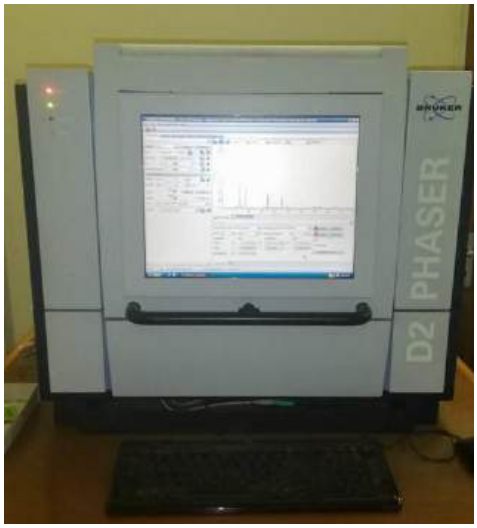

Bruker D2 Phaser diffractometer

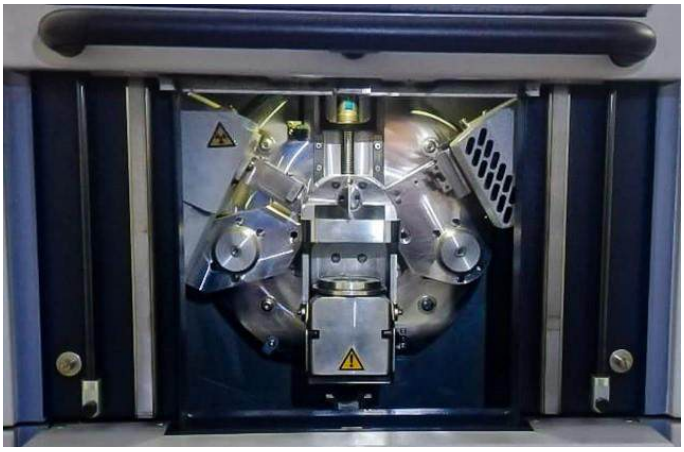

Front opening of the diffractometer

Figure 3.4: Bruker D2 Phaser diffractometer and its front when opened.

3.2.2.2. Synchrotron X-ray diffraction

In this project, the synchrotron measurements for both pair distribution function and room temperature X-ray diffraction data were carried out using a capillary geometry at 28-ID-1 beamlines of the National Synchrotron Light Source ll (NSLS-ll) at the Brookhaven National Laboratory (BNL) which produces higher-resolution data. These X-rays have higher brilliance which gives a high signal-to-noise ratio and allows for small feature detection in data that is useable for precise and accurate Rietveld refinement and small box pair distribution function analysis.

3.2.3. Rietveld refinement and pair distribution function analysis

For qualitative analysis of the PXRD patterns, Diffract.EVA software was used as a fingerprinting tool to identify the phases that are present in the material (measured pattern) against the reference pattern (crystallographic information) obtained from Crystallography Open Database (COD). Rietveld refinement of all crystalline powder materials was carried out to investigate and quantify the phases formed and determine the crystallographic information (lattice parameter and crystallite size).

The structural analysis of the powder diffraction profiles using Rietveld refinement was carried out using Topas-academic V7.13 software. The full pattern Rietveld refinement was performed against the calculated/ reference model (crystallographic information) using Notepad++ to configure starting parameters that can be used in the least square analysis. The conventional Rietveld plot was generated using Python scripts on the open-source software.

The experimental PDF data was reduced (Fourier transformed) using xPDFsuite software. A structural model was then refined in a direct space least-squares refinement using the Topas.

The PDF refinement followed a small box approach which is quicker, and it is relatively similar to Rietveld refinement in nature, however, this approach has few parameters and highly constrained fits which only accounts for small deviations from the average crystal structure as observed in standard XRD. Diffraction data of standard reference material 640d (silicon powder) was refined to obtain the accurate instrumental parameters such as the wavelength.

3.3. Theory on characterization techniques

3.3.1. Simultaneous thermal analysis

Advanced techniques such as simultaneous thermal analysis, that incorporates thermal gravimetric analysis (TGA) and differential thermal analysis (DTA) are available to analyze the weight decomposition and heat flow profiles of powder materials simultaneously [1]. Thermal analyses are critical when analyzing the kinetics of chemical reactions under desired conditions as a function of time or temperature [2]. In the STA instrument, the material is exposed to a controlled temperature environment for both heating and cooling where different atmospheric conditions can be applied such as air, oxygen, and nitrogen gas while recording the TGA and DTA profiles.

TGA is mainly used to understand the decomposition, melting, or polymorphic transitions of powdered materials as a function of temperature. In recent research, DTA has been used to identify solid-state reactions or phase changes in the sample during heating and cooling processes which are expressed in terms of the endothermic and exothermic peaks in the heat flow curve against the temperature profile (Fig 3.5) [3]. The endothermic peaks are ascribed to non-oxidative decomposition reactions as indicated by the negative heat flow, and the exothermic peaks indicate the thermo-oxidative degradation where volatile radicals are driven off from the material in the presence of the purge gas [4]. Both the DTA and TGA are influenced by several parameters such as the weight of the sample used for analysis, the nature of the environment in which the analysis is carried out (i.e. the purge gas used during analysis), and the rate of heating and cooling [3, 5].

When measuring the DTA and TGA profiles of a material, the applied heating rate can affect the accuracy of the measurements at different events, and this depends on the rate of the reaction taking place. An example of the heat flow for a lithiated graphite anode is shown (Fig. 3.5) at heating rates of 5, 10 and 15 °C/min. The slowest heating rate of 5 °C/min provides more detailed events as observed from Fig.3.5, However, when using faster heating rates (such as 10 and 15 °C/min) these increases the rate of reaction and these becomes a disadvantage when investigating reaction kinetics such as crystallization or thermodynamic properties of unstable materials, as some information has been lost as the reaction occurs rapidly while the measurements are taken at a slower rate.

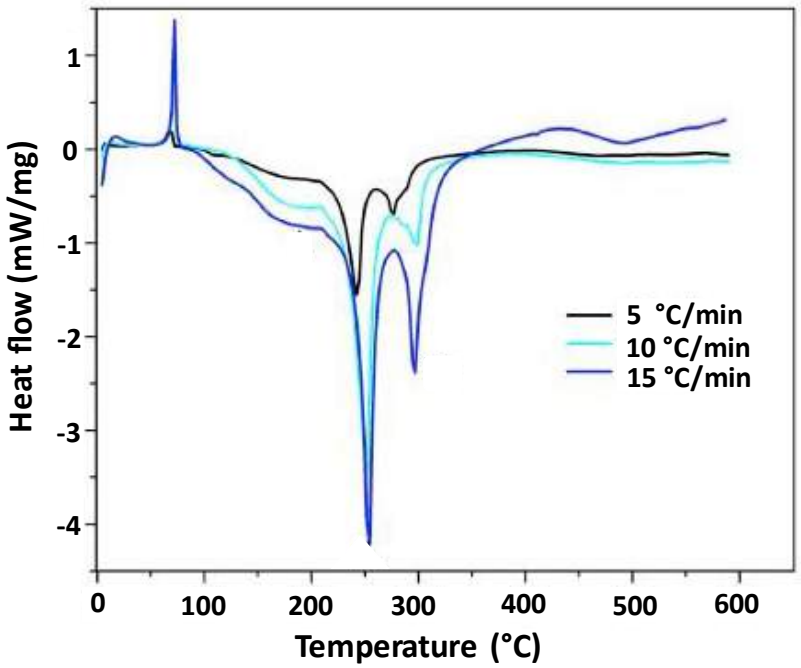

Figure 3.5: Heat flow plots at different heating rates of 5 °C/min, 10 °C/min, and 15 °C/min with the endothermic peaks shown as negative heat flow and exothermic peaks shown as positive heat flow [3].

3.3.2. Powder X-ray diffraction (PXRD)

Powder diffraction is an essential technique in understanding the atomic structure of crystalline materials. The interest in powder diffraction on materials has increased as researchers are now studying complex materials, pharmaceuticals and minerals, as well as doing *in-situ* and *in-operando* studies [6]. Powder diffraction has the advantage of non-destructive analysis, which are rapid and offer simple sample preparation. The powder diffractometer can be fairly flexible as it can allow the laboratory configuration as Bragg-Brentano (flat plate) which is primarily used or Debye-Scherrer (capillary) geometry which can be utilized in different applications [7].

X-rays are electromagnetic waves whose wavelengths are of the order of 10^{-10} m (1 Å) and are typically generated by bombarding a metal with high-energy electrons [8]. When X-rays interact with matter, they can be scattered or absorbed, the scattered waves can undergo destructive interference which results in intensity minima (the waves are out of phase with each other which results in completely destroying the amplitude of the resulting waves), while the waves that are scattered in-phase with each other undergo constructive interference which results in intensity maxima [9].

When the incidence beam of X-rays hits the region of a powder sample, the interference maxima appear as a series of rings (in two-dimension). This information is integrated into a one-dimensional diffraction pattern in reciprocal space in Bragg-Brentano (reflection) and Debye-Scherrer (transmission) geometries [10]. Bragg-Brentano and Debye-Scherrer geometries are similar with the main difference in positioning of X-ray source, and followed

by the mounting of X-ray optics with suitable beam divergence. The transmission geometry is set up in a way that the X-ray source is mounted to the incidence side and the detector is attached on the other side wherein the sample is positioned in a fixed beam path to allow the detector to measure Debye-Scherrer cones to maximise counting statistics. In this work, Bragg-Brentano geometry was used in all laboratory PXRD measurements.

The crystalline materials are made up of atoms with a long-range order in three-dimensional space where the basic repeating units describes the full symmetry of the crystal structure, and this is called the unit cell [11]. The peak positions, peak intensities, peak width, and peak shape yields information about the shape, size, and strain state of the crystallites in powder materials, whereas, the peak position is determined by the unit cell dimensions (the size and shape of the unit cell) while the intensities are related to the atomic coordinates (atomic positions) of the unit cell and these can be determined from diffraction by applying Bragg's equation (Eqn.3.1) [7].

$$n\lambda = 2d_{hkl}sin\theta$$ Equation 3.1: Bragg's law

where: n is the diffraction order, λ is the wavelength of the incident beam, d is the spacing of adjacent crystal lattice planes and θ is Bragg angle/diffraction angle. The wave behaviour of X-rays has been exploited by utilizing X-ray scattering where the atoms are visualized as being arranged in planes with a separation distance (d) between them and with Bragg reflections labelled as (hkl) which are the Miller index labels associated with the respective crystallographic planes. Bragg's law describes the relationship between the wavelength of an incident X-ray beam, the incident angle, and the spacing of adjacent crystal lattice planes.

From the powder diffraction data, structural information can be extracted by qualitative and quantitative analysis (Fig.3.6). Qualitative analysis, known as fingerprinting the phase/s, is useful for phase identification where the experimental pattern is compared to reference patterns in a database, such as the Powder Diffraction File and International Centre for Diffraction Data [12]. If the full powder pattern in the database matches the experimental data, using all peaks in the identification, then the quality of the data is determined using the figure of merit. For samples containing multiple phases, it is often required to determine the different phase compositions using quantitative analysis as this technique is phase sensitive [13].

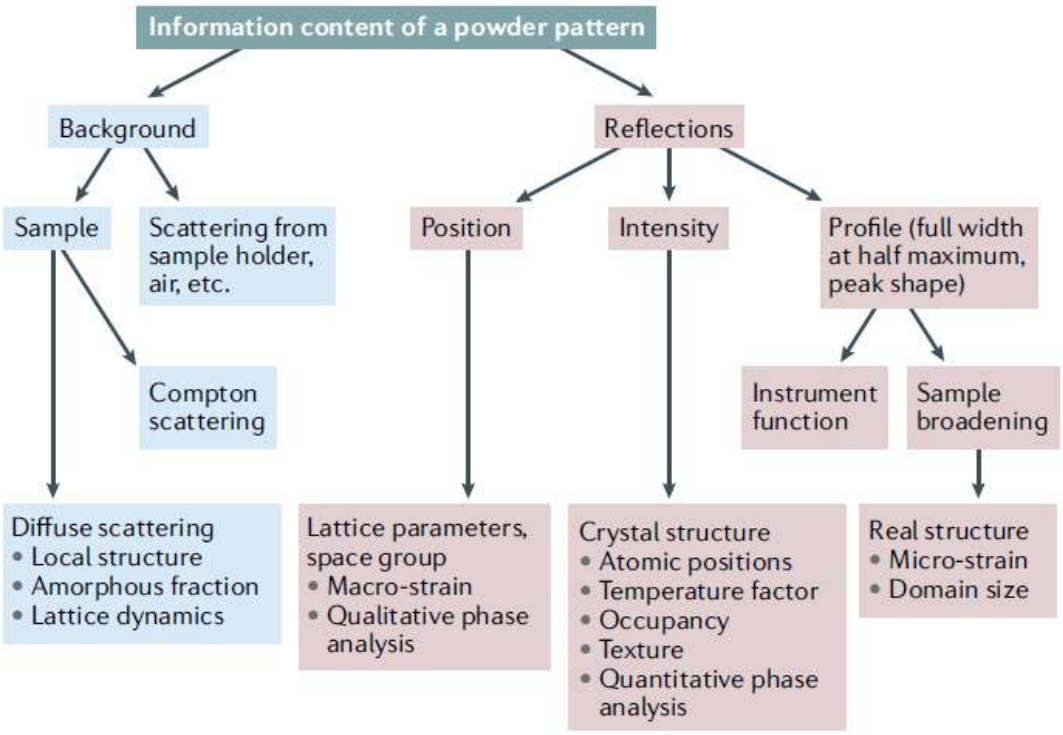

Figure 3.6: Schematic representation of information content of a powder pattern [7].

In-situ diffraction analysis offers an opportunity to understand the actual form of reactions taking place on the material in real time. This information is critical for modifying, controlling and manipulating the reactions to achieve the desired outcome [14]. The advanced powder diffraction instruments can do *in-situ* diffraction measurements, such as variable temperature powder X-ray diffraction (VT-PXRD) which is aimed at studying the phase changes of a solid-state material as a function of temperature, where both intermediate and high-temperature stages are available [15].

3.3.3. Synchrotron techniques

Synchrotron radiation is defined as the electromagnetic radiation emitted by accelerating electrons relatively close to the speed of light (3×10^8 m/s). These electrons are produced by an electron accelerator (electron gun) and then travel through the booster where they are accelerated to the given energy, achieving the multi-GeV level of energy moving at a speed relatively close to the speed of light [16]. The electrons are then ejected into a high vacuum storage ring (several kilometers long) which are then forced to change direction under a magnetic field (using bending magnets, wigglers, and undulators) and then radiate electromagnetic radiation in a narrow cone towards the beamlines. At the beamlines radiation is carried to the experimental end station which incorporates devices appropriate to select wavelength and focus the beam using monochromators, slits, and mirrors as different beamlines have different functionality. A schematic representation of a beamline at a synchrotron is shown in Fig.3.7 [17].

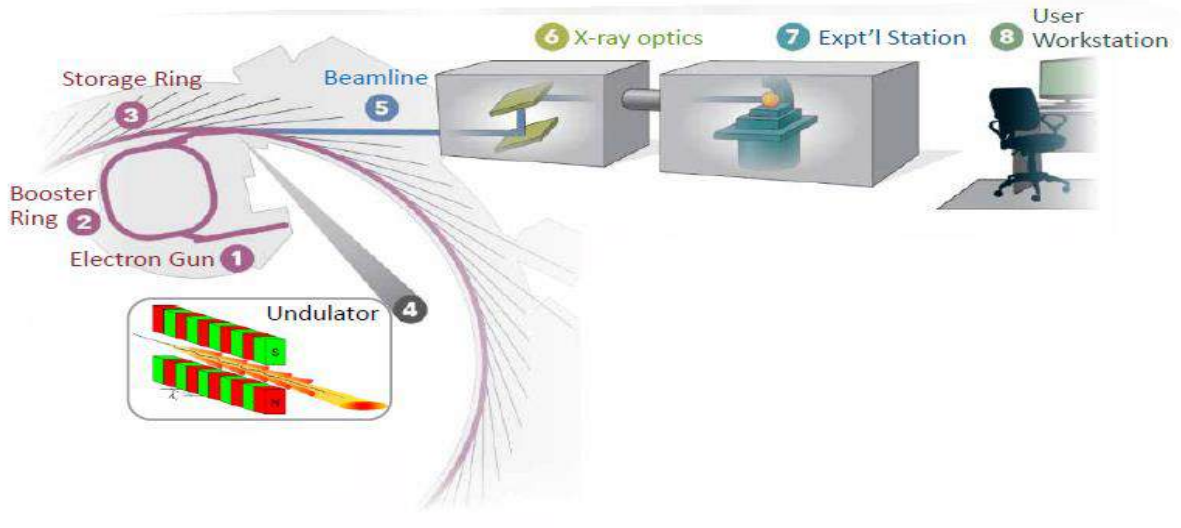

Figure 3.7: Schematic representation of Synchrotron technique.

In generation synchrotrons, the radiation is produced by the bending magnets giving electromagnetic radiation that is a continuous spectrum of wavelengths. In 2nd and 3rd generation synchrotrons, insertion devices such as wigglers and undulators are employed to increase the X-ray beam intensity and these synchrotrons produces high-energy radiations and smaller distribution angles [18].

Synchrotron radiation has high brightness which is more intense than the laboratory sources and this reduces the experimental time and results in a higher resolution data. Synchrotron radiation is highly collimated and has a wide energy spectrum which gives an advantage of measuring XRD pattens with a high signal/noise ratio due to the monochromatic, high flux and highly collimated beams, that allows for complex structural analysis. Capillary geometry is commonly applied in synchrotrons as it is easy to control the sample environment if needed, where the resolution is mainly due to the source (smaller diameter results in higher resolution) and capillaries are easy to align.

3.3.4. Rietveld refinement

Rietveld refinement is a least square approach that optimizes the fit of the experimental observed data by the structure model [19]. This method has Adapted a whole pattern fitting strategy in which the structure model, peak shapes, and background information are used to calculate a powder pattern. The observed intensities, $y_{obs,i}$, at each step in the 2θ is compared to the calculated intensities, $y_{calc,i}$, and the Rietveld algorithm optimizes the parameters used in the model to minimize the sum of the squared differences between the two intensity values using the formula (Eqn.3.2) [20]:

$$\sum_{i=1}^{N} w_i (y_{obs,i} - y_{calc,i})^2$$ Equation 3.2: Minimization

where w_i is the weight. The process is normally followed by monitoring the weighted profile R-factor, R_{wp}, which is scaled by the weighted intensities which have a low value given by:

$$R_{wp} = \sqrt{\frac{\sum_{i=1}^{N} w_i(y_{obs,i} - y_{calc,i})^2}{\sum_{i=1}^{N} w_i(y_{obs,i})^2}}$$ Equation 3.3: Weighted profile R-factor

R_{wp} is a very useful parameter when compared to R_{exp} (the expected R-factor) to see how good the fit is when doing the refinement. R_{exp} uses the number of data points (N) and number of varied parameters (P), where N should be more than P.

$$R_{exp} = \sqrt{\frac{N-P}{\sum_{i=1}^{N} w_i(y_{obs,i})^2}}$$ Equation 3.4: Expected profile R-factor

The goodness of fit (GoF) or χ, relates the statistically expected R_{exp} to the R_{wp}. The closer the GoF value is to 1, the better the refinement. (At the start of a refinement, χ is usually a large value which indicates that refined parameters result in a poor model, whereas when the GoF have the value approaching 1, this results in refined parameters producing a model that has better agreement with the data) where the R-factors are related by:

$$GoF = \chi = \frac{R_{wp}}{R_{exp}} = \sqrt{\frac{\sum_{i=1}^{N} w_i(y_{obs,i} - y_{calc,i})^2}{N-P}}$$ Equation 3.5: Goodness of fit

There are general structural parameters that are refined when fitting the data profile, namely, the fractional atomic coordinates, atomic site occupancy, unit cell parameters, and atomic displacement parameters [21]. These parameters give statistical information about the structure. The instrumental calibration and intensity correction parameters were refined before the structural refinement using the NIST 660c (Lab_6) standard.

3.3.5. Pair Distribution Function (PDF)

The traditional crystallographic structure solution approach, which gives information about the average structure, is insufficient to understand the defects in materials on an atomic scale. The pair distribution function method was originally used to study liquids and amorphous materials which lack lattice periodicity; however, this method can also be used to study disordered crystalline materials [22].

The study of diffuse scattering and Bragg diffraction over a wide range of reciprocal space yields the local atomic arrangements which open a pathway of understanding complex materials. The 1D diffraction pattern of intensities is Fourier transformed from the reciprocal space to the real space in order to achieve the atomic pair distribution function (as shown in detail on Fig.3.8). This is then used to unravel the local structure represented by the probability of finding two atoms in the material some distance (r) apart from each other in both crystalline and non-crystalline materials, which can be understood by the bond length distribution [23, 24].

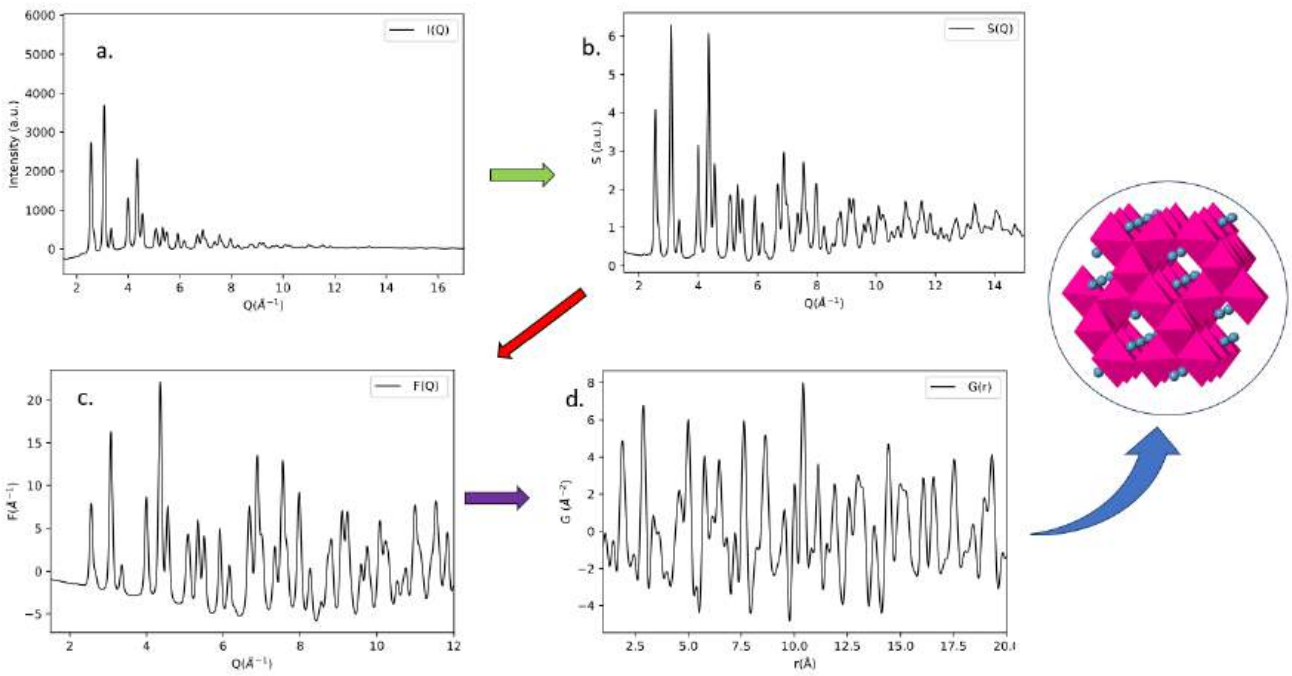

Figure 3.8: Schematic representation of converting powder diffraction data to the pair distribution function. (a) Integration data, (b) normalized scattering intensity $S(Q)$, (c) normalised reduced total scattering structure function $F(Q)$, and (d) atomic pair distribution function (PDF) $G(r)$ with Q being the scattering vector. Adapted from [25].

A total scattering approach is needed to extract the structural information of nanomaterials with a structural domain of less than 10 nm [26]. Mathematically the PDF, $G(r)$, is obtained from the measured powder intensities utilizing a sine Fourier transformation of a normalized scattering intensity, $S(Q)$ [27], given by:

$$G(r) = 4\pi r[\rho(r) - \rho_o]$$

$$= \frac{2}{\pi}\int_{Q_{min}}^{Q_{max}} Q[S(Q) - 1]\sin(Qr)\, dQ \qquad \text{Equation 3.6: Fourier transformation}$$

where $\rho(r)$ is the atomic pair density function, ρ_o is the atomic number density in atoms/Å^3 and Q is the magnitude of the scattering vector S. $Q = 2\pi/d = 4\pi sin\theta/\lambda$ where 2θ is the scattering angle and λ is the wavelength of the radiation that has been used. After calculating the PDF of a structure, it is then possible to explain the local structure by fitting the structure models to the pair distribution function using the regression method, as the $G(r)$ provides fundamental information such as how many atoms are located at a spherical distance r for any given coordination number [28].

In order to obtain a high-resolution local atomic structure, the data should be measured by using instruments with high diffraction angles (large Q_{max}), high energy radiation (short wavelength), good counting statistics, and optimal background suppression. The PDF is the bond length distribution of the material given by the scattering powers of the neighbouring

atoms, where the simple analysis is to find the bond length information and coordination numbers [24].

The instrument setup determines the limits of the Q values that can be accessed experimentally to a range of $Q_{min} \leq Q \leq Q_{max}$. The quality of collimation usually gives the value of Q_{min} as the experimental factors result in an ability to calculate the dispersion of the sample at Q = 0 Å^{-1}. Q_{max} is the termination ripple where there is a decrease in the PDF resolution as the data cannot be Fourier transformed to infinite Q. It is critical to make corrections that have contributed to the scattered intensity from effects including, but not limited to, Compton scattering, scattering from the sample holder, and fluorescence [29].

After the data has been measured, the PDF can be calculated from a structural model by using the relation:

$$Gc(r) = \frac{1}{r}\sum_i \sum_j \left[\frac{b_i b_j}{\langle b \rangle^2}\delta\left(r - r_{ij}\right)\right] - 4\pi r \rho_0$$ Equation 3.7: G(r) PDF from a structure model

where the sum of all pairs of atoms i and j within the model crystal is separated by the radius r_{ij} with the scattering power of (b) of the sample. To gain a deeper understanding of the PDF, the data needs to be refined using more advance modelling methodologies such as Reverse Monte Carlo modelling, Empirical potential structure refinement, theoretical model, or complex modelling [23].

The Reverse Monte Carlo technique is a “big-box” approach that begins with a larger assembly of atoms in a crystallographic model. In this method, atoms can be used to match the structural model containing many atoms on the experimental PDF where the technique selects a random site within the crystal and the system variables that are associated with the site (occupancy or displacements), which then check the constrains and then compute the goodness of fit, if the GOF has reduced, the loop continues to select another atom until the convergence [28]. The large-box approach can be used to model longer-range effects such as the amorphous materials. The small box method (real space crystal structure refinements) uses the least number of parameters to describe the structure and can be utilized when looking for a small deviation from an ordered crystal structure that relates to a single unit cell which has been reduced to lower symmetry [29].

3.4. References

[1] S. Arvelakis, P. A. Jensen and K. Dam-Johansen, “Simultaneous thermal analysis (STA) on ash from high-alkali biomass,” *Energy & Fuels,* vol. 18, pp. 1066-1076, 2004.

[2] S. Windisch-Kern, A. Holzer, C. Ponak, T. Hochsteiner and H. Raupenstrauch, “Thermal analysis of lithium ion battery cathode materials for the development of a novel pyrometallurgical recycling approach,” *Carbon Resources Conversion,* vol. 4, pp. 184-189, 2021.

[3] A. Kriston, I. Adanouj, V. Ruiz and A. Pfrang, “Quantification and simulation of thermal decomposition reactions of Li-ion battery materials by simultaneous thermal analysis coupled with gas analysis,” *Journal of Power Sources,* vol. 435, pp. 226774-226787, 2019.

[4] P. R. Day, J. Xia, R. Petibon, J. Rucska, H. Wang and A. T. Wright, “Differential thermal analysis of li-ion cells as an effective probe of liquid electrolyte evolution during aging,” *Journal of The Electrochemical Society,* vol. 162, pp. 2577-2581, 2015.

[5] Y. Huang, Y.-C. Lin, D. M. Jenkins, N. Chernova, Y. Chung, B. Radhakrishnan, I.-H. Chu, J. Fang, Q. Wang, F. Omenya, S. P. Ong and S. M. Whittingham, “Thermal stability and reactivity of cathode materials for li-ion batteries,” *ACS Applied Materials & Interfaces,* vol. 8, pp. 7013-7021, 2016.

[6] X.-Q. Yang, J. McBreen, W.-S. Yoon and C. P. Grey, “Crystal structure changes of $LiMn_{0.5}Ni_{0.5}O_2$ cathode materials during charge and discharge studied by synchrotron based in situ XRD,” *Electrochemistry Communications,* vol. 4, pp. 649-654, 2002.

[7] J. A. Kaduk, S. J. Billinge, R. E. Dinnebier, N. Henderson, I. Madsen, R. Černý, M. Leoni, L. Lutterotti, S. Thakral and D. Chateigner, “Powder diffraction,” *Nature Reviews,* vol. 1, pp. 77-99, 2021.

[8] P. Atkins and J. de Paula, Atkin's Physical chemistry, Ninth Edition, New York: W.H. Freeman and Company, 2010.

[9] J. Walker, D. Halliday and R. Resnick, Principles of physics tenth edition, Europe: John Wiley & Sons, Inc, 2014.

[10] S. T. Thornton and A. Rex, Modern Physics for Scientists and Engineers, Mexico: Cengage Learning, 2019.

[11] N. Fleck, H. Amli, V. Dhanak and W. Ahmed, “Characterization techniques in energy generation and storage,” *Emerging Nanotechnologies for Renewable Energy,* vol. 1, pp. 259-285, 2021.

[12] E. Garnier, "Powder Diffraction. Theory and Practice"., *Cambridge: RSC Publishing*, vol. 1, 2009.

[13] J. S. Evans and I. R. Evans, "Structure analysis from powder diffraction data: Rietveld refinement in excel," *Jornal of Chemical Education*, vol. 1, no. 1, pp. 1-11, 2020.

[14] W. Zhu, D. Liu, A. Paolella, C. Gagnon, V. Gariépy, A. Vijh and K. Zaghib, “Application of operando x-ray diffraction and raman spectroscopies in elucidating the behavior of cathode in lithium-ion batteries,” *Frontiers in Energy Research,* vol. 6, no. 66, pp. 1-16, 2018.

[15] Y. Luo, Y. Zhang, L. Yan, J. Xie and T. Lv, “Octahedral and porous spherical ordered $LiNi_{0.5}Mn_{1.5}O_4$ spinel: the role of morphology on phase transition behavior and electrode/ electrolyte interfacial properties,” *ACS Applied Materials Interfaces,* vol. 10, pp. 31795-31803, 2018.

[16] H. Cheng, C. Lu, Y. Yan, J. Liu, X. Han, H. Jin, Y. Wang, Y. Liu and C. Wu, “Synchrotron radiation X-ray powder diffraction techniques applied in hydrogen storage materials - A review,” *Progress in Natural Science: Materials International,* vol. 27, pp. 66-73, 2017.

[17] P. S. Rahimabadi, M. Khodaei and K. R. Koswattage, “Review on applications of synchrotron-based X-ray techniques in materials characterization,” *Journal of Dentistry,* pp. 1-26, 2020.

[18] H. Iwamoto, “Synchrotron radiation x-ray diffraction techniques applied to insect flight muscle,” *International Journal of Molecular Sciences,* vol. 1, pp. 1-19, 2018.

[19] J. S. Evans and I. R. Evans, “Structure analysis from powder diffraction data: rietveld refinement in excel,” *Journal of Chemical Education,* vol. 1, pp. 1-11, 2020.

[20] R. E. Dinnebier, Y. Liebold-Ribeiro and M. Jansen, "The low and high temperature crystal structures of $[Mg(H_2O_6)]XBr_3$ double salts(X= Rb, Cs) " *Journal of Inorganic,* vol. 634, pp. 1857-1862, 2008.

[21] “R factors in rietveld analysis: how good is good enough,” *International Centre for Diffraction Data,* vol. 21, no. 1, pp. 67-70, 2006.

[22] T. Proffen, S. J. Billinge, T. Egami and D. Louca, “Structural analysis of complex materials using the atomic pair distribution function – a practical guide,” *Journal of Inorganic Chemistry.,* vol. 218, pp. 132-143, 2002.

[23] S. J. Billinge and M. Terban, “Structural analysis of molecular materials using the pair distribution function,” *Chemical Reviews,* vol. 122, pp. 1208-1272, 2022.

[24] X. Wang, S. Tan, X.-Q. Yang and E. Hu, “Pair distribution function analysis: fundamentals and application to battery materials,” *Chinese Physics B,* vol. 29, no. 2, pp. 28802-28813, 2020.

[25] S. J. Billinge, “The rise of the X-ray atomic pair distribution function method: a series of fortunate events,” *Philosophical Transactions A,* vol. 1, pp. 1-14, 2019.

[26] X. Wang, S. Tan, X.-Q. Yang and E. Hu, “Pair distribution function analysis: Fundamentals and application to battery materials,” *Chinese Physics B,* vol. 29, no. 2, pp. 1-20, 2019.

[27] S. J. Billinge, “21ST century challenges: structure beyond crystals,” *IUCr Newsletter,* vol. 27, no. 4, pp. 1-17, 2019.

[28] M. W. Terban and S. J. Billinge, “Structural Analysis of Molecular Materials Using the Pair Distribution Function,” *Chemical Reviews,* vol. 122, pp. 1208-1272, 2022.

[29] S. J. Billinge and M. G. Kanatzidis, “beyond crystallography:the study of disorder, nanocrystallinity and crystallographically challenged materials with pair distribution functions,” *Chemical Communications,* vol. 1, pp. 749-760, 2004.

Chapter 4: A detailed investigation on the decomposition of the precursor materials

Undoped and Al-doped lithium manganese metal oxide ($Li_{1.03}Mn_{1.97}O_4$ and $LiAl_{0.4}Mn_{1.6}O_4$, respectively) precursors were synthesized using the citrate sol-gel method with metal nitrate or metal acetate salts as starting materials, as described in chapter 3 (section 3.1). The precursors analysed here were obtained by drying the gels formed at 140 °C for 5 hours in air. The analysis began by examining the crystallographic structure of the precursor, followed by the thermal analysis using differential thermal analysis and thermogravimetric analysis from room temperature to 800 °C, some of the undoped concentration samples was not studied for the doped material due to the TGA analysis which shows a slight difference on the mass loss of the material with the aim of studying the material with less mass loss on the flow cell.

4.1. Investigation of precursors prepared using nitrate salts

4.1.1. Laboratory XRD of Undoped precursor

Precursors synthesised using various total metal ion to citric acid concentration ratios ($[M_T]$:[Cit] as described in Table.4.1) were explored to understand the effect of citrate and to determine the minimum amount of citric acid required to successfully synthesize $Li_{1.03}Mn_{1.97}O_4$. The idea for future studies, is that the starting precursor would be analysed using *in-situ* XRD by placing it in a capillary and then heating it to 700 - 800 °C. The mass loss should be as low as possible to ensure sufficient sample remains in the capillary to be detected and remain in the X-ray beam.

Table 4.1: The $[M_T]$:[Cit] used to prepare undoped precursor materials using the sol-gel method.

Sample ID	$[M_T]$:[Cit]
$Li_{1.03}Mn_{1.97}O_4$	1:1.667
	1:1
	1:0.833
	1:0.667
	1:0.5

The X-ray diffraction patterns of these undoped precursor materials show the formation of a crystalline phase, easily observed by visual inspection of these patterns (Fig.4.1). These diffraction patterns have comparable peak positions and peak shapes, however, when increasing the concentration of the complexing agent, an increase in the number of counts (i.e. the peak intensity) was noticed with ▲ in Fig.4.1 clearly showing an increase in the number of counts as [Cit] is increased. For the sample with the lowest concentration of complexing agent ($[M_T]$: [Cit] = 1:0.5), the diffraction pattern has a peak at ~29° 2θ (indicated by ★ in Fig.4.1) which was not evident in the patterns for the samples with higher

concentrations of citric acid. This could be an indication of excess manganese nitrate or lithium nitrate. Kwon *et al.* [1] reported an excess lithium acetate ($C_2H_3LiO_2$) when calcining $LiMn_2O_4$ at 600 °C while Berbenni *et al.* [2] reported an excess Mn_3O_4 in $LiMn_2O_4$ when preparing the cathode material with Li_2CO_2-$MnCO_3$ mixtures (X_{Li}= 0.1-0.33) calcined at 850 °C.

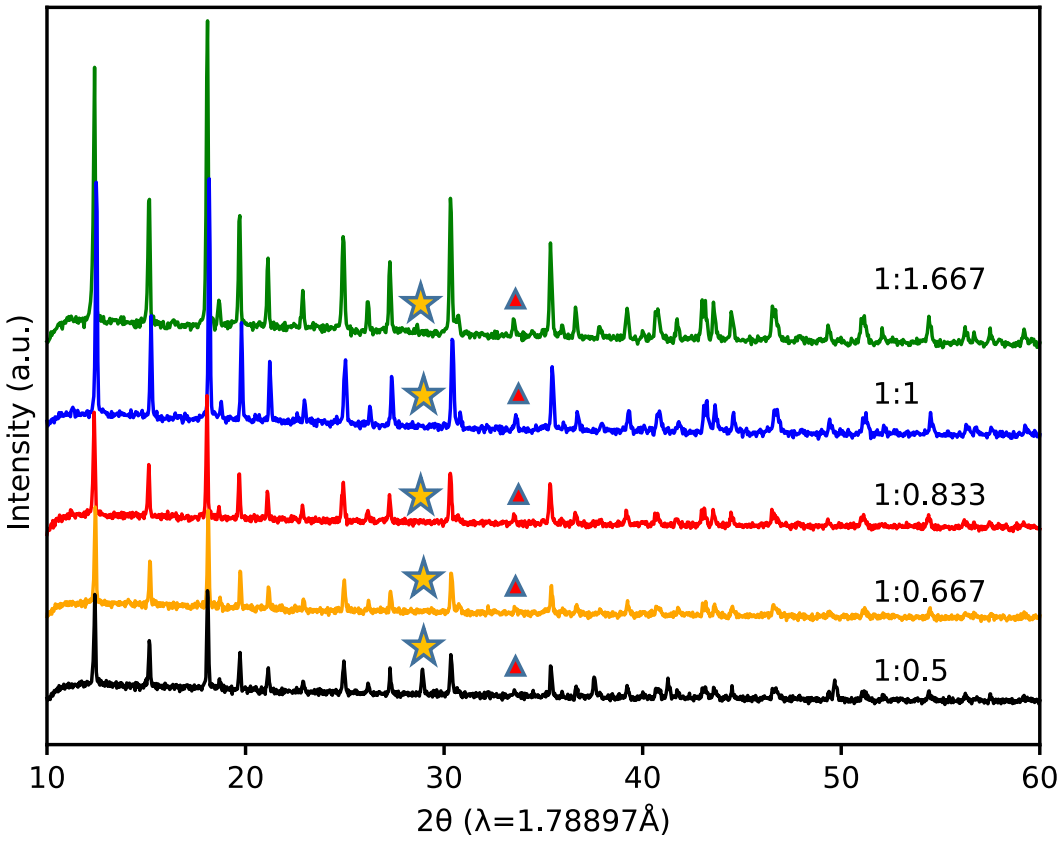

Figure 4.1: Powder X-ray diffraction patterns of precursors for undoped lithium manganese oxide prepared using nitrate salts and differing [M_T]:[Cit] as indicated. Major discrepancies between the patterns are indicated by ★ and ▲.

The qualitative analysis (fingerprinting) of the diffraction pattern for the precursor with [M_T]:[Cit] = 1:1.667 reveals a single phase of Δ-aqua-S-citrato(2-)-manganese(II) (with chemical formula [$Mn(C_6H_6O_7)(H_2O)$]) being present, this phase has an orthorhombic crystal system and a *P*222 space group. The structure (Fig.4.2) shows that the citrate ligand chelates with Mn(ll) through the alpha-hydroxyl group and one oxygen atom from both the alpha and beta-carboxyl groups. When arranged in a crystal lattice, the second oxygen atom from the beta-carboxyl group remains uncoordinated, while that of the alpha-carboxyl group is bonded to an adjacent Mn atom, leading to octahedrally coordinated Mn and a helical chain [3].

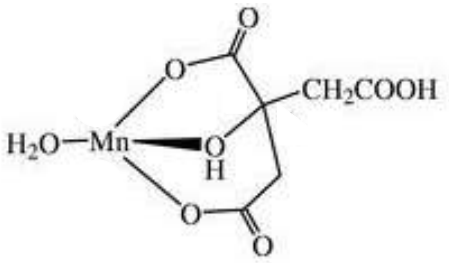

Figure 4.2: Chemical structure of Δ-Aqua-S-citrato(2-)-manganese(II) [3, 4].

The quantitative analysis (Rietveld refinement) of the diffraction pattern for the [M_T]:[Cit] = 1:1.667 precursor based on the Δ-aqua-S-citrato(2-)-manganese(ll) phase supports the presence of this single phase (Fig.4.3) as there is good agreement between the calculated and experimental data (i.e. peak positions, shapes and intensities were all aligned). This was confirmed by the difference plot, where only minor discrepancies were noted, mainly on the first three peaks, which might be related to preferred orientation. From the statistical analysis (Table.4.2), a goodness of fit (GOF) value of 1.31 indicates a good quality refinement (GOF should approach 1).

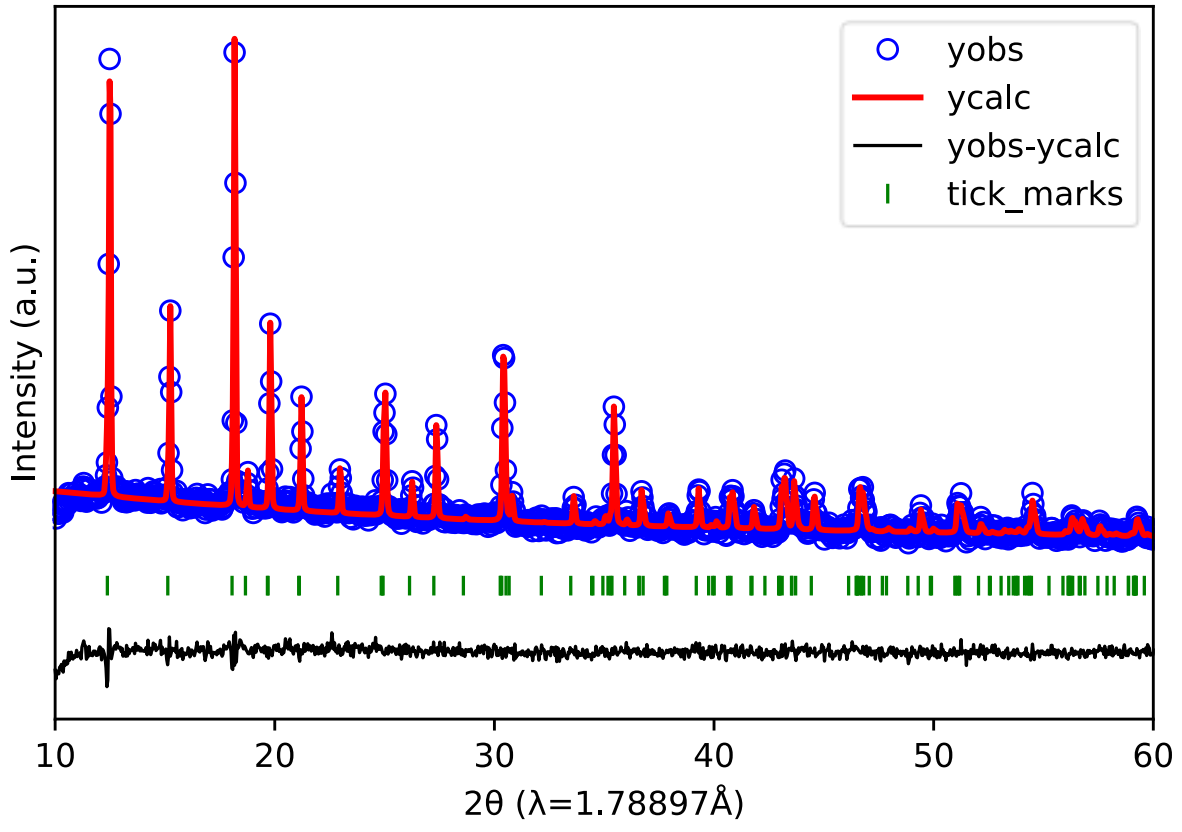

Figure 4.3: Rietveld refinement of the precursor with [M_T]:[Cit] = 1:1.667. The pattern obtained from the experimental data (yobs) is shown in blue, the calculated model (ycalc) in red, and difference plot which represents the difference between the observed and the calculated model (yobs-ycalc) in black. The tick marks in green shows the calculated peak positions correspond to orthorhombic phase for Δ-aqua-S-citrato(2-)-manganese(II).

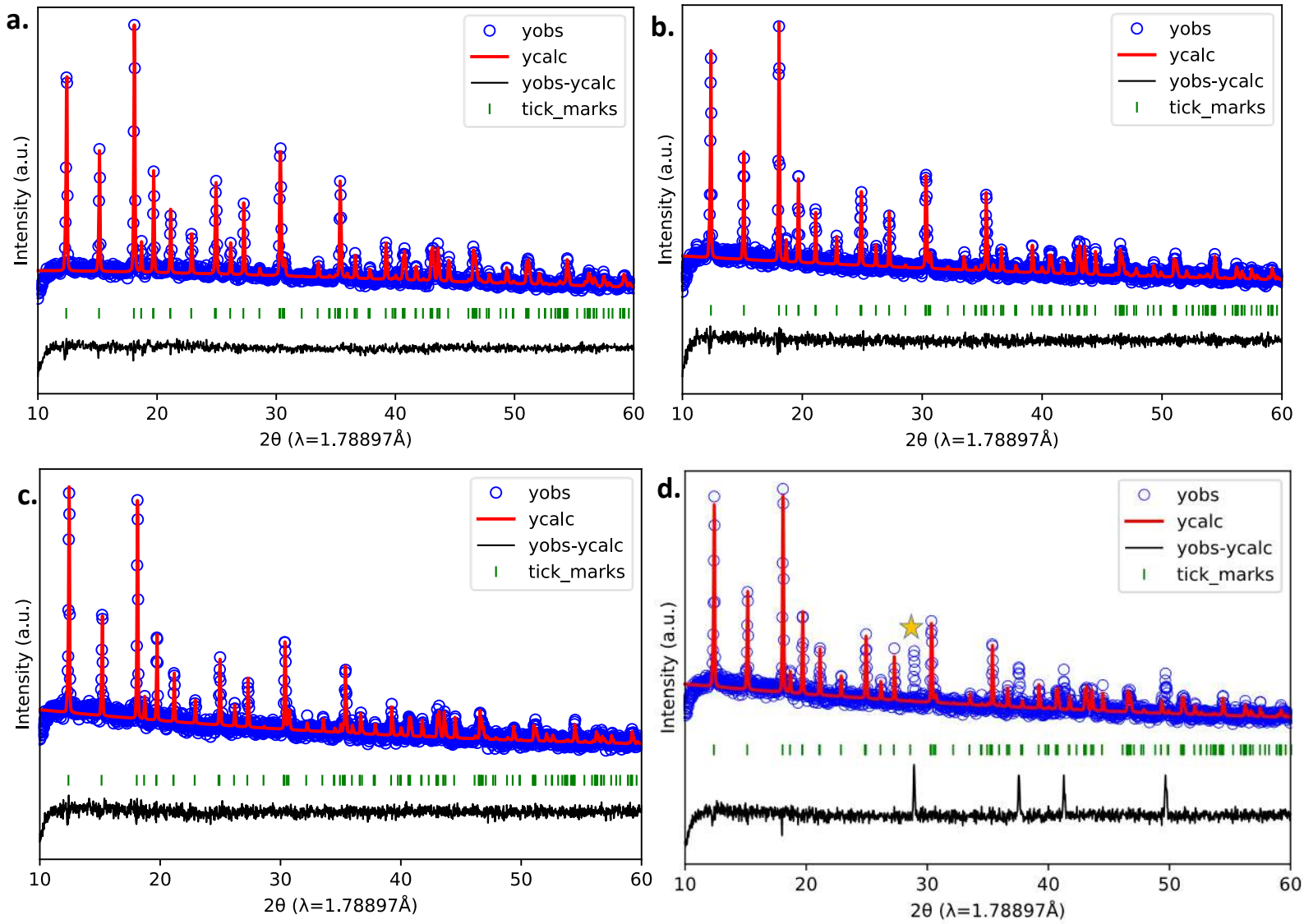

Figure 4.4: Rietveld refinements of precursors with [M_T]: [Cit] of (a.) 1:1, (b.) 1:0.833, (c.) 1:0.667 and (d) 1:0.5. The tick marks correspond to orthorhombic phase for Δ-aqua-S-citrato(2-)-manganese(II). The peak indicated by ★ corresponds to that in Fig. 4.1.

The overall Rietveld refinements of the diffraction patterns for precursors with [M_T]:[Cit] of 1:1, 1:0.833 and 1:0.667 (Fig.4.4 (a - c)) exhibited a similar outcome, revealing the formation of Δ-aqua-S-citrato(2-)-manganese(II) (an orthorhombic system with space group *P*222) with no detectable impurity phases. However, it was observed that the concentration of complexing agent directly influences the crystal growth of the material, with a decrease in the complexing agent concentration resulting in low peak intensities, implying reduced crystallinity. The statistical GOF also showed an improved calculated fit when reducing the citric acid concentration (Table.4.2).

When reducing the concentration of the complexing agent concentration such that [M_T]:[Cit] = 1:0.5, the Rietveld refinement (Fig.4.4(d)) revealed a mixture of phases of Δ-aqua-S-citrato(2-)-manganese(II) ([$Mn(C_6H_6O_7)(H_2O)$]) of an orthorhombic system (with space group *P*222) and lithium nitrate ($LiNO_3$) of a rhombohedral crystal system (with space group *R*3*C*). Using both Δ-aqua-S-citrato(2-)-manganese(II) and lithium nitrate in the model resulted in a statistical GOF of 1.24 as indicated in Table 4.2 (a GOF value of 1.50 was obtained when LiNO3 was omitted from the model). Reducing the [Cit] results in a general decrease crystallite size and increase unit cell volume.

Table 4.2: Refined structural parameters of the undoped precursor material Rwp, Rexp and GOF are the statistical fit parameters described in chapter 3 section 3.3.4.

[M_T]:[Cit]	Space group	Lattice parameter			Rexp	Rwp	GOF	Crystallite size(μm)	Volume (Å^3)
		a(Å)	b(Å)	c(Å)					
1:1.667	*P*222	6.0398(3	10.4737(2)	13.5896(2)	0.92	1.22	1.31	6.98(1)	859.66(2)
1:1	*P*222	6.0383(5)	10.4698(4)	13.5892(1)	0.89	1.16	1.30	6.73(5)	859.11(2)
1:0.833	*P*222	6.0363(1)	10.4679(2)	13.5827(5)	1.11	1.36	1.22	6.62(3)	858.26(3)
1:0.667	*P*222	6.0375(2)	10.4701(4)	13.5831(3)	1.11	1.29	1.15	6.68(4)	858.44(5)
1:0.5	*P*222 *R3C*	6.0364(4) 5.7579(4)	10.4672(9) 5.7579(4)	13.5802(1) 48.1200(6)	1.11	1.38	1.24	6.52(2)	544.21(8)

The Rietveld refinement of the XRD patterns has resulted in an agreement between the calculated and the observed patterns as this can be seen by visually inspecting the Rietveld patterns which show fewer discrepancies on the difference plot between the observed and calculated patterns, however, at lower concentration of the complexing agent, impure starting material precursor can be observed.

4.1.2. Laboratory XRD of Al-doped precursor.

The precursor material for aluminium doped lithium manganese metal oxide ($LiAl_{0.4}Mn_{1.6}O_4$) was also prepared by dissolving stoichiometric amounts of nitrate salts with various concentrations of citric acid (shown in Table.4.3).

Table 4.3: The [M_T]:[Cit] used to prepare Al-doped precursor materials using the sol-gel method.

Sample ID	[M_T]:[Cit]
$LiAl_{0.4}Mn_{1.6}O_4$	1:1.667
	1:1
	1:0.667

The room temperature diffraction patterns of these Al-doped lithium manganese oxide dried gel precursor (Fig.4.5.) showed that amorphous phases were formed when introducing the Al-dopant in the cathode material. Amorphous materials are materials that have no order in the arrangement of atoms and thus leading to diffraction patterns that does not exhibit any peaks.

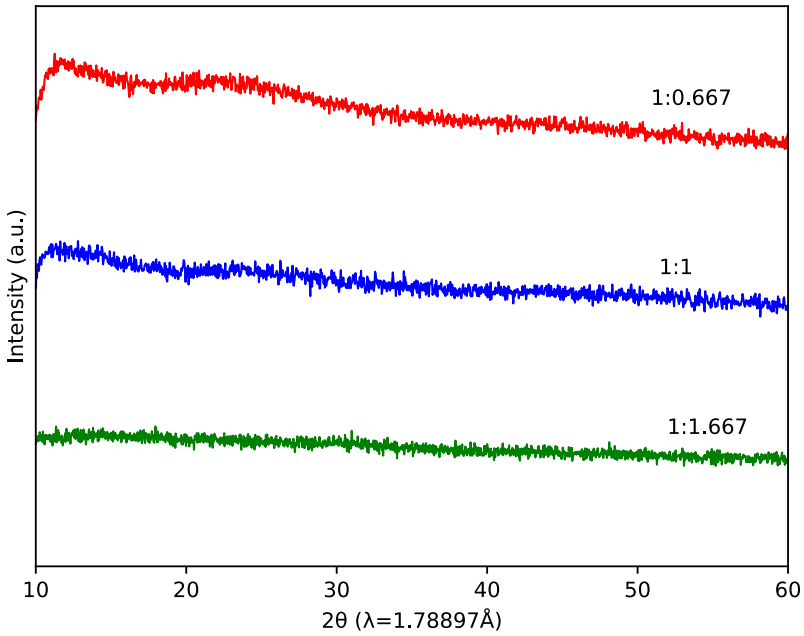

Figure 4.5: Powder X-ray diffraction patterns of the dried precursor of Al-doped lithium manganese oxide.

4.1.3. STA analysis of Undoped starting material precursor

STA (which incorporates DTA and TGA) measurements were run using a slow scan rate of 5 °C/min from 30 °C to 800 °C for all the precursors synthesised using varying [M_T]:[Cit]. The results for the undoped samples are present here. In all cases, the data collected from a blank crucible, as determined just before the measurement of the sample, was subtracted from the data collected of the material in that crucible to negate any crucible effects.

The precursor with [M_T]:[Cit] = 1:1.667 produced a heat flow curve (Fig.4.6) with a very small endothermic peak at ~280 °C (indicted by *1*) which was likely due to trapped (water of crystallisation) or strongly adsorbed moisture within the precursor material. This endothermic peak was also observed by Hashem *et al.* [5] when synthesising the $LiMn_2O_4$ spinel. This was followed by two exothermic peaks between 300 – 400 °C which is related to the

decomposition of nitrates and organic materials (indicated by *2* and *3*, respectively) to form released gases such as CO_2 and NOx (where NOx refers to NO or NO_2). The release of these gases is similar to the reported decomposition of nitrates by Malecka *et al.* [6]. There was no further significant endo- or exothermic reactions upon further heating or during the cooling cycle which seems to indicate that the material is stable after the initial decomposition stage and during the timeframe of the measurement. The downward trend in the heat flow above 400 °C shows the material absorbing heat and is related to its heat capacity.

The TGA curve (Fig.4.6) showed multiple weight loss decomposition steps (indicated by *ii – v*) mainly from about 150 °C to 380 °C, after which there was no further mass loss when heating the material to 800 °C. Some mass loss also occurs below 100 °C (indicated by *i*) which is simply from moisture that was absorbed on the material. The mass loss in Fig.4.6(*ii*) shows the removal of entrapped H_2O in the precursor where Fig.4.6(*iii*) could be related to the decomposition of the complexing agent where the crystalline precursor (synthesised using nitrate salts) converts to the amorphous material. Mohamed *et al.*[7] and Snyders *et al.*[8] show the evolution of the phase transition where materials changed phases from the crystalline precursor to amorphous intermediate phase, and then finally formed the spinel cathode oxide. The two closely spaced mass loss steps above ~300 °C (indicated *iv* and *v*) correspond to the decomposition of nitrates and organic components, and clearly correspond to the exothermic processes *2* and *3*, respectively. Both the TGA and DTA curves suggest that the formation of the metal oxide has occurred by ~400 °C, with no further reactions or decompositions taking place above this temperature.

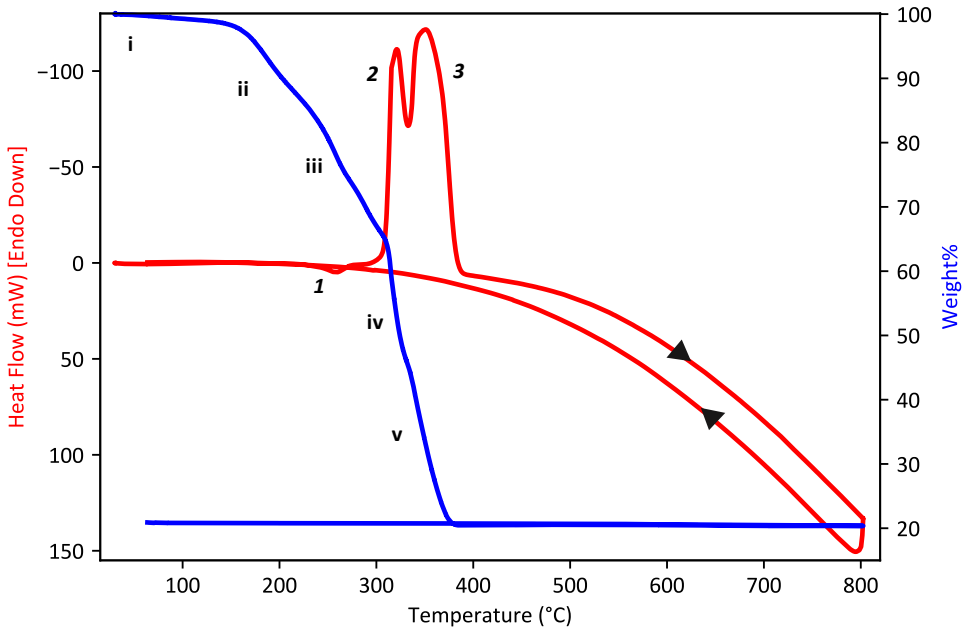

Figure 4.6: DTA (red) and TGA (blue) plots of the precursor for undoped lithium manganese oxide with $[M_T]$:[Cit] = 1:1.667.

The DTA curves in Fig.4.7 for $[M_T]$:[Cit] = 1:1 (a), 1:0.833 (b) and 1:0.667 (c) confirm a similar reaction mechanism as was seen Fig.4.6 for $[M_T]$:[Cit] = 1:1.667 where the labels (*1 – 3* and *i*

– *v*) are used to indicate the same processes. In some cases, two distinct steps are not clearly visible in the TGA curves (e.g. processes *iii* and *iv* in Fig. 4.7(a) and (b)), thus these are labelled together. The DTA curve for $[M_T]$:[Cit] = 1:1 (Fig.4.7(a)) shows more overlap between the peaks *2* and *3* (representing the decomposition of nitrate and organic components), probably due to significantly less citrate being present. These two peaks become more resolved when even less citrate is added (Fig.4.7(b) and (c)) and peak *3* is not so broad. Unexpectedly, peak *2* in Fig.4.7(b) is split which shows nitrates about to fully decompose and beginning decomposition of organics occurring at the same time. In Fig.4.7(c) the mass loss processes labelled *iv* and *v* (corresponding to peaks *2* and *3*, respectively) also become resolved and it is evident that the % loss for process *v* is lower than that for process *iv*; the opposite to that observed in Fig.4.6 when a large excess of citrate was present.

The DTA curves of materials prepared with low citric acid concentrations (Fig.4.7(b) and (c)), show that when these materials were heated above 400 °C, smooth curves were no longer obtained. Fig.4.7 shows the exothermic peaks shift to lower temperatures as a lower concentration of citric acid is added. The number of humps (indicated as *4*) seem to imply some reaction is still occurring and that the lithium manganese oxide is not fully formed (i.e. there are impurity phases still present) or that some phases are still reacting at these higher temperatures. These humps were not instrument artifacts since the same behaviour was noted when the measurements were repeated a few times. Huang *et al.*[9] also showed this instability when investigating the thermal stability of $Li_{0.1}Ni_{0.8}Co_{0.15}Al_{0.05}O_2$ charged electrode.

Since the aim was to see to what extent the mass loss can be reduced to enable *in-situ* variable temperature XRD measurements, the total mass loss was compared for these samples. Fig.'s 4.6 and 4.7 confirmed that when reducing the concentration of citric acid, a smaller overall mass loss is noted. This is expected since it is the citrate and nitrate that is lost upon heating to form the oxide materials. For $[M_T]$:[Cit] = 1:1.667, a total mass loss of 80% is seen, while it was only ~70% for $[M_T]$:[Cit] = 1:1 and ~65% for $[M_T]$:[Cit] = 1:0.667. Even for the lower citrate concentrations. This was also illustrated by Maino *et al.*[10] which showed that when annealing materials with low concentration of complexing agent will result in a higher product yield.

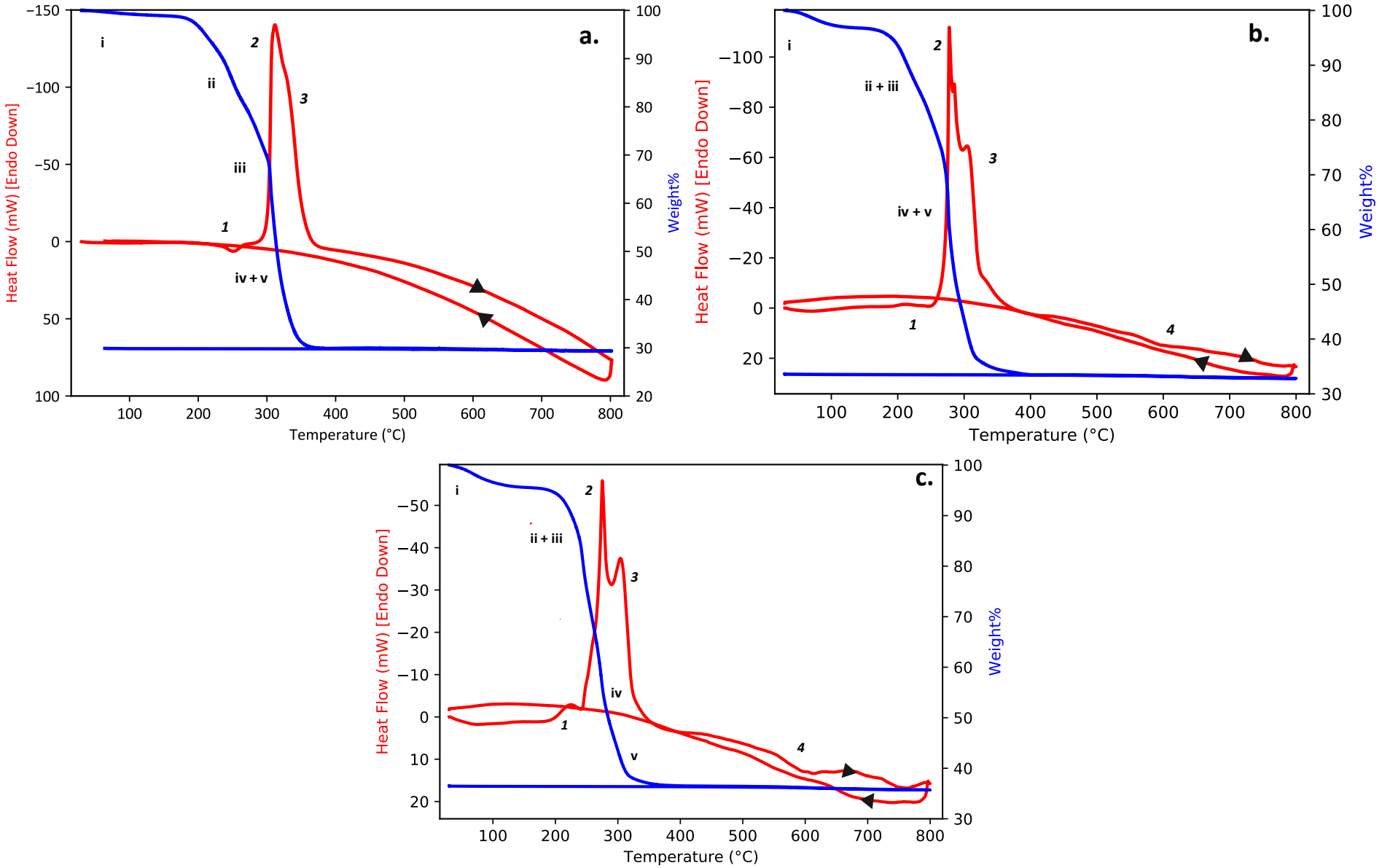

Figure 4.7: DTA and TGA plots of the precursors for undoped lithium manganese oxide synthesised with [M_T]:[Cit] of (a) 1:1, (b) 1:0.833 and (c) 1:0.667.

4.1.4. STA analysis of Al-doped starting precursor

When doping the lithium manganese oxide with aluminium with the aim to produce $LiAl_{0.4}Mn_{1.6}O_4$, the XRD patterns showed that amorphous precursors form for various $[M_T]$:[Cit] (Fig.4.5). The TGA curves (Fig.4.8(a-c)) showed mass loss at *i* indicating removal of absorbed H_2O on the precursor. The mass loss between ~200-300 °C (labelled as *iii*) seems to be a single process (unlike that seen for the undoped samples) and it is mostly likely due to no waters of crystallisation being present as the materials were amorphous. Processes labelled *iv* and *v* were due to the decomposition of organic and nitrate components as before. A similar decomposition step was noted by Snyders *et al*.[8] which shows the decomposition materials of amorphous precursors occurring as a single process.

The DTA curve in Fig.4.8(c) with $[M_T]$:[Cit] = 1:0.667 showed the formation of humps (indicated *4*), as was previously seen for samples with very low citric acid concentrations, which might be due to thermal instability of the product and an excess $LiNO_3$. The total mass loss for all these samples was close to 65%, due to less decomposition citric acid to form CO_2 and H_2O gases, the reaction confirmed by Prosini *et al*. [11].

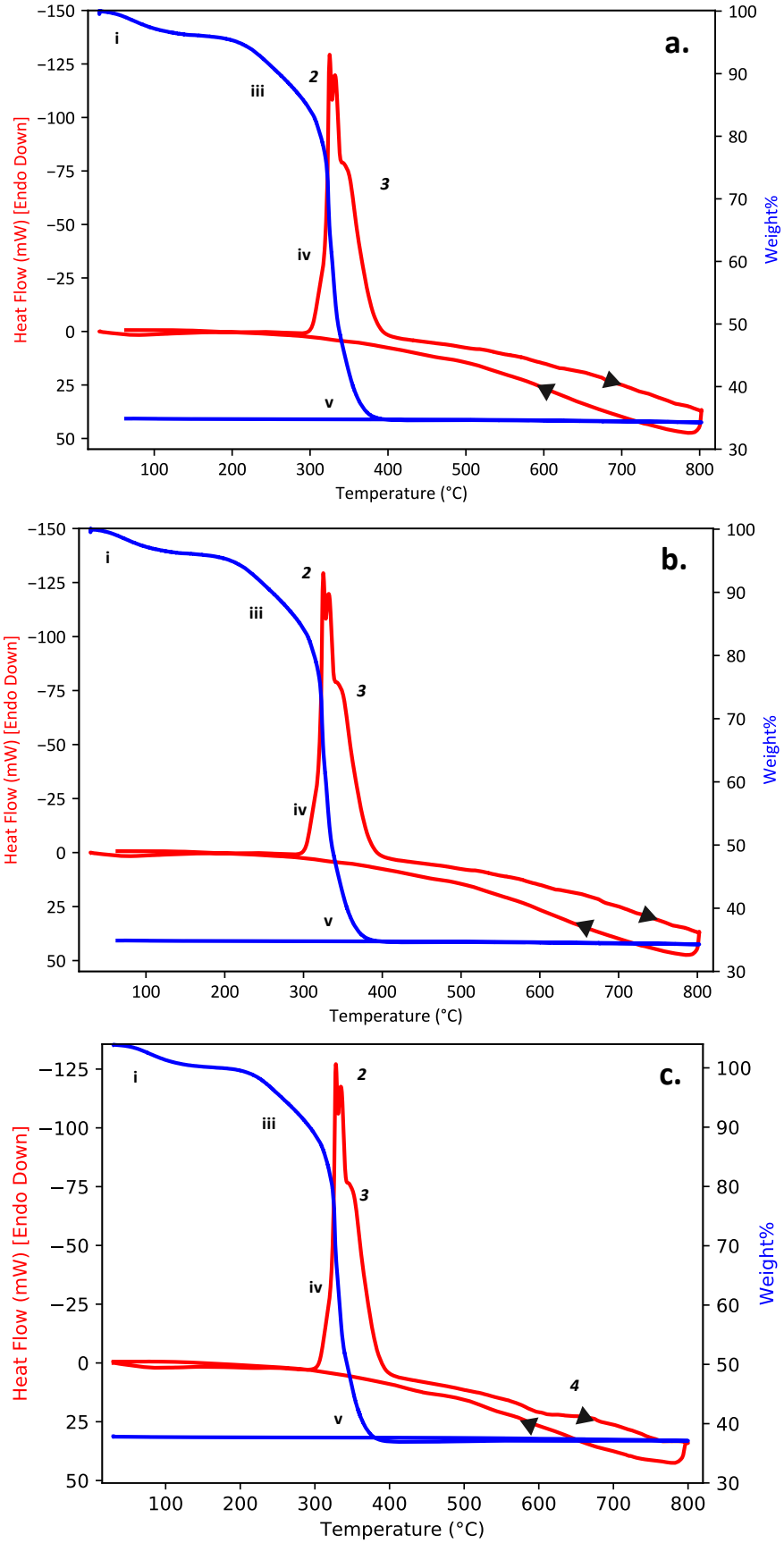

Figure 4.8: DTA and TGA plots of Al-doped lithium manganese oxide precursors synthesised with [M_T]:[Cit] of (a) 1:1.667 (b) 1:1 and (c) 1:0.667.

4.1.5. The effect of calcining nitrate precursors at 270 °C and 300 °C

Since the DTA curves (Fig.4.6, Fig.4.7 and Fig.4.8) showed mass loss processes *ii* and *iii* for the various precursors, these precursors were calcined for 5 hours at 270 °C and 300°C each to probe what occurs just before the organic and nitrate components decompose. Thus precursors prepared with [M_T]:[Cit] = 1:1 were firstly heated to 270 °C and XRD patterns were collected (Fig.4.9(a)). The undoped precursor that was initially crystalline (Fig.4.4(a)) became amorphous (Fig.4.9(a)). A similar behaviour was reported by Kriston *et al.*[12] and Snyders *et al.*[8] where it was noted that if the starting precursor for lithium manganese oxide had a crystalline phase, the material became amorphous upon further heating to 250 °C before the formation of the final metal oxide at 550 °C. Also observed here is that the doped material simply remained amorphous when heated at 270 °C.

When heating these precursors from room temperature to 300 °C, it was observed that the formation of a spinel metal oxide starts emerging (Fig.4.9(b)) for both the undoped and Al-doped precursor as indicated by the tick marks added for the spinel structure.

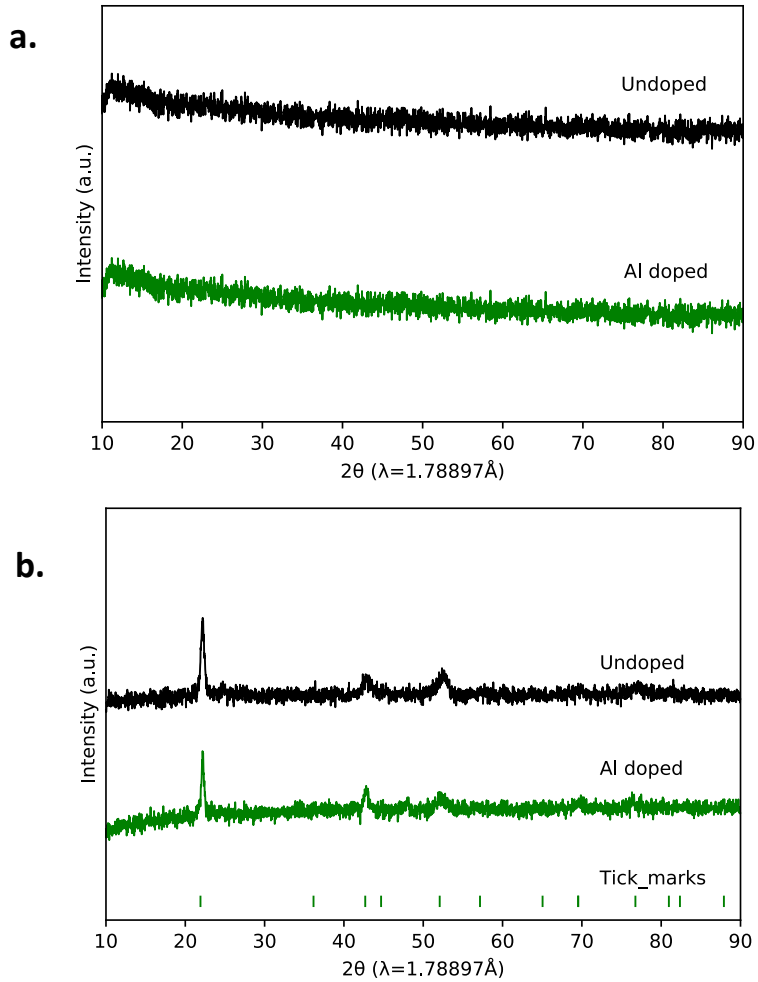

Figure 4.9: X-ray diffraction patterns of nitrate-based precursors prepared using [M_T]:[Cit] = 1:1 calcined at (a) 270 °C and (b) 300 °C for 5 hours in air with | being the tick marks for lithium manganese oxide spinel structure.

4.2. Investigation of precursors prepared using acetate salts

4.2.1. Laboratory XRD of precursors

The metal acetate salts were also used as starting materials to synthesise precursors of undoped and Al-doped lithium manganese oxide using the sol-gel method as described in chapter 3 and above with $[M_T]$:[Cit] = 1:1. Since metal acetates are more widely used in this synthesis [5, 13, 14], this work was done to compare the precursors and reactions to those synthesised using metal nitrate salts as starting materials.

Both undoped and Al-doped precursors (obtained from drying the gels at 140 °C for 5 hours in air) exhibit the crystallographic structure of a single phase consisting of Δ-aqua-S-citrato(2-)-manganese(II) with a space group of *P*222 (Fig.4.10) with the lattice parameters at (a)=6.03 Å, (b)= 10.47 Å and (c)= 13.56 Å and the cell volume of 858.4 $Å^3$ [3], these single phase Δ-aqua-S-citrato(2-)-manganese(II) was also obtained for the undoped nitrate-based precursors (Fig.4.4(a)). The Al-doped precursor synthesised using the metal nitrate salts was amorphous (Fig.4.5), but that was not the case here. From visual inspection, it was noticed that acetate-based precursors had relatively lower crystallinity compared to that for the undoped nitrate-based precursor. This resulted in poorer fits when Rietveld analysis of the diffraction patterns of both the acetate-based precursors was done, with GOF values of 4.55 and 3.61 obtained for undoped and Al-doped precursors, respectively (Table.4.4). The lattice parameters and crystallite size are comparable with precursors prepared using the nitrate salts as starting materials.

Table 4.4: Refined structural parameters of acetate-based precursor materials with $[M_T]$:[Cit] = 1:1 fitted using the Δ-aqua-S-citrato(2-)-manganese(II) system with space group *P*222.

	Lattice parameter			Rexp	Rwp	GOF	Crystallite size (μm)	Volume ($Å^3$)
	a(Å)	**b(Å)**	**c(Å)**					
undoped	6.0338(8)	10.4613(1)	13.5717(2)	0.87	3.94	4.55	6.37(2)	856.66(3)
Al-doped	6.0331(7)	10.4620(1)	13.5744(1)	0.90	3.25	3.61	6.36(1)	856.79(4)

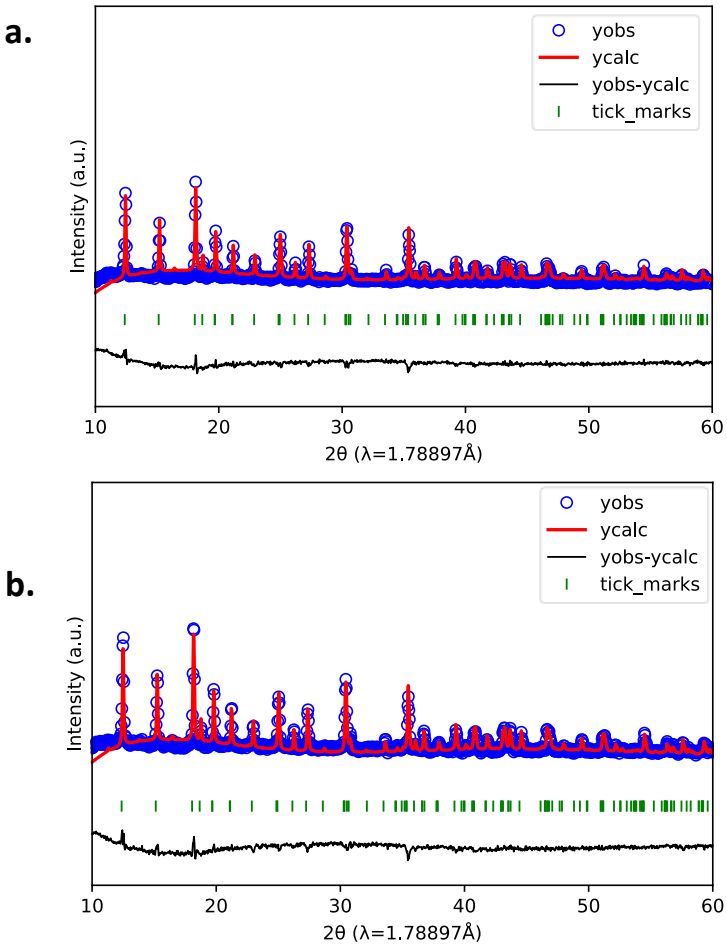

Figure 4.10: Rietveld refinement of a dried acetate-based precursors with [M_T]:[Cit] = 1:1 for (a.) undoped and (b.) Al-doped precursors. The tick marks correspond to orthorhombic phase for Δ-aqua-S-citrato(2-)-manganese(II).

4.2.2. STA analysis of precursors

The TGA and DTA plots for both these precursors show material decomposition occurring in four main steps (Fig.4.11, labelled *1 – 4* and *i – iv*, respectively), with no loss of moisture noted below 100 °C. The sample mass becomes stable from ~480 °C, revealing that the acetate-based precursors require higher temperature to decompose all the organic components as compared to nitrate-based precursors. The DTA data show one large exothermic peak (indicated by *3*) and a low intensity tail to the peak at higher temperatures (indicated by *4*). These are related to burning off of CO_2 as a results from decomposition of citric acid and acetates in the material. The DTA curves also show two endothermic processes (labelled *1* and *2*) taking place below 300 °C which are related to the processes *i* and *ii* on the TGA plots, respectively. These processes (endothermic peaks *1* and *2*) are related to adsorbed water and the water of crystallization as it was observed by Jeevanantham *et al.*[15] when synthesising $LiNi_{0.94}Mg_{0.01}Mn_{0.03}Co_{0.02}O_2$.

When heating both Al- and undoped materials from ~480 °C and higher, where the sample mass becomes stable, the Al-doped material resulted to higher product yield of ~30% with

the undoped material resulting in ~25%. Wang *et al*.[16] shows that partial substitution of Al in ($LiAl_{0.1}Mn_{1.9}O_4$) resulted in a higher percentage yield.

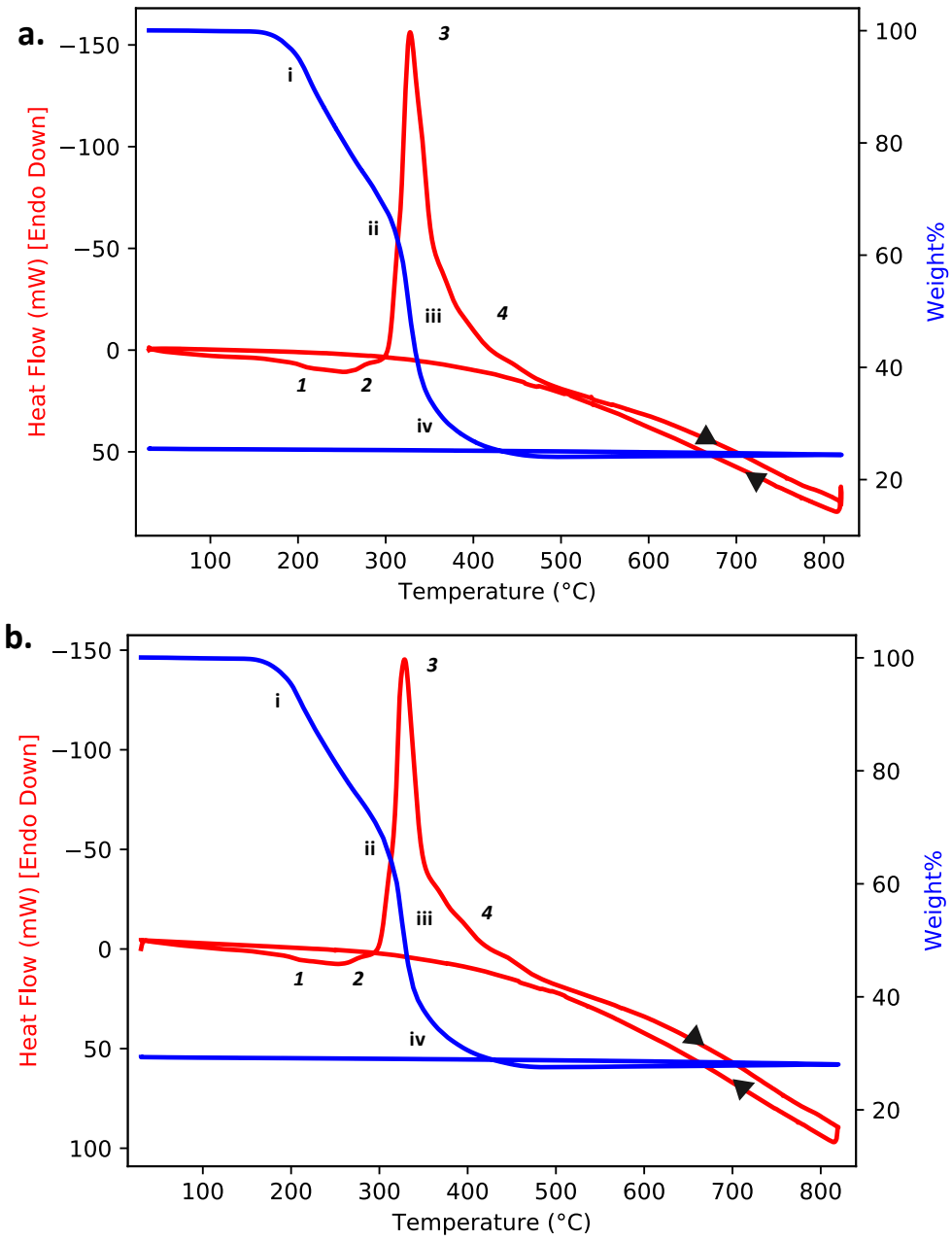

Figure 4.11: DTA and TGA plots for acetate-based precursors synthesised using [M_T]: [Cit] = 1:1 as for (a) undoped and (b) Al-doped precursors.

4.2.3. The effect of calcining acetate precursors at 270 °C and 300 °C

When heating both the undoped and Al-doped acetate-based precursors at 270 °C for 5 hours as before, they do not lose their crystallinity (Fig.4.12(a)) as was seen with the nitrate-based precursors, and the orthorhombic Δ-aqua-S-citrato(2-)-manganese(II) phase was still prevalent. However, when heating further at 300 °C only a broad hump was observed

implying an amorphous material had formed (Fig.4.12(b)). The acetate-based precursors clearly require high temperatures to enable phase transitions when compared to that for nitrate-based precursors.

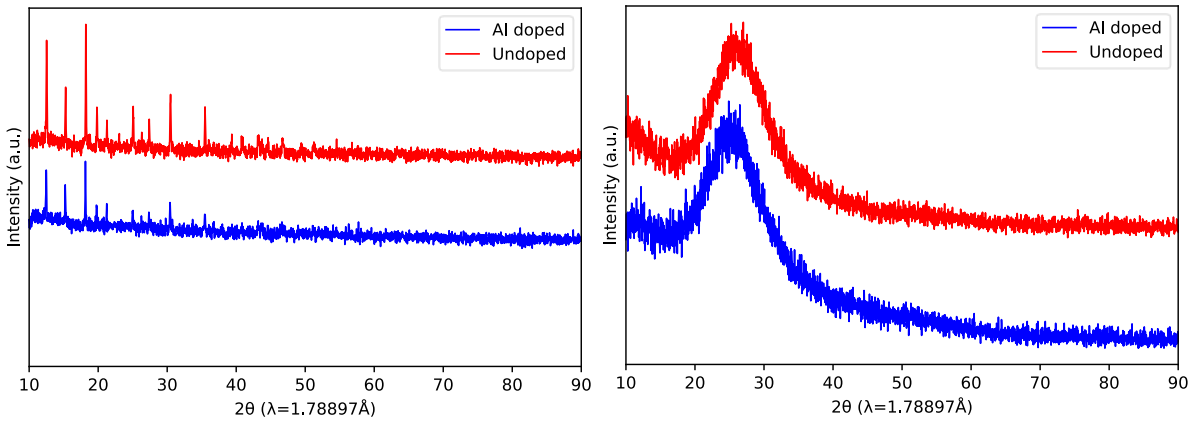

Figure 4.12: X-ray diffraction patterns of acetate-based precursors prepared using [M_T]: [Cit] = 1:1 and calcined at (a) 270 °C and (b) 300 °C for 5 hours in air.

4.3. Conclusion

Various undoped precursor materials prepared using metal nitrate salts exhibited a crystalline phase of Δ-aqua-S-citrato(2-)-manganese (II) with an orthorhombic crystal system and a *P*222 space group. A phase transition occurs to form an amorphous phase and upon further heating the nitrates and organics are burned off. When reducing the concentration of the citrate complexing agent, such that [M_T]:[Cit] = 1:0.5, the precursor forms a mixture of phases as observed from the Rietveld refinement, but it appears to be comprised of a single phase when [M_T]:[Cit] = 1: 0.667. The DTA curves of these materials show a reaction taking place when heated at (~600 °C). Based on the STA data of precursors prepared with excess citric acid (i.e. [M_T]:[Cit] = 1:1.667), more organic components are released (as CO_2) thereby loosing 80% of the initial mass. When reducing the concentration of citric acid, such that [M_T]:[Cit] = to 1:1, a mass loss of ~70% was less than that for the acetate-based precursor where a mass loss of closer to 75% was found. The acetate-based precursors need to be heated at higher temperatures (~600 °C) to produce the final metal oxide product since these materials does not easily decomposes at low to moderate temperatures (less than 600 °C), whereas the nitrate-based precursors required more moderate temperatures (~380 °C)

When doping with aluminium, precursors prepared using metal nitrate salts were amorphous, as observed from the XRD patterns. This was different to precursors prepared using metal acetate salts where the Δ-aqua-S-citrato(2-)-manganese (II) structure was found. When heating the acetate-based precursors with [M_T]:[Cit] of 1: 1 at 300 °C, an amorphous phase was formed, whereas heating the nitrate-based precursors under the same conditions resulted in the start of the formation of the spinel. The nitrate-based precursor thus decomposes at more moderate temperature, whether Al-doped or undoped, as compared to the citrate-based precursors.

4.5. References

[1] B. J. Kwon, F. Dogan, J. R. Jokisaari, B. Key, C. Kim, Y.-S. Liu, J. Guo, R. F. Klie and J. Cabana, "Effect of passivating shells on the chemistry and electrode properties of $LiMn_2O_4$ nanocrystal heterostructures," *Applied Materials & Interfaces,* vol. 1, pp. 1-36, 2018.

[2] V. Berbenni and A. Marini, "Thermogravimetry and X-ray diffraction study of the thermal decomposition processes in Li_2CO_3–$MnCO_3$ mixtures," *Journal of Analytical and Applied Pyrolysis,* vol. 62, pp. 45-62, 2002.

[3] Y. F. Deng, Z. H. Zhou and H. L. Wan, "D-Aqua-S-citrato(2±)manganese(II)," *Acta Crystallographica Section E,* vol. 59, pp. 310-312, 2003.

[4] "Crystallographic communications," June 2003. [Online]. Available: https://publcif.iucr.org/cifmoldb/gui/cifjmol.php?cifid=tk6102. [Accessed 31 January 2024].

[5] A. Hashem, S. Abbas, X. Hou, A. Eid and A. Abdel-Grany, "Facile one step synthesis method of spinel $LiMn_2O_4$ cathode material for lithium batteries," *Heliyon,* vol. 5, no. 7, pp. 1-29, 2019.

[6] B. Malecka, A. Lacz, E. Drozdz and A. Malecki, "Thermal decomposition of d-metal nitrates supported on alumina," *Journal of Thermal Analysis and Calorimetry,* vol. 119, pp. 1053-1061, 2015.

[7] H. S. Mohamed, H. Heba, E.-S. M. Mayyada, Amany Mostafa and H. F. Shaalan, "Synthesis, characterization and performance evaluation of lithium manganese oxide spinels for lithium adsorption," *Egyptian Journal of Chemistry,* vol. 60, no. 4, pp. 697-710, 2017.

[8] C. D. Snyders, E. E. Ferg and D. Billing, "An investigation into the phase transitions of synthesised materials with Al- and Mg-doped lithium manganese oxide spinels by in-situ powder x-ray diffraction," *Journals of Powder Diffraction,* vol. 32, no. 1, pp. 23-30, 2016.

[9] Y. Huang, Y.-C. Lin, D. M. Jenkins, N. A. Chernova, Y. Chung, B. Radhakrishnan, I.-H. Chu, j. Fang, Q. Wang, F. Omenya, S. P. Ong and M. S. Whittingham, "Thermal stability and reactivity of cathode materials for li-ion batteries," *Applied materials and Interfaces,* vol. 8, pp. 7013-7021, 2016.

[10] G. Maino, J. D'Haen, F. Mattelaer, C. Detavernier, A. Hardy and M. K. Van Bael, "Effect of annealing atmosphere on $LiMn_2O_4$ for thin film Li-ion batteries from aqueous chemical solution deposition," *Journals of Materials Chemistry A,* vol. 4, pp. 18457-18469, 2016.

[11] P. P. Prosini, A. Aurora, L. D. Seta and C. Paoletti, "Easy and scalable synthesis of $Li_{1.2}Ni_{0.2}Mn_{0.6}O_2$," *Energies,* vol. 16, no. 22, pp. 7674-7684, 2023.

[12] A. Kriston, I. Adanouj, V. Ruiz and A. Pfrang , "Quantification and simulation of thermal decomposition reactions of Li-ion battery materials by simultaneous thermal analysis coupled with gas analysis," *Journal of Power Sources,* vol. 435, p. 226774, 2019.

[13] Y. M. Hon, K. Z. Fung and M. H. Hon, “Synthesis and characterization of $Li_{1+x}Mn_{2-x}O_4$ powders prepared by citric acid gel process,” *Journal of the European Ceramic Society,* vol. 21, no. 4, pp. 515-255, 2001.

[14] P. Singh, A. Sil, M. Nath and S. Ray, “Preparation and characterization of lithium manganese oxide spinel $Li_{1.03}Mn_{1.97}O_4$ doped with Mg and Fe,” *Physica B,* vol. 34, pp. 622-628, 2010.

[15] B. Jeevanantham, P. Sarathkumar, S. Kavita and M. K. Shobana, “Magnesium doped $LiNi_xMn_yCo_zO_2$ cathode structural properties,” *Applied Surface Science Advances,* vol. 12, pp. 100350-100362, 2022.

[16] J. L. Wang, Z. H. Li, J. Yang, J. J. Tang, J. J. Yu, W. B. Nie, G. T. Lei and Q. Z. Xiao, “Effect of Al-doping on the electrochemical properties of a three-dimensionally porous lithium manganese oxide for lithium-ion batteries,” *Journal of Electrochemica Acta,* vol. 75, pp. 115-122, 2012.

Chapter 5: Understanding the effect of calcining precursors at various temperatures

Abstract: $Li_{1.03}Mn_{1.97}O_4$ and $LiAl_{0.4}Mn_{1.6}O_4$ can be prepared at moderate temperatures (~380 – 500°C) to form the final sought-after spinel structured metal oxide. Increasing the calcination temperature has revealed a decrease in lattice parameters and unit cell volume, with an increase in crystallite size. When heating precursors synthesized from nitrate salts to 800 °C, an additional impurity monoclinic phase for dilithium manganese oxide was detected together with the $Li_{1.03}Mn_{1.97}O_4$ cubic spinel phase, as observed from the Rietveld analysis. However, when heating precursors synthesized from acetate salts at the same conditions, the pure cubic spinel structure was found with no formation of impurities.

5.1. Laboratory X-ray diffraction analysis of precursors calcined at moderate temperatures (up to 500 °C)

5.1.1. Undoped lithium manganese oxide prepared using metal nitrate salts

Undoped lithium manganese oxide precursor materials prepared with $[M_T]$:[Cit] of 1:1.667 and 1:1 were looked at in more detail based on the observed DTA and TGA results (see Chapter 4). It was noted that when calcining these precursors at a temperature just above 380 °C, it appears to result in a final product being formed with no further reactions taking place. To probe this, the precursor materials were calcined at different temperatures from 380 °C to 500 °C and the products formed at each temperature were analysed to determine if there are any phase transformations occurring in that temperature range. This was an *ex-situ* approach, so the samples were cooled after leaving them at the given temperature for 5 hours and all diffraction patterns were measured at room temperature (Fig.5.1). In each case, the precursor material was simply heated to the desired temperature, i.e. this was not a consecutive methodology.

The diffraction patterns of calcined precursor materials with $[M_T]$:[Cit] = 1:1.667 all showed the formation of a crystalline cubic spinel structure (Fig.5.1) which increased in crystallinity as the calcination temperature was increased from 380 °C to 500 °C, as evidenced from the sharper peaks. The increase in crystallinity with increase in temperature was also achieved on a related material ($LiNi_{0.76}Mn_{0.14}Co_{0.1}O_2$) when analysing the effects of calcination temperatures between 725-900 °C by Zhenga *et al*. [1]. The XRD patterns had no additional peaks, an indication of the phase purity of the spinel metal oxide obtained at the various temperatures, at least within the resolution of the diffractometer used. A very slight peak shift to the right was observed as the calcination temperature was increased from 380 °C to 500 °C, also reported by Maino *et al*. [2] and Schluter *et al.* [3], which results from a decrease in lattice dimensions.

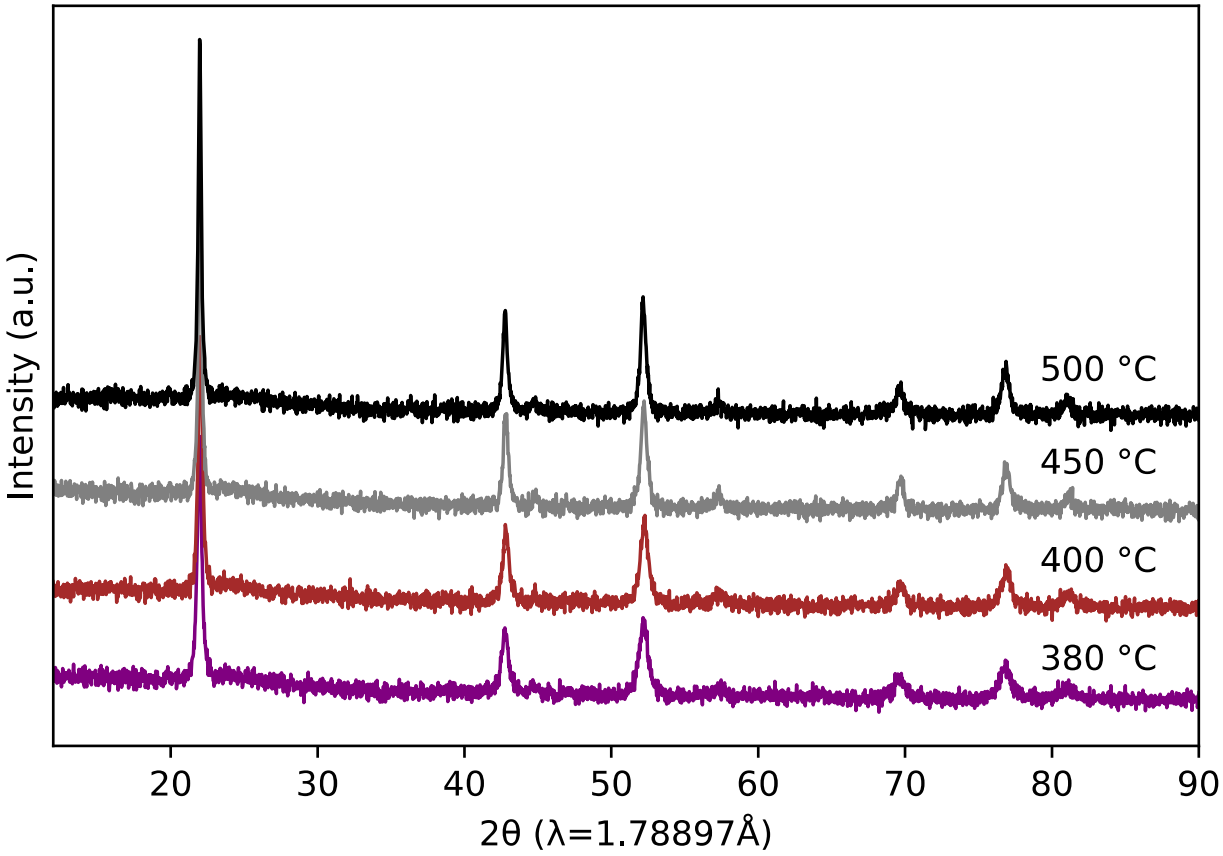

Figure 5.1: PXRD diffractograms of $Li_{1.03}Mn_{1.97}O_4$ prepared with 1: 1.667 [M_T]: [Cit] by calcining the precursor at different temperatures for 5 hours in the air.

A similar response was observed when calcining precursors with [M_T]:[Cit] = 1:1, with the final spinel product already forming at 380 °C and the same behaviour noted as the calcination temperature was increased (Fig.5.2). Further comprehensive analysis of the XRD patterns was performed via Rietveld refinements to quantify the structural changes with varying calcination temperature [4].

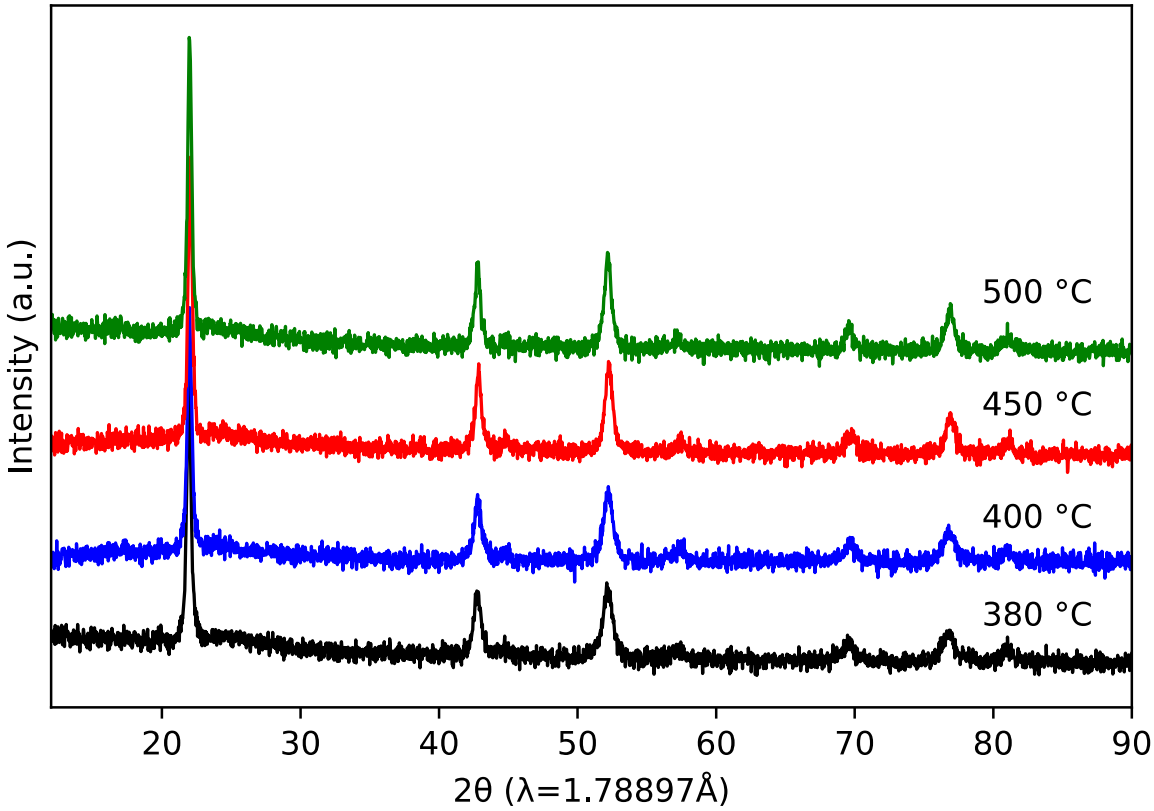

Figure 5.2: PXRD diffractograms of $Li_{1.03}Mn_{1.97}O_4$ prepared with 1: 1 [M_T]: [Cit] calcined at different temperatures for 5 hours in the air.

The Rietveld refinements of the laboratory X-ray diffractograms confirmed that metal oxides prepared with [M_T]:[Cit] = 1:1 displayed the cubic spinel phase of $Li_{1.03}Mn_{1.97}O_4$ (space group *Fd*-3*m*) when the precursor material was calcined at 380 °C, 400 °C, 450 °C, or 500 °C for 5 hours in air (Fig.5.3) and all the diffraction peaks are indexed accordingly. It was interesting to note that even the material calcined at the lower temperatures demonstrate excellent crystallinity and well-defined cubic spinel structure [5, 6].

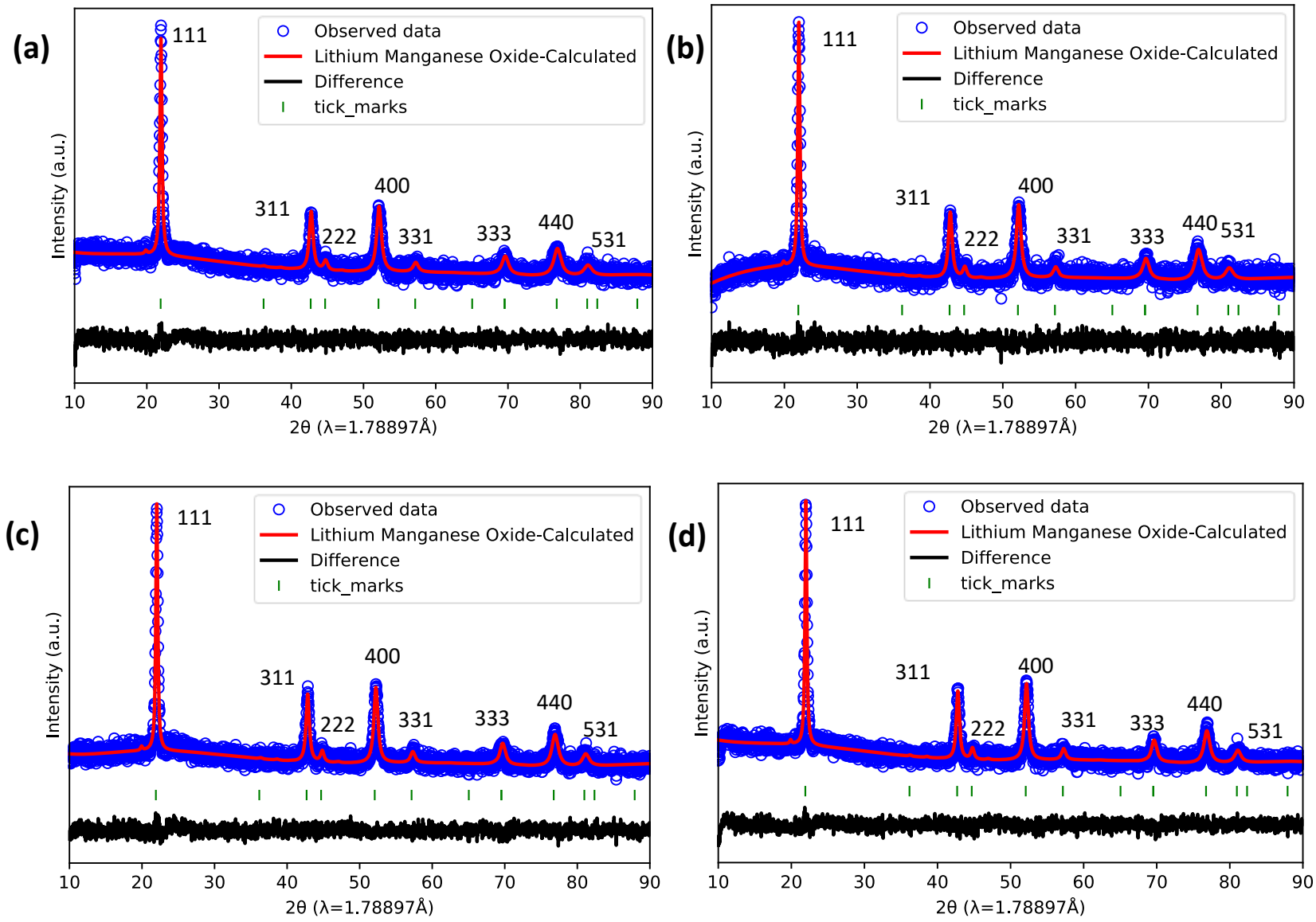

Figure 5.3: Rietveld refinement fitting the $Li_{1.03}Mn_{1.97}O_4$ cubic spinel crystal structure (space group *Fd*-3*m*) to the XRD patterns for samples with $[M_T]$:[Cit] = 1:1 calcined at (a) 380 °C, (b) 400 °C, (c) 450 °C and (d) 500 °C in air.

The lattice dimensions extracted from the refinement (Table 5.1) show a slight decrease in the with increasing the calcination temperature, resulting in the unit cell volume shrinking. When increasing the calcination temperature between 380 – 500 °C, the cathode materials favours the formation of a well-ordered spinel structure. It was observed that with increasing calcination temperature, the curves shift towards slightly higher 2θ values, along with increasing crystallite size (Table.5.1), which aligns with the data from Lee *et al*. [7] and Ronduda *et al.* [8].Thus in general an increase in calcination temperature results in an increase in average crystallinity and particle size [9].

Table 5.1: Refined room temperature structural parameters of $Li_{1.03}Mn_{1.97}O_4$ using the cubic spinel model (space group *Fd*-3*m*). Samples were produce using $[M_T]$:[Cit] = 1:1 and calcining the precursors at various temperatures.

Calcination temperature (°C)	Lattice parameter (Å)	Rexp	Rwp	GOF	Crystallite size (μm)	Volume (Å^3)
380	8.1498(1)	1.06	1.11	1.06	3.36(4)	541.30(3)
400	8.1491(2)	1.05	1.10	1.04	4.27(6)	541.16(2)
450	8.1473(1)	1.05	1.09	1.04	4.36(5)	540.81(2)
500	8.1418(3)	1.04	1.12	1.07	5.66(5)	539.71(2)

When the material prepared with $[M_T]$:[Cit] = 1:1 was calcined at 380 °C for an extended period (10 hours), the Rietveld refinement revealed no phase changes had occurred when compared to the material calcined for 5 hours at the same temperatures (Fig.5.4). However, when heating the material for this longer period, the lattice parameter decreases slightly to 8.1456(2) Å, with a corresponding decrease in the unit cell volume (540.47(3) Å^3), and the crystallite size (6.46(3) μm) increases. Which shows that longer annealing times results in crystallite growth and better ordering of atoms (smaller average unit cells) and gives comparable sizes to that when annealing at higher temperatures for 5 hours (~600 °C and will be seen in Table 5.5).

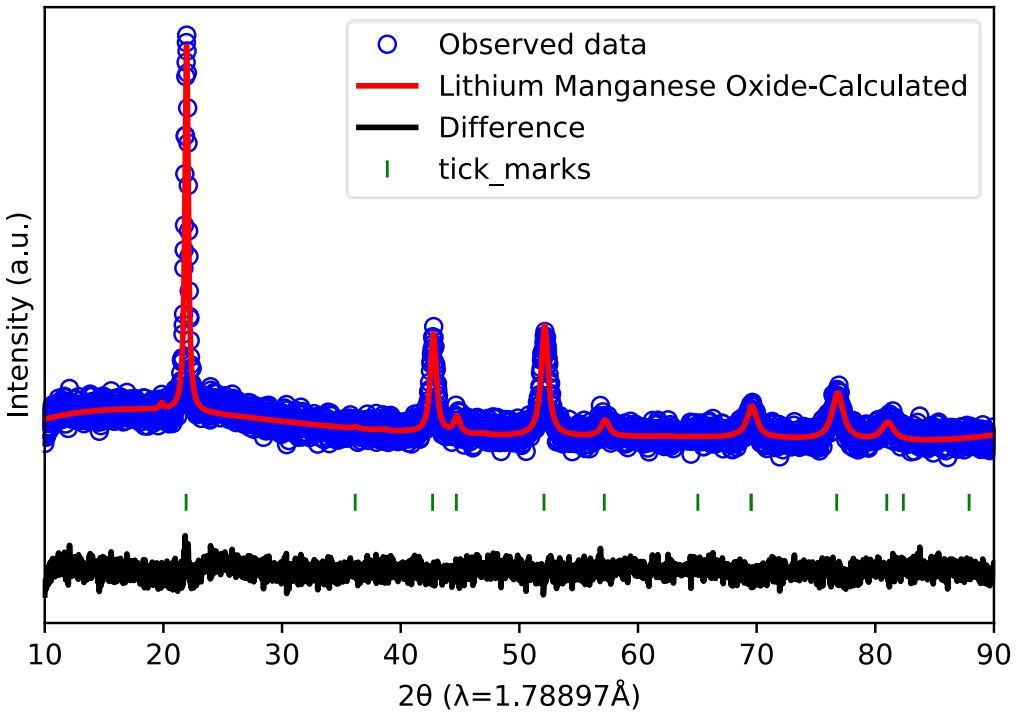

Figure 5.4: The Rietveld refinement of $Li_{1.03}Mn_{1.97}O_4$ (calcined at 380 °C for 10 hours) with space group *Fd*-3*m* synthesised using $[M_T]$:[Cit] = 1:1; Rwp= 1.13, Rexp=1.04 and GOF= 1.09.

The Rietveld refinements of $Li_{1.03}Mn_{1.97}O_4$ synthesised with $[M_T]$:[Cit] = 1:1.667 showed comparable responses to that prepared with $[M_T]$:[Cit] = 1:1, where only the cubic spinel crystal structure was observed after calcining in the same temperature range (Fig.5.5) and the refined parameters are presented in Table 5.2. As before, when increasing the calcining temperature, a slight decrease in the unit cell volume was observed and an increase in crystallite size.

Table 5.2: Refined room temperature structural parameters of calcined $Li_{1.03}Mn_{1.97}O_4$ (synthesised using $[M_T]$:[Cit] = 1:1.667) using the cubic spinel model (space group *Fd*-3*m*).

Calcination temperature (°C)	Lattice parameter (Å)	Rexp	Rwp	GOF	Crystallite size (µm)	Volume (Å^3)
380	8.1571(2)	1.04	1.09	1.05	2.76(5)	542.75(2)
400	8.1461(4)	1.05	1.10	1.04	3.23(3)	540.57(2)
450	8.1452(7)	1.04	1.13	1.08	4.27(4)	540.39(1)
500	8.1409(2)	1.04	1.12	1.07	4.36(3)	539.53(2)

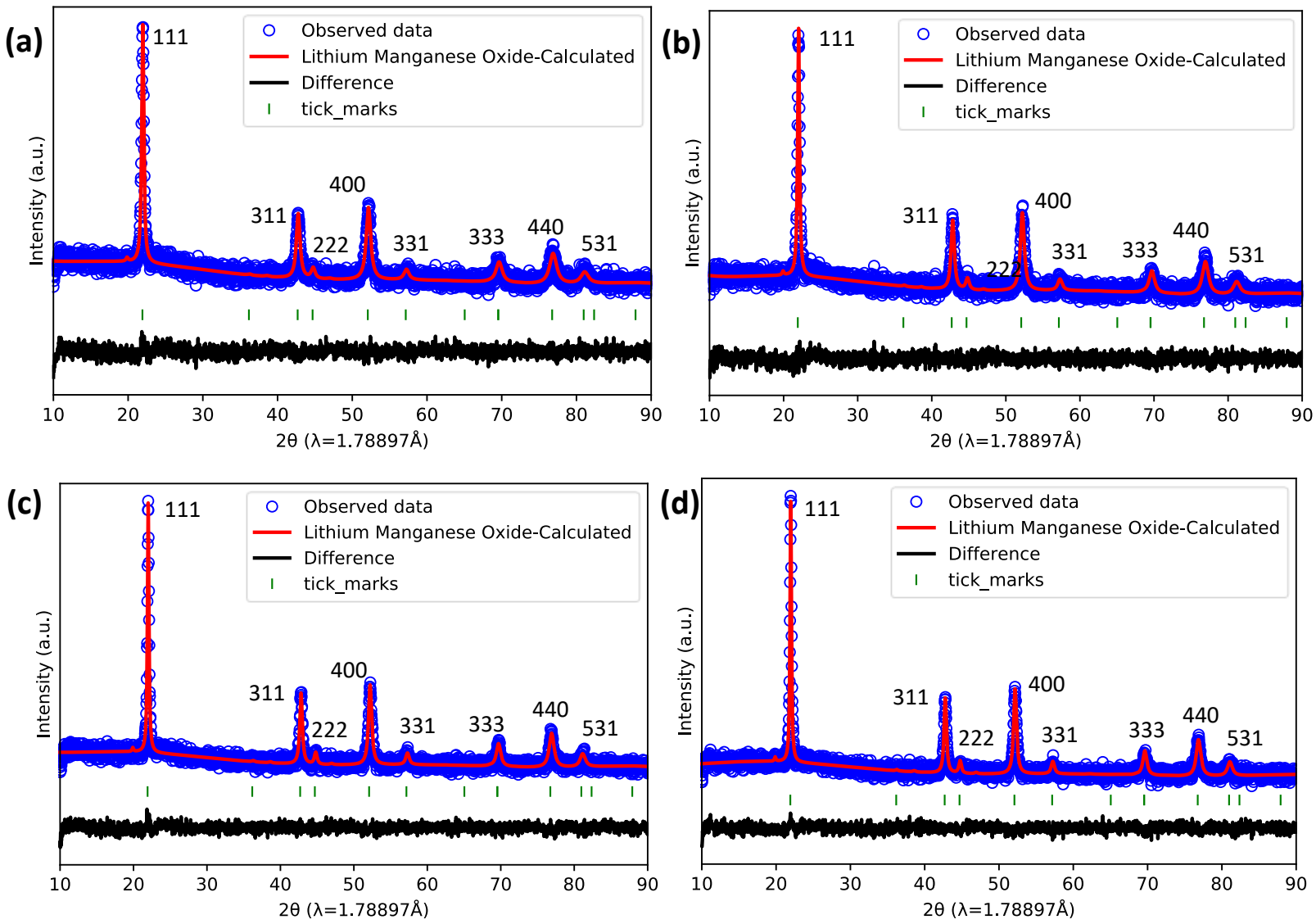

Figure 5.5: Rietveld refinement fitting the $Li_{1.03}Mn_{1.97}O_4$ cubic spinel crystal structure (space group *Fd*-3*m*) to the XRD pattern for samples with $[M_T]$:[Cit] = 1:1.667 calcined at (a) 380 °C, (b) 400 °C, (c) 450 °C and (d) 500 °C in air

In Chapter.4, it was evident from the ripples in the DTA curves at higher temperatures (indicated by *4* in Fig.4.7 (b and c)) that the materials prepared with an excess concentration of total metal nitrate salts compared to citric acid resulted in further reaction taking place beyond 380 °C, even though these were not accompanied by further mass loss. When calcining these samples to apply an *ex-situ* investigation, a side reaction occurred when the samples were heated to 380 °C in the furnace and kept there for 5 hours (Fig.5.6). This resulted in a black product being expelled into the furnace. This may be related to these ripples noted. At 380 °C it would have been expected that the carbonaceous material would be converted to CO_2 and H_2O already as shown in the TGA curves Fig.4.7 (b and c)).



Figure 5.6: The samples prepared using [M_T]:[Cit] of 1:0.833 and 1:0.667 heated to 380 °C and calcined for 5 hours in air.

5.1.2. Al-doped lithium manganese oxide prepared using metal nitrate salts

When calcining the Al-doped samples with different [M_T]:[Cit] (1:1.667, 1:1 and 1:0.667), it was observed that increasing the concentration of citric acid results in an increase in crystallinity of the material when calcined for the same duration at the same temperature (Fig.5.7). The increase in calcination temperature from 380 °C to 450 °C also shows a slight increase in XRD peak intensity while the diffraction peaks shift slightly to higher 2θ angles. The Al-doped precursor materials prepared with an excess of total metal ions compared to citric acid (1:0.667 [M_T]:[Cit]) formed a cubic spinel structure when calcined at 380 °C, indicating that doping with aluminium has resulted in material stability as compared to the undoped sample. Yuwen *et al.* [10] also showed that doping with aluminium enhance the structural stability of the material.

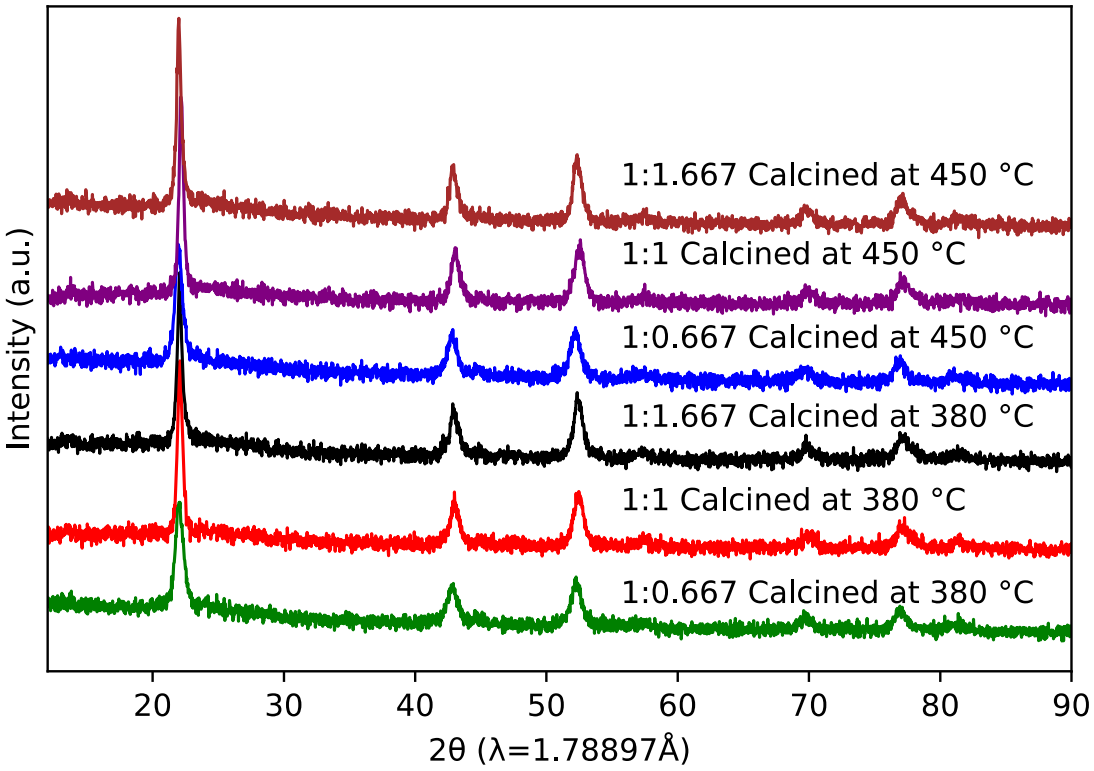

Figure 5.7: PXRD patterns of $LiAl_{0.4}Mn_{1.6}O_4$ prepared with $[M_T]$:[Cit] of 1:1.667, 1:1 and 1:0.667 calcined at different temperatures for 5 hours in the air.

The Rietveld refinement of the diffraction patterns of $LiAl_{0.4}Mn_{1.6}O_4$ prepared with different $[M_T]$:[Cit] (Table.5.3) was fitted using the cubic spinel (Fig.5.8 and Fig.5.9) which shows a good agreement between the observed and calculated model. When increasing the calcination from 380 °C and 450 °C, the Al-doped samples showed no apparent change on the crystal structure and all the diffraction peaks were indexed according to the cubic spinel structure (Fig.5.9). Material prepared with $[M_T]$:[Cit] = 1:1 showed higher crystallite sizes when compared to the other materials.

The Rietveld refinement of a calcined Al-doped material ($LiAl_{0.4}Mn_{1.6}O_4$) at 380 °C and 450 °C results in a decrease in lattice dimensions with an increase in temperature (Table 5.3), which was similar to what was observed with undoped samples when calcined at these temperatures. The crystallite size increases with an increase in calcination temperature.

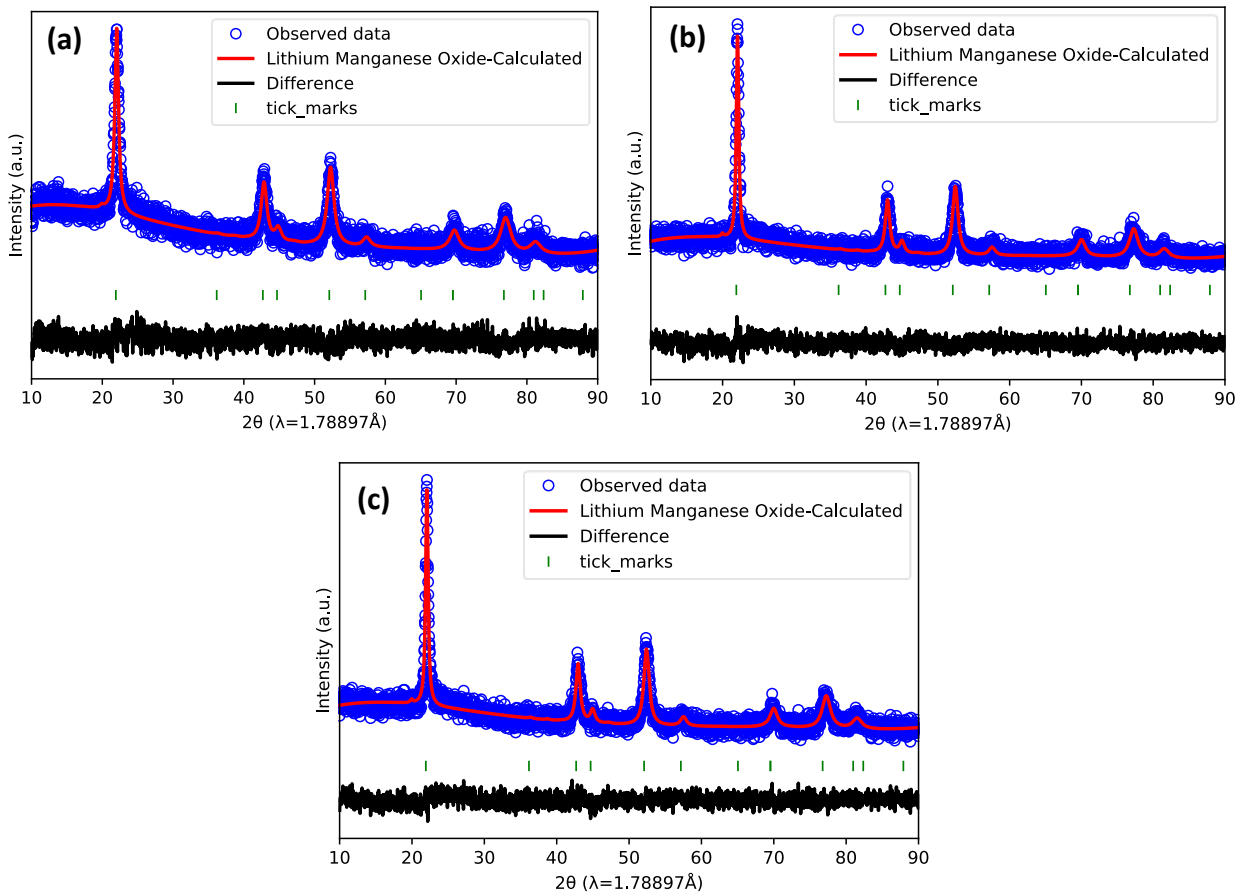

Figure 5.8: Rietveld refinements fitted with $LiAl_{0.4}Mn_{1.6}O_4$ cubic spinel crystal structure (space group *Fd*-3*m*) to the XRD pattern for $[M_T]$:[Cit] of (a) 1:0.667, (b) 1:1 and (c) 1:1.667 sample calcined at 380 °C in air.

Since the ionic radius of Al^{3+} ion (0.053 nm) is smaller than that of the Mn^{3+} ion (0.064 nm), the partial substitution of Mn^{3+} by Al^{3+} in the lithium manganese oxide lattice should result in shrinkage of the unit cell volume (i.e. reduced lattice dimensions) and a single phase should remain. The data from the Rietveld refinements confirm this (Table 5.3). It was noted by Marincaş *et al.* [11] that when doping with aluminium, there was a decrease in the cell parameters due to smaller ionic radius for Al^{3+} compared to that of Mn^{3+} and various studies support that doping with Al^{3+} promotes a stable crystal structure when heating the material to 850°C [12, 13, 14].

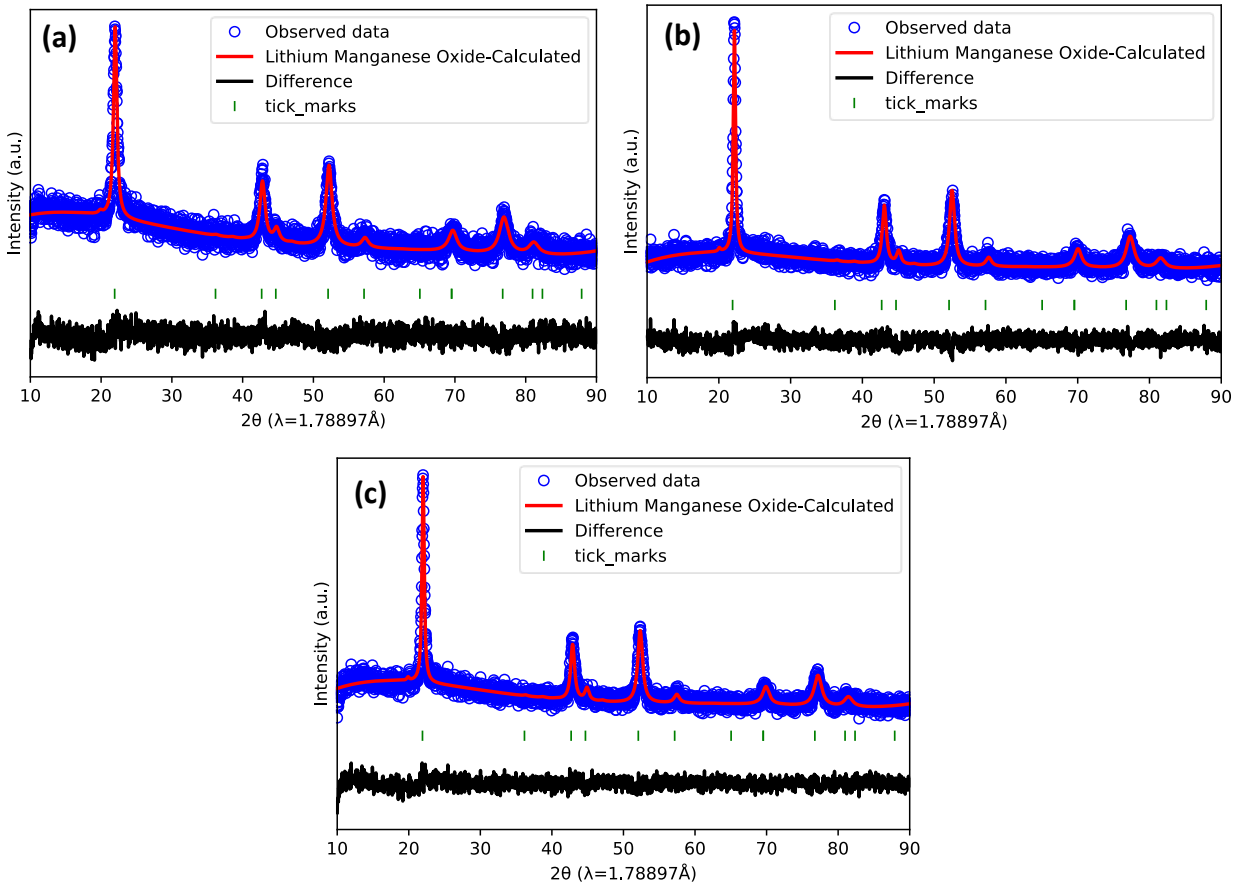

Figure 5.9: Rietveld refinements fitted with $LiAl_{0.4}Mn_{1.6}O_4$ cubic spinel crystal structure (space group *Fd*-3*m*) to the XRD pattern for $[M_T]$:[Cit] of (a) 1:0.667, (b) 1:1 and (c) 1:1.667 samples calcined at 450 °C in air.

Table 5.3: Refined room temperature structural parameters of $LiAl_{0.4}Mn_{1.6}O_4$ calcined at 380 and 450 °C fitted using the cubic spinel model (space group *Fd*-3*m*).

$[M_T]$:[Cit]	Calcination temperature (°C)	Lattice parameter (Å)	Rexp	Rwp	GOF	Crystallite size (µm)	Volume (Å^3)
1:0.667	380	8.1449(2)	1.10	1.14	1.03	2.61(2)	540.32(4)
1:0.667	450	8.1406(2)	1.10	1.19	1.08	3.04(3)	539.47(2)
1:1	380	8.1177(2)	1.09	1.08	1.09	4.34(5)	534.93(3)
1:1	450	8.1128(1)	1.09	1.22	1.10	5.26(2)	533.96(3)
1:1.667	380	8.1138(2)	1.09	1.21	1.11	2.13(8)	534.17(3)
1:1.667	450	8.1118(1)	1.10	1.15	1.05	3.57(2)	533.77(2)

When the dried starting material precursor with $[M_T]$:[Cit] = 1:1 was calcined at 380 °C for an extended period (10 hours) (Fig.5.10), only a slight decrease in the lattice parameter and volume (8.1119(6) Å and 533.78(3) $Å^3$, respectively) and an increase in the crystallite size (5.32(2) µm) was found. The difference was not as dramatic as that seen for the undoped material which again supports the higher stability when doping with Al^{3+}.

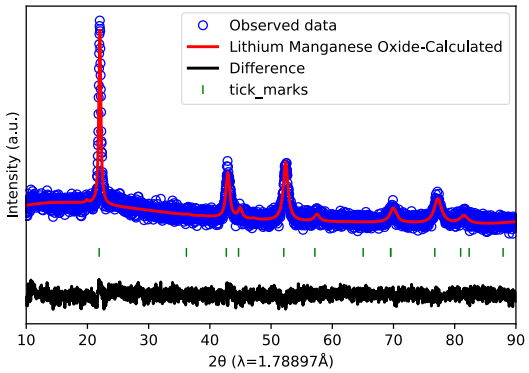

Figure 5.10: Rietveld refinement of $LiAl_{0.4}Mn_{1.6}O_4$ with space group *Fd*-3*m*; Rwp = 1.18, Rexp = 1.09 and GOF = 1.08. The precursor made with $[M_T]$:[Cit] = 1:1 was calcined at 380 °C for 10 hours.

5.1.3. Undoped and Al-doped lithium manganese oxide prepared using metal acetate salts

STA data indicated the formation of a final product with no further mass loss at temperatures just below 400 °C (Section 4.3) for precursors prepared using metal acetate salts – slightly higher than that prepared using the nitrate salts. These precursors were thus calcined at 400 °C and 500 °C and they were shown to exhibit an initial formation of the spinel structure, but the diffraction peaks had low intensities (especially when compared that that for the materials prepared using nitrate salts) , which increased with increase in temperature, thus indicating that the spinel phase was not yet fully formed or ordered when calcined at 400 °and 500 °C (Fig.5.11). Once again, no impurity phases were detected for both the undoped and Al-doped materials calcined at these temperatures for 5 hours in air (Table.5.4).

Table 5.4: Refined room temperature structural parameters of calcined metal oxides of $Li_{1.03}Mn_{1.97}O_4$. and $LiAl_{0.4}Mn_{1.6}O_4$ with space group *Fd*-3*m*.

	Calcination temperature (°C)	Lattice parameter (Å)	Rexp	Rwp	GOF	Crystallite size (µm)	Volume ($Å^3$)
$Li_{1.03}Mn_{1.97}O_4$	400	8.1497(8)	2.37	3.07	1.29	3.87(2)	547.31(2)
	500	8.1463(6)	2.22	4.14	1.86	4.36(3)	544.46(2)
$LiAl_{0.4}Mn_{1.6}O_4$	400	8.1387(3)	2.34	3.40	1.45	2.65(4)	546.92(3)
	500	8.1247(3)	2.35	3.32	1.41	3.49(2)	543.33(2)

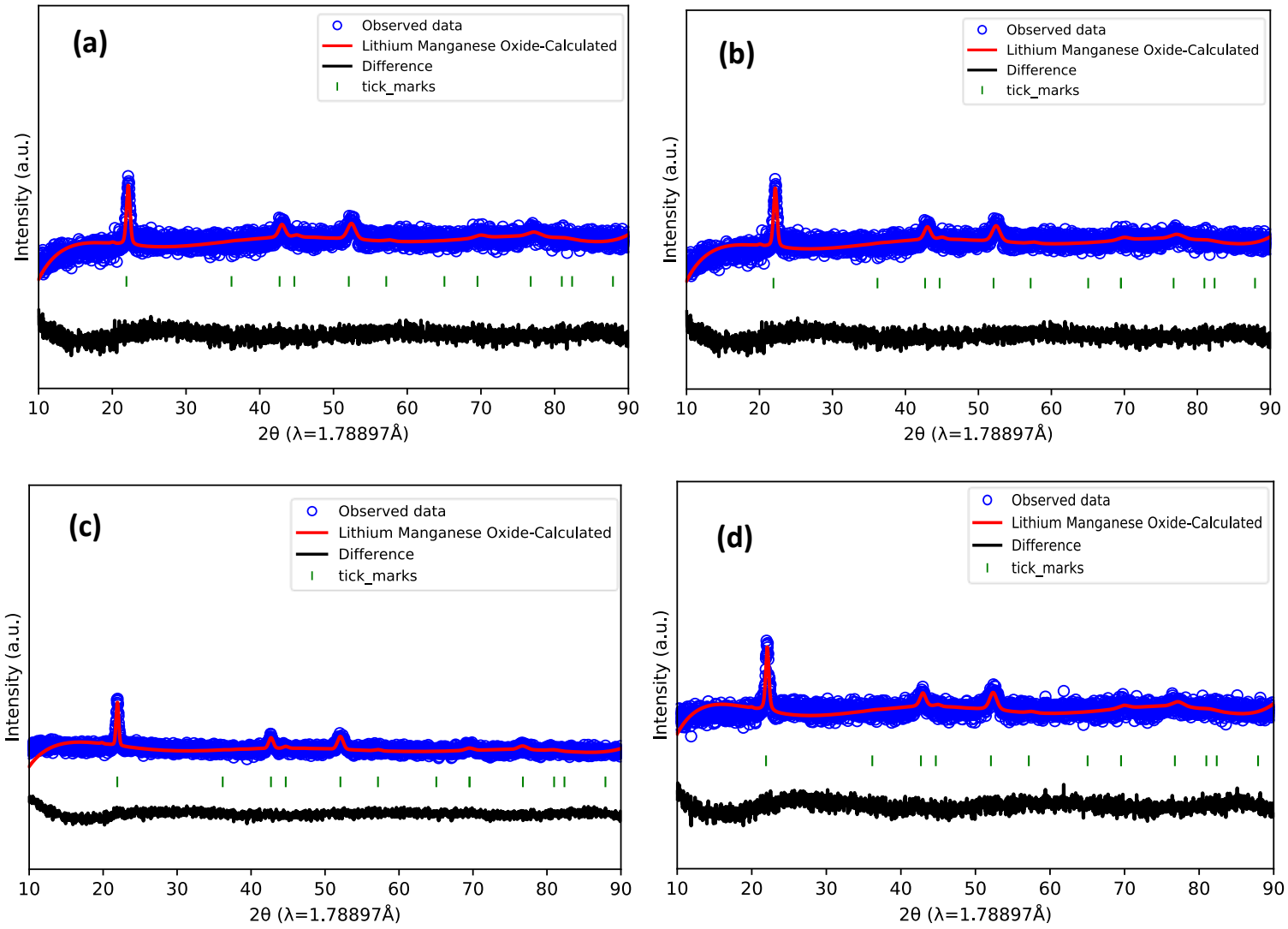

Figure 5.11: Rietveld refinement of $Li_{1.03}Mn_{1.97}O_4$ calcined at (a) 400 °C and (b) 500 °C, and of $LiAl_{0.4}Mn_{1.6}O_4$ calcined also at (c) 400 °C and (d) 500 °C for $[M_T]$:[Cit] = 1:1 using the cubic spinel crystal structure (space group *Fd*-3*m*).

5.2. Laboratory X-ray diffraction analysis of precursors calcined at high temperatures (600- 800 °C)

5.2.1. Undoped and Al-doped lithium manganese oxide prepared using metal nitrate salts

When calcining precursor material of $Li_{1.03}Mn_{1.97}O_4$ prepared using [M_T]:[Cit] = 1:1 with metal nitrate salts at high temperature has resulted in an increase in crystallinity. Rietveld refinements of the sample calcined at 600 °C and 700 °C (Fig.5.12. (a and b)) show a pure cubic spinel structure, however, when calcining this material at 800 °C, the formation of mixture of phases of a monoclinic crystal system (space group *C*2/*C*) for dilithium manganate(IV) (Li_2MnO_3) and the cubic spinel crystal system (space group *Fd*-3*m*) for lithium manganese oxide (Fig.5.12.c) was observed. The formation of a Li-rich phase at high temperatures has also been reported by Yu *et al.* [14] and Pulido *et al.* [15]. Increasing the calcination temperature results in narrower and sharper peaks with higher signal-to-noise ratios; this was observed on the difference plot where smooth lines show low noise from the background.

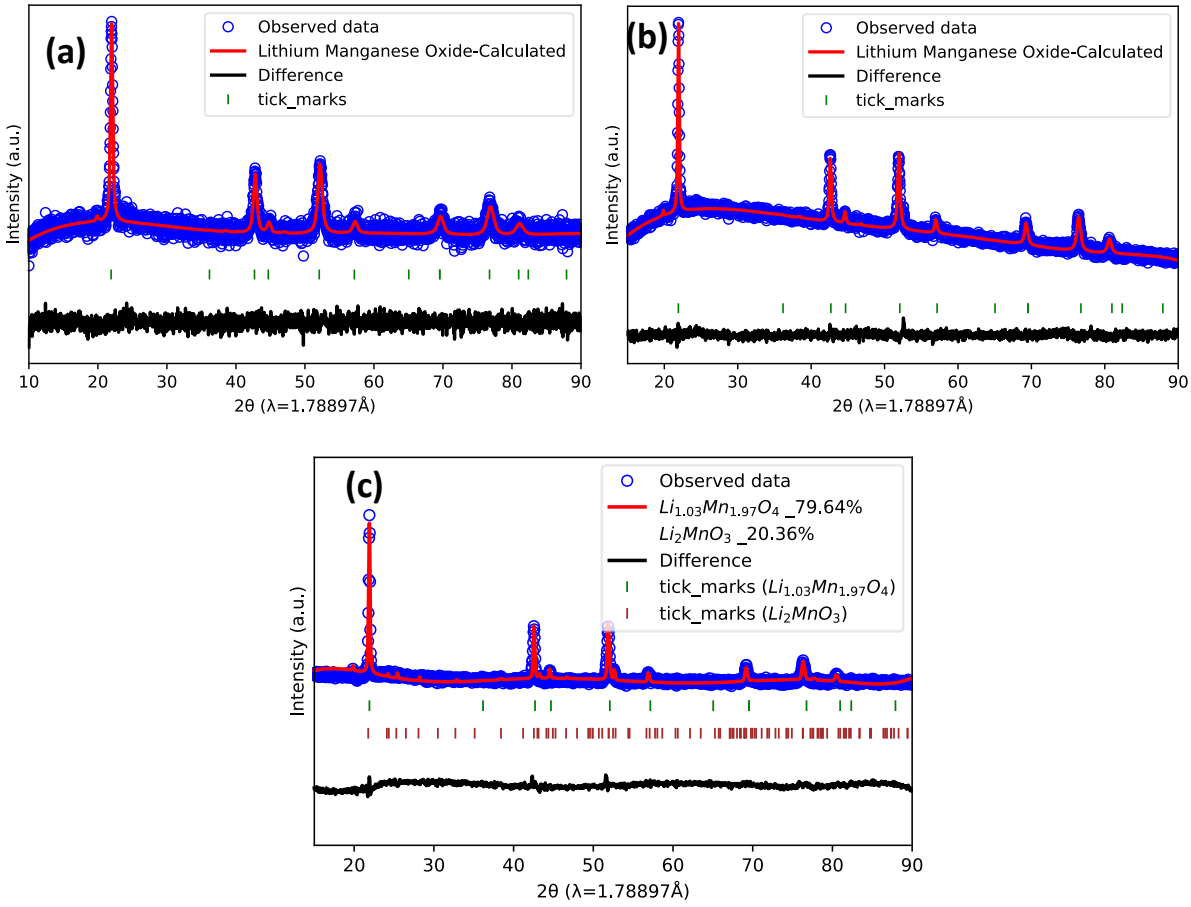

Figure 5.12: Rietveld refinement of $Li_{1.03}Mn_{1.97}O_4$ prepared with [M_T]:[Cit] = 1:1 and calcined at (a) 600 °C, (b) 700 °C and (c) 800 °C in air prepared with nitrate precursor.

When calcining Al-doped materials prepared with [M_T]:[Cit] = 1:1 at high temperatures, the materials formed had pure cubic spinel structures with increasing crystallinity as temperature is increased (Fig.5.13). In this case, the Li-rich phase was not formed at 800 °C, indicating the

stabilising effect of aluminium on the structure. A decrease in lattice parameter and volume was noticed while the crystallite size increase when increasing calcining temperatures (Table.5.5). However, the $Li_{1.03}Mn_{1.97}O_4$ prepared with $[M_T]$:[Cit] = 1:1 and annealed 800 °C has a higher lattice parameter (8.2054 (3) Å) when compared to the other samples which might be due to a mixture of phases. It was observed from the Rietveld refinement (Table.5.5) that samples calcined at temperature lower than 800 °C have a good R statistic and a GOF of approximately 1 which implies a good correlation between the calculated structure model and the measured pattern, a slight mismatch between the first peak of the sample calcined at 800 °C was observed which resulted in an increase in GOF and Rwp statistical value.

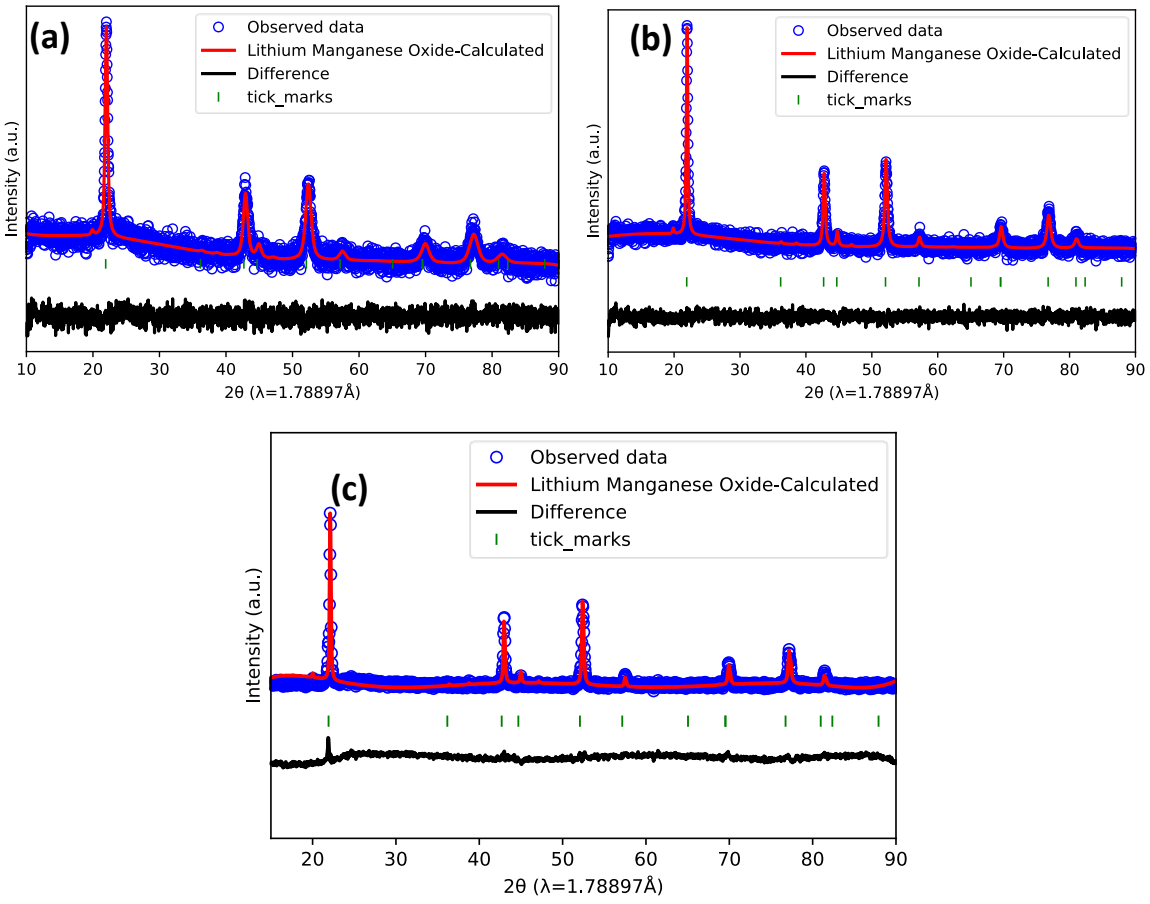

Figure 5.13: Rietveld refinement of $LiAl_{0.4}Mn_{1.6}O_4$ prepared with $[M_T]$:[Cit] = 1:1 and calcined at (a) 600 °C, (b) 700 °C and (c) 800 °C in air prepared with nitrate precursor.

Table 5.5: Refined room temperature structural parameters of calcined metal oxides of $Li_{1.03}Mn_{1.97}O_4$. and $LiAl_{0.4}Mn_{1.6}O_4$ with space group *Fd*-3*m* of a cubic model.

	Calcination temperature (*°C*)	Space group	Lattice parameter (Å)	Rexp	Rwp	GOF	Crystallite size (μm)	Volume (Å^3)
$Li_{1.03}Mn_{1.97}O_4$	600	*Fd*-3*m*	8.1447(4)	1.06	1.11	1.06	6.09(6)	540.29(9)
	700	*Fd*-3*m*	8.1349(1)	1.04	1.09	1.05	6.29(5)	538.34(3)
	800	*Fd*-3*m* *C2/C*	8.2054(2) a=4.9463(8) b=8.5621(2) c=9.5623(3) β= 99.12 (1)	0.83	3.29	3.98	6.45(3)	552.46(4)
$LiAl_{0.4}Mn_{1.6}O_4$	600	*Fd*-3*m*	8.1119(1)	1.04	1.08	1.04	5.47(3)	533.78(2)
	700	*Fd*-3*m*	8.1082(1)	1.09	1.14	1.04	6.48(2)	533.05(3)
	800	*Fd*-3*m*	8.1024(8)	0.82	3.29	3.98	6.65(2)	531.91(4)

5.2.2. Undoped and Al-doped lithium manganese oxide prepared using metal acetate salts

Samples of $Li_{1.03}Mn_{1.97}O_4$ that were prepared using the acetate salts and $[M_T]$:[Cit] = 1:1 were calcined at 600-800 °C for 5 hours. Rietveld refinement of the XRD data shows a pure cubic spinel phase without any formation of impurities (Fig.5.14(c)) for all samples, unlike that observed for the nitrate-based sample. It was noted by Dong *et al.* [16] that calcining at higher temperatures leads to increased particle size as material crystallinity increases which is similar to what was observed. Al-doped materials have shown reduced lattice parameters when calcined at high temperatures when compared to the undoped samples (Table.5.6). Zhenfei *et al.* [17] also indicated a smaller lattice parameter for the Al-doped $LiMn_2O_4$ cathode material (8.2507 Å) and cell volume of (567.617 Å^3) as compared to the undoped sample (8.8621 Å and 695.99 Å^3, respectively). The increase in GOF on the sample calcined at 800 °C was observed (Table.5.6) which is similar to that of Table.5.5 and are both related to the minor mismatch between the calculated structure pattern and the measured pattern.

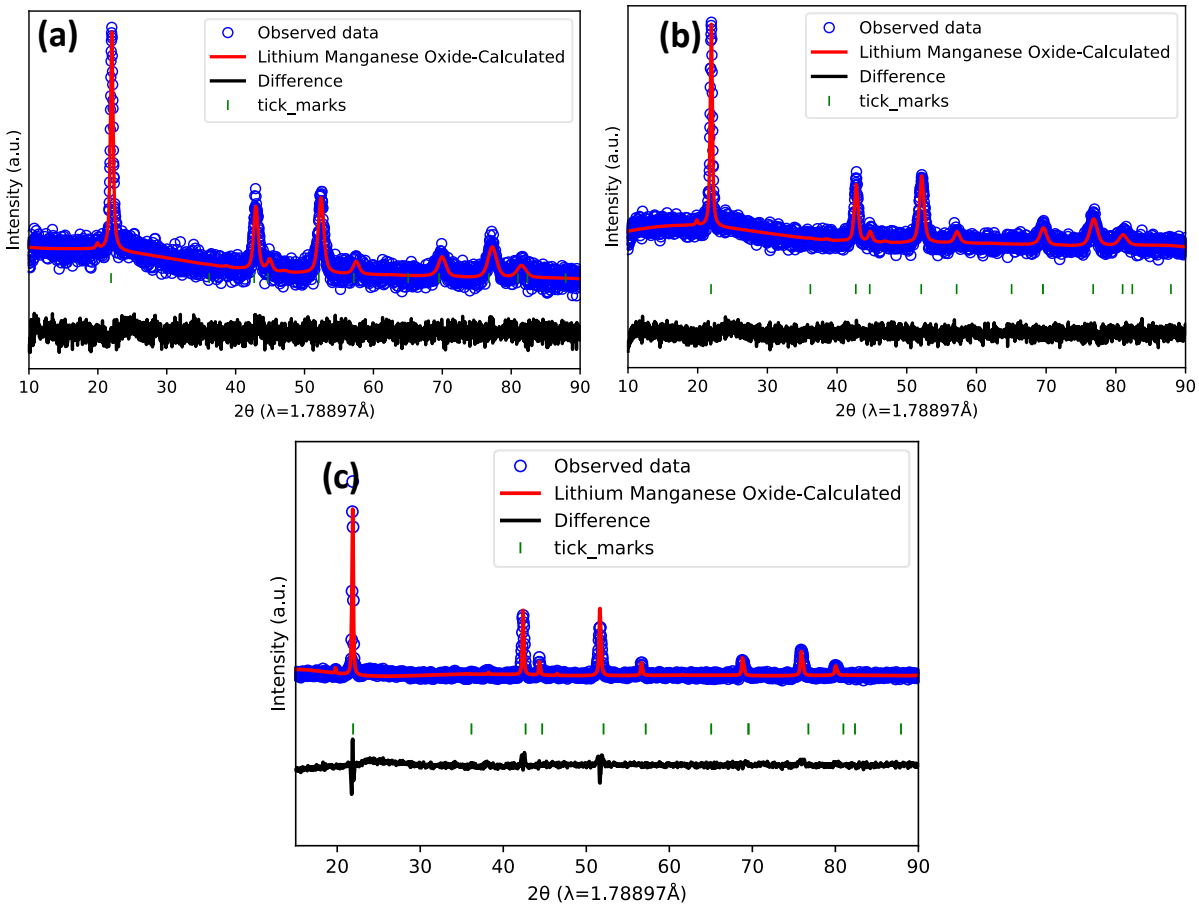

Figure 5.14: Rietveld refinement of $Li_{1.03}Mn_{1.97}O_4$ prepared with $[M_T]$:[Cit] = 1:1 and calcined at (a) 600 °C, (b) 700 °C and (c) 800 °C in air prepared with acetate precursor

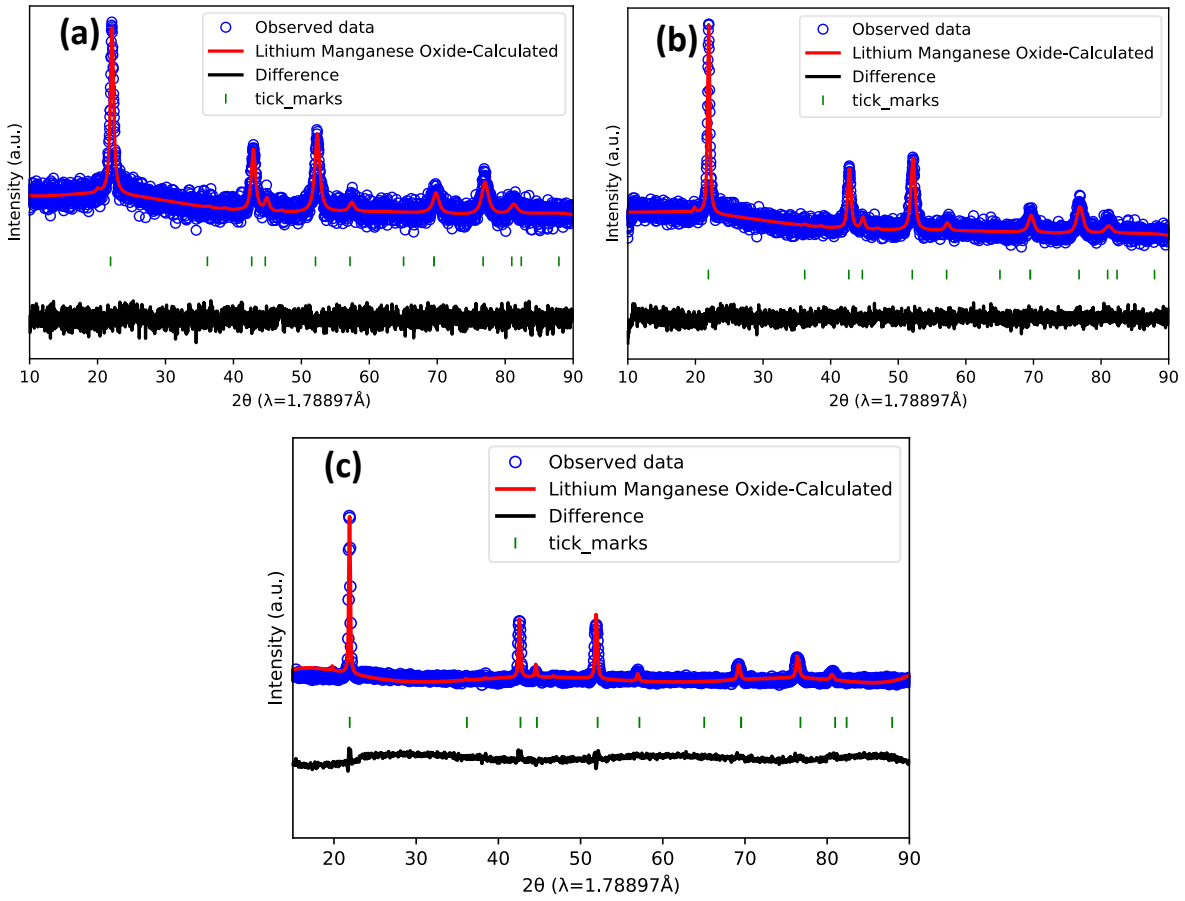

Figure 5.15: Rietveld refinement of $LiAl_{0.4}Mn_{1.6}O_4$ prepared with $[M_T]$: [Cit] = 1: 1 and calcined at (a) 600 °C, (b) 700 °C and (c) 800 °C in air prepared with acetate precursor

Table 5.6: Refined room temperature structural parameters of calcined metal oxides of $Li_{1.03}Mn_{1.97}O_4$ and $LiAl_{0.4}Mn_{1.6}O_4$ with space group *Fd*-3*m* of a cubic model.

	Calcination temperature (°C)	Lattice parameter (Å)	Rexp	Rwp	GOF	Crystallite size (µm)	Volume (Å^3)
$Li_{1.03}Mn_{1.97}O_4$	600	8.1430(2)	1.05	1.08	1.03	4.78(3)	539.94(2)
	700	8.1402(1)	1.09	1.14	1.05	5.48(1)	539.39(3)
	800	8.1387(6)	0.78	2.82	3.60	6.32(3)	539.09(5)
$LiAl_{0.4}Mn_{1.6}O_4$	600	8.1298(2)	1.04	1.10	1.05	4.48(6)	537.32(4)
	700	8.1251(3)	1.06	1.09	1.03	5.25(3)	536.39(1)
	800	8.1123(4)	0.82	3.66	4.50	6.63(2)	533.86(2)

For comparison the diffraction patterns for $Li_{1.03}Mn_{1.97}O_4$ prepared from nitrate and acetate salts with $[M_T]$:[Cit] = 1:1 and calcined at 800 °C, are overlayed in Fig.5.16. The clear additional peak when using the nitrate salts was seen at about 52° 2θ emphasising a mixture of phases

in this case. The $Li_{1.03}Mn_{1.97}O_4$ prepared from acetate salts shows a single-phase metal oxide. These pattern shows the main peaks occurring at slightly different angles due to variation on lattice parameter as an effect of different decomposition of materials.

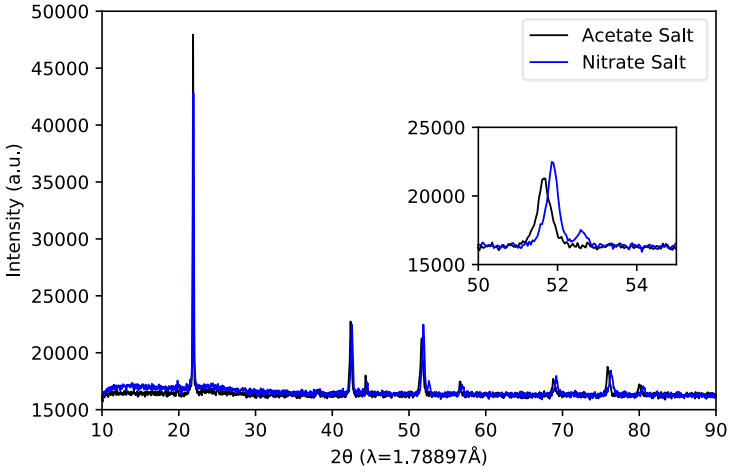

Figure 5.16: Comparison of diffraction patterns for $Li_{1.03}Mn_{1.97}O_4$ prepared using acetate and nitrate salts and calcined at 800 °C for 5 hours in air.

5.3. Conclusion

The attempt to synthesize $Li_{1.03}Mn_{1.97}O_4$ and $LiAl_{0.4}Mn_{1.6}O_4$ by utilizing metal nitrate salts to form the precursors which were then calcined at 380 °C up to 700 °C was successful and the diffraction data showed the presence of the pure cubic spinel structure with *Fd*-3*m* space group. It was observed that metal oxides prepared with $[M_T]$: [Cit] = 1: 1 have high crystallinity when compared with other metal oxides when calcined at 380-500 °C. When increasing the calcining temperature to 800 °C the undoped $Li_{1.03}Mn_{1.97}O_4$ starts to degrade and another phase related to dilithium manganese oxide with a monoclinic crystal system started to form. Doping with aluminium prevented this degradation from occurring at 800 °C. This was also the case when calcining precursors prepared using acetate salts. Calcining acetate-based precursors at moderate temperatures of 400 °C and 500 °C results in metal oxides with low crystallinity when compared to that with nitrate-based precursors.

5.4. References

[1] J. Zheng, P. Yan, L. Estevez, C. Wang and J.-G. Zhang, "Effect of calcination temperature on the electrochemical properties of nickel-rich $LiNi_{0.76}Mn_{0.14}Co_{0.10}O_2$ cathodes for lithium-ion batteries," *Nano Energy,* vol. 49, pp. 538-548, 2018.

[2] G. Maino, J. D'Haen, F. Mattelaer, C. Detavernier, A. Hardy and M. K. Van Bael, “Effects of annealing atmosphere on $LiMn_2O_4$ for thin film Li-ion batteries from aqueous chemical decomposition,” *Jornals of Materials Chemistry,* vol. 4, pp. 18457-18469, 2016.

[3] S. Schlueter, R. Genieser, D. Richards, H. E. Hoster and M. P. Mercer, “Quantifying structure dependent responses in Li-ion cells with excess Li spinel cathodes: Matching voltage and entropy profiles through mean field models,” *Physical Chemistry Chemical Physics ,* vol. 20, no. 33, pp. 1-15, 2018.

[4] X. van Niekerk, E. E. Ferg, C. Gelant and D. G. Billing, “An investigation into the temperature phase transitions of synthesized lithium titanate materials doped with Al, Co, Ni and Mg by in situ powder X-ray diffraction,” *Powder Diffraction,* vol. 35, no. 4, pp. 233-246, 2020.

[5] K. I. Hamad and Y. Xing, “Stabilizing Li-rich NMC materials using precursor salts with acetate and nitrate anions for Li-ion batteries,” *Batteries,* vol. 5, no. 69, pp. 1-14, 2019.

[6] W. Hua, S. Wang, M. Knapp, S. J. Leake, A. Senyshyn, C. Richter, M. Yavuz, J. R. Binder, C. P. Grey, H. Ehrenberg, S. Indris and B. Schwarz, “Structural insights into the formation and voltage degradation of lithium and manganese rich layered oxiedes,” *Nature Communications,* pp. 1-11, 2019.

[7] E. Lee, S. Muhammad, . T. Kim, . H. Kim, . W. Lee and W. Yoon, “Tracking the influence of thermal expansion and oxygen vacancies on the thermal stability of Ni-rich layered cathode materials,” *Advanced Science,* vol. 7, no. 12,pp. 1-18, 2020.

[8] H. Ronduda, Z. Magdalena, A. Szczesna-Chrzan, T. Trzeciak, A. Ostrowski , . D. Szymanski, W. Wieczorek, W. Raróg-Pilecka and M. Marcinek, “On the sensitivity of the Ni-rich layered cathode materials for Li-ion batteries to the different calcination conditions,” *Nanomaterials,* vol. 10, no. 2018, pp. 1-20, 2020.

[9] S. K. Mishra and G. Ceder, “Structural stability of lithium manganese oxides,” *Physical review B,* vol. 59, no. 9, pp. 6120-6130, 1999.

[10] G. Yuwen, W. Shougui, g. Fei, G. Changqing, D. Jipeng and C. Guanghui, “Al and Cr ions co-doped spinel manganese lithium ion-sieve with enhanced Li^+ adsorption performance and structural stability,” *Microporous and Mesoporous Materials,* vol. 351, no. 1, pp. 112492-112504, 2013.

[11] A.-H. Marincas and P. Ilea, “Enhancing lithium manganese oxide electrochemical behavior by doping and surface modifications,” *Coatings,* vol. 11, no. 4, pp. 1-35, 2021.

[12] H. Wang, R. Gao, Z. Li, L. Sun, Z. Hu and X. Lu, “Different effects of Al substitution for Mn or Fe on the structure and electrochemical properties of $Na_{0.67}Mn_{0.5}Fe_{0.5}O_2$ as a sodium ion battery cathode material,” *Inorganic Chemistry,* vol. 9, pp. 5249-5257, 2018.

[13] Q. Pei, . M. Lu, X. Liu, D. Li, . X. Rao, . Z. Lu and S. Zhong, “The effects of Al-doped to cathode material based on hollow microspheres of nickel-manganese on sodium-ion batteries,” *Nanotechnology,* vol. 32, no. 39,pp. 672-691, 2021.

[14] H. Yu, Y.-G. So, Y. Ren, T. Wu, G. Guo, R. Xiao, J. Lu, H. Li, L. Yang, H. Zhou, R. Wang, K. Amine and Y. Ikuhara, “Temperature-sensitive structure evolution of lithium–manganese rich layered

oxides for lithium-ion batteries," *Journal of the American chemical society,* vol. 140, pp. 15279-15289, 2018.

[15] R. Pulido, N. Naveas, T. Graber, R. Martin-Palma, F. Agulló-Rueda, I. Brito, C. Morales, L. Soriano, L. Pascual, C. Marini, J. Hernández-Montelongo and M. M. Silvan, "Hydrothermal control of the lithium-rich Li_2MnO_3 phase in lithium manganese oxide nanocomposites and their application as precursors for lithium adsorbents," *Dalton Transaction,* vol. 50, pp. 10765-10778, 2021.

[16] X. Dong, H. Wang, J. Wang, Y. He, P. Yang, S. Wang, J. Chen, C. Yang and F. Lu, "The effects of calcination on the electrochemical properties of manganese oxides," *Journal of Advanced Nanoscale,* vol. 5, pp. 5309-5321, 2023.

[17] C. Zhenfei, M. Yangzhou, H. Xuanning, Y. Xiaohui, Y. Zexin, Z. Shihong, S. Guangsheng, X. Youlong, W. Cuie and Y. Weidong, "High electrochemical stability of Al-doped spinel $LiMn_2O_4$ cathode material for Li-ion batteries," *Journal of Energy Storage,* vol. 27, pp. 101036-101045, 2020.

Chapter 6: Investigating crystallographic structure using local and average structure refinements

Abstract: The synchrotron XRD and PDF analysis of both $Li_{1.03}Mn_{1.97}O_4$ and $LiAl_{0.4}Mn_{1.6}O_4$ prepared using nitrate metal salts as starting materials at 380 °C and 450 °C, forms a cubic spinel-based structure. There was a direct correlation between the two analyses where both the local and average structure analysis exhibit comparable crystallographic information, and phase purity of the metal oxide. The pair distribution function and X-ray diffraction of the final products shows a comparable lattice parameter to confirm the formation of the same final metal oxide.

6.1. Synchrotron X-ray diffraction analysis of metal oxide produced at moderate temperatures

6.1.1. Undoped lithium manganese oxide

Synchrotron powder X-ray diffraction (SPXRD) was used to further explore the phases produced at various stages in the synthesis since it provides high-resolution diffraction data with high signal-to-noise ratios. Following the DTA and TGA results (see chapter 4), it was observed that at temperatures above 380 °C there appears to be no further effect on the phase produced but does affect the crystallite size and cell volume of the final product. There is also no further weight loss or phase instability (particularly if $[Cit] \geq [M_T]$) and this was observed from the *ex-situ* XRD (see chapter 5). Therefore, further analysis was thus done on the materials that were synthesized using metal nitrate salts and with 1:1 total metal to citric acid ratio, and the dried precursor was then calcined at two separate temperatures, namely 380 °C or 450 °C, for 5 hours in the air.

The SPXRD patterns were plotted in Q (moment transfer) instead of 2θ (scattering angle) to compare synchrotron and laboratory XRD patterns independent of the wavelength. The synchrotron diffraction patterns (Fig.6.1) show the cubic spinel structure was formed, and spinel peaks at the higher Q values were observed. The SPXRD shows high resolution diffractograms with peaks indicated by ▲ being more pronounced than those detected by laboratory PXRD. This clearly shows the importance of using high-resolution diffraction data for more in-depth understanding of materials. From visual inspection, the peaks for this material show higher intensity (i.e. increased crystallinity) and occur at slightly higher Q values (i.e. lattice parameter contraction) for the sample calcined at the higher temperature.

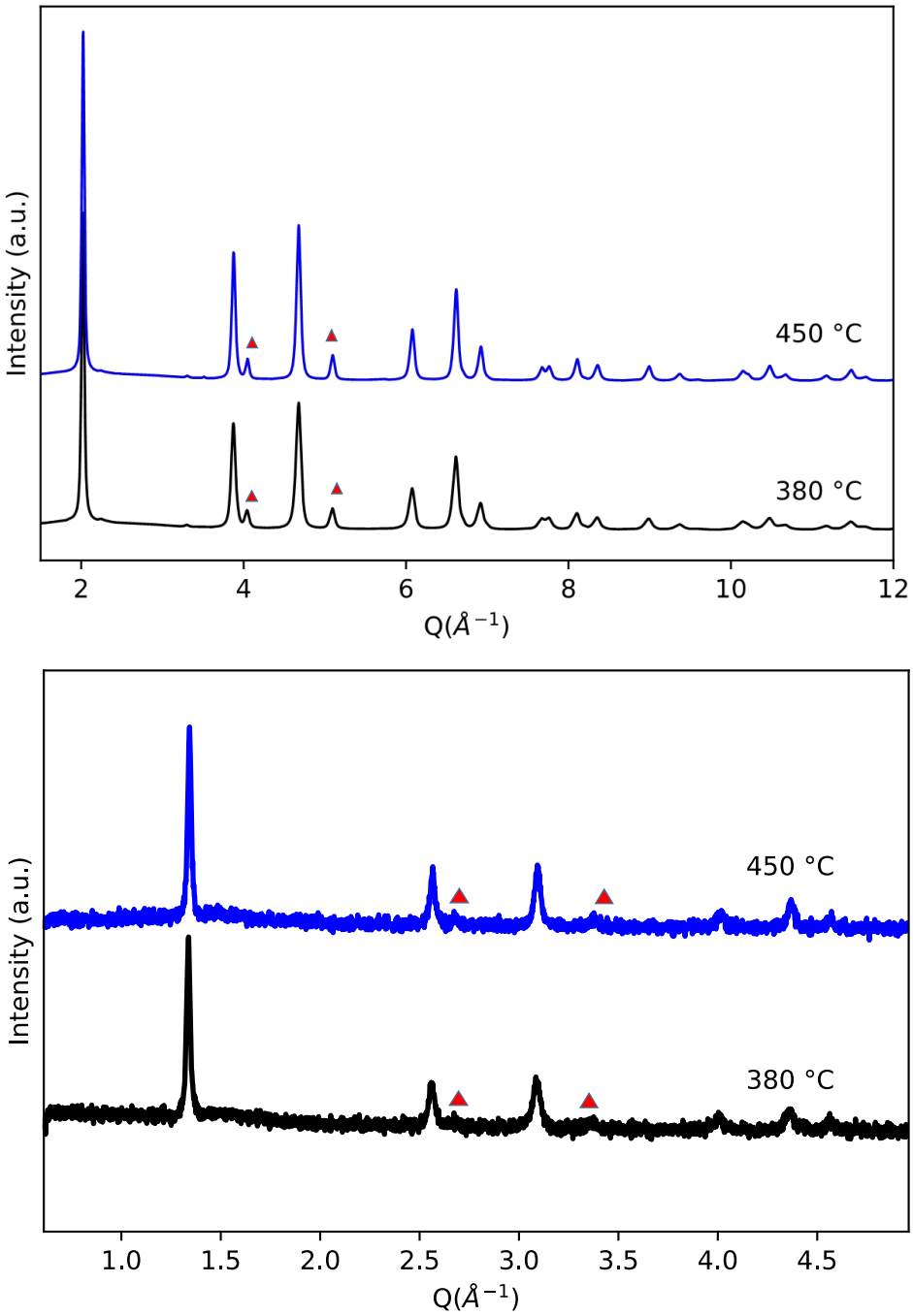

Figure 6.1: Diffraction patterns of $Li_{1.03}Mn_{1.97}O_4$ prepared with a [M_T]:[Cit] = 1:1 and calcined at 380 °C or 450°C for 5 hours in the air, with (a.) SPXRD and (b.) Laboratory XRD data. Peaks indicated by ▲ highlight some of the peaks which are barely visible by lab XRD, but are clearly visible by SXRD.

The Rietveld refinements clearly indicate $Li_{1.03}Mn_{1.97}O_4$ materials (calcined at 380 °C or 450 °C) displayed the cubic spinel structure (space group *Fd*-3*m*) and that there are no impurity phases present (Fig.6.2). This shows that when calcining the starting material precursor at either 380 °C or 450 °C, the required product phase is already formed with the crystallinity increasing at the higher calcination temperature (i.e. 450 °C). Parameters obtained from Rietveld refinement confirmed the decrease in lattice dimension as the calcination temperature was increased (Table.6.1), similar response was noticed to the crystallite size as increasing the calcination temperature. These materials show a similar behaviour with those

in chapter 5 due to the increase in calcination temperature results in a decrease in lattice dimensions.

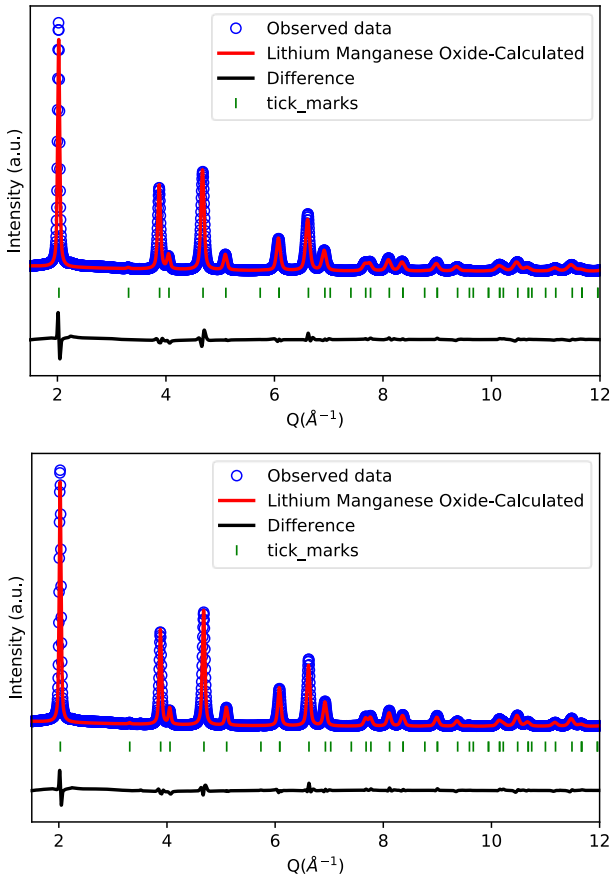

Figure 6.2: Rietveld refinements of $Li_{1.03}Mn_{1.97}O_4$ prepared with [M_T]: [Cit] =1: 1 and calcined at (a) 380 °C and (b) 450 °C displaying the cubic spinel crystal structure (space group *Fd*-3*m*).

Table 6.1 Lattice parameters and crystallite size of 1:1 [M_T]: [Cit] of $Li_{1.03}Mn_{1.97}O_4$ calcined at various temperatures obtained from Rietveld refinements.

Calcination temperature (°C)	Lattice parameter (Å)	Crystallite size (µm)	Volume (Å^3)	Rexp	Rwp	GOF
380	8.1667(2)	0.035(1)	544.68 (4)	12.93	13.65	1.05
450	8.1601(1)	0.036(3)	543.36 (5)	11.88	12.52	1.06

6.1.2. Al-doped lithium manganese oxide

Careful observation of the synchrotron diffraction patterns (Fig.6.3) produced by the $LiAl_{0.4}Mn_{1.6}O_4$ samples, prepared with [M_T]:[Cit] of 1:1 and calcined at 380 °C or 450°C, indicate a clear formation of crystalline material with the cubic spinel structure, additional peaks that are not related to the cubic spinel are seen between the major peaks (indicated by ★), these peaks were not seen when comparing with SPXRD of undoped samples which appears clearly on both the Al-doped samples. It was noticed that some of these peaks disappears/ have reduced intensity when heating the material to 450°C. The $LiAl_{0.4}Mn_{1.6}O_4$

metal oxide calcined at 380 °C showed slightly better crystallinity than that calcined at 450°C, contrary to expectation, but this may simply be due to slight differences in the dried starting precursor gels since these were to distinct samples.

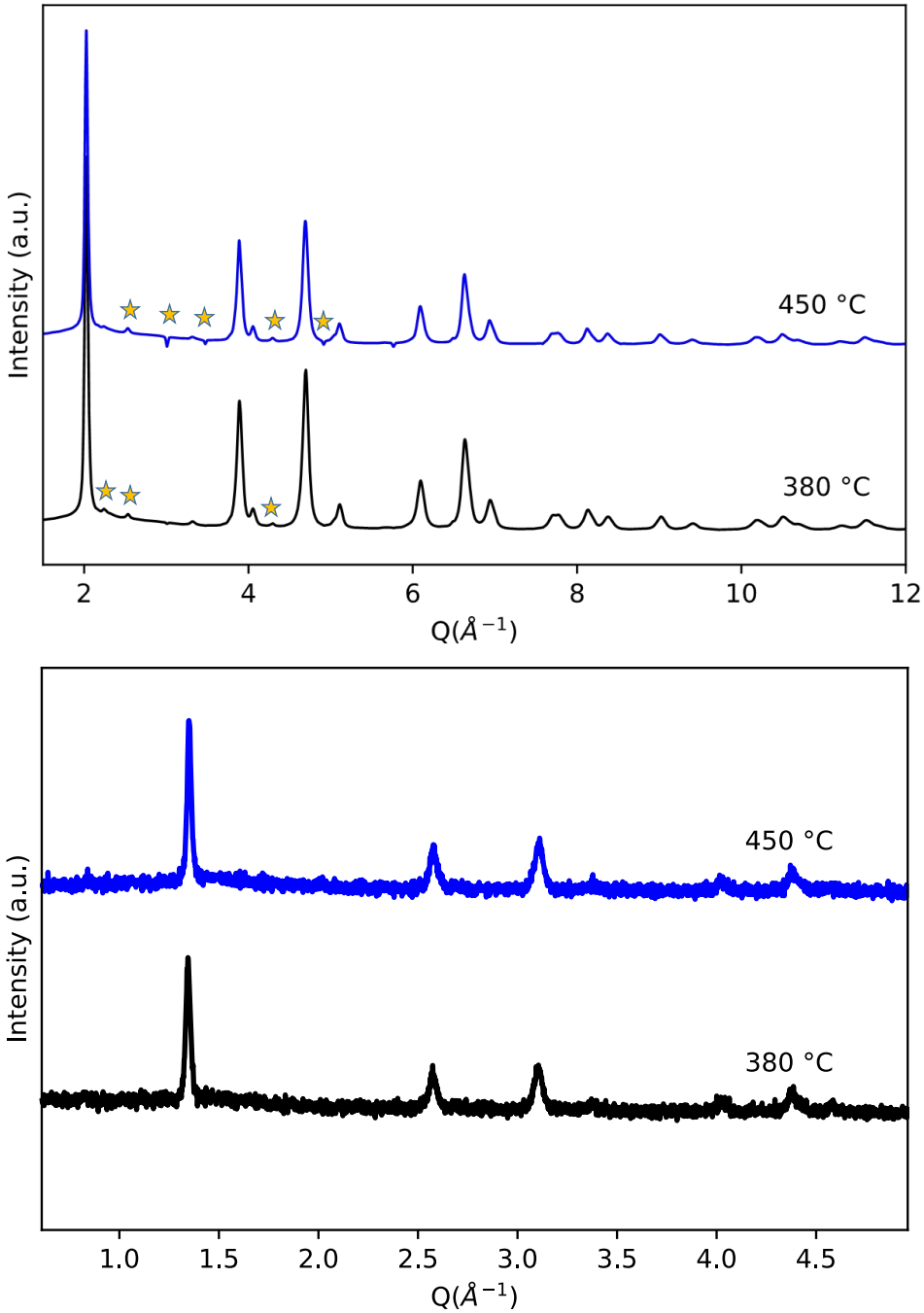

Figure 6.3: Diffractograms of $LiAl_{0.4}Mn_{1.6}O_4$ prepared with [M_T]: [Cit] = 1:1 and calcined at 380 °C or 450 °C for 5 hours in the air with (a.) SPXRD and (b.) Laboratory XRD, with ★ representing undefined peaks.

The Rietveld refinements of confirmed the formation of the cubic spinel structure for at both calcination temperatures (Fig.6.4), but the peaks indicated by ★ are not part of the spinel

structure and does not correspond to that for Al_2O_3 or citric acid, which might indicate a formation of impurities on materials doped with aluminium.

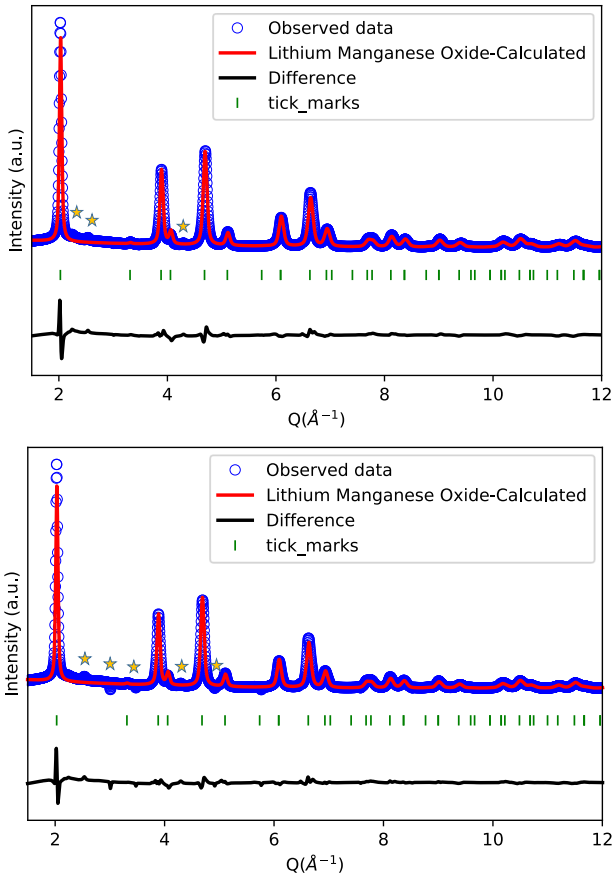

Figure 6.4: Rietveld refinements of the diffraction patterns for $LiAl_{0.4}Mn_{1.6}O_4$ prepared with [M_T]:[Cit] of 1:1 and calcining the precursor at (a) 380 °C, (b) 450 °C. The peak indicated by ★ corresponds to that in Fig. 6.3.

Rietveld refinement also confirmed a decrease in lattice dimension as the temperature was changed from 380 °C to 450°C (Table.6.2), however, the crystallite size increased when calcining at slightly higher temperature. The SPXRD lattice parameters are similar to the laboratory analysis in chapter 5 of the Al-doped samples.

Table 6.2: Lattice parameters and crystallite size of $LiAl_{0.4}Mn_{1.6}O_4$ prepared at 1:1 [M_T]: [Cit] obtained from Rietveld refinements.

Calcination temperature (°C)	Lattice parameter (Å)	Crystallite size (µm)	Volume (Å^3)	Rexp	Rwp	GOF
380	8.1320(3)	0.029(1)	537.76 (2)	12.23	13.35	1.04
450	8.1315(3)	0.036(2)	537.65 (1)	13.37	14.65	1.07

6.2. Pair distribution function analysis

The pair distribution function shows the probability of finding two atoms a distance r apart in the material; this is related to the peak position on the G(r) versus r plot. The distribution of atom-to-atom distances has a gaussian shape which results from atomic disorder in the peak position resulting in the distribution of the interatomic spacing, which is also related to the unit cell and geometry. The height of the peak corresponds to the scattering factors, where atoms with greater scattering factors produce higher peaks and also the probability itself. Gallo *et al.* [1] presented that the PDF peaks have different information regarding the local structure with the area under the curve represents the coordination number and occupancy for the corresponding atom-to-atom pair, in addition, the peak width is related to the disorder of atoms due to vibrations and excessive thermal motion at elevated temperatures whereas the wider peaks suggest the broader distribution of interatomic distances.

The $Li_{1.03}Mn_{1.97}O_4$ PDF integrated data was processed using xPDFsuite to generate S(Q) and the PDF G(r). The pair distribution function (Gr) curves were collected between 1.5 < r < 25 Å, these PDF data was then truncated at Q_{max}= 22.0 $Å^{-1}$ which was found to be an acceptable range of Q to maximize the real space resolution while avoiding termination effect. PDF analysis was carried out using small box method in Bruker AXS TOPAS-Academic Version 6, with the wavelength and peak shapes being calibrated using 640d (silicon powder) where the real space refinement accuracy is defined by the agreement factor Rw.

Since the material calcined at 380 °C or 450 °C throughout was crystalline, it allows for short interatomic distances analysis by assigning some G(r) peaks to a pair of atoms in the average *Fm-3m* crystal structure. The PDF model shows peaks at high r-values (10 < r < 25 Å) which corresponds to the average structure, and the peaks at low r-values (1.5< r < 10 Å) relate to the local structure of the crystalline material.

6.2.1. Undoped lithium manganese oxide PDF analysis

The same samples presented in SPXRD above are the ones analysed for PDF/total scattering refinements. This was modeled, using a small box model, with the cubic spinel structure (with space group *Fd*-3*m*) as was used for the X-ray diffraction patterns. The PDF refinements confirm the presence of the cubic spinel phase without any impurities in the local structure (Fig.6.5). Diaz-Lopez *et al.* [2] presented local structure and lithium diffusion pathways in $Li_4Mn_2O_5$, showing the first big peak around 2 Å allocated to the overlap of Mn-O and Li-O nearest neighbor distance, with the small peaks related to the second peak just below 3 Å allocated as Mn-Li and Mn-Mn bonds overlapped, it was noted that the third peak about 3.5 Å is allocated to an overlap of Mn-O and Li-O. These peaks were also clearly observed in $Li_{1.03}Mn_{1.97}O_4$ calcined at 380 °C or 450 °C (Fig.6.5). Ammundsen *et al.* [3] reported $LiMn_2O_4$ refined by EXAFS showing Mn-O as the first coordination shell due to the shortest interatomic distances (r = 1.904 Å) followed by the second coordination shell related to Mn-Mn (r = 2.841

Å); also clearly related to $Li_{1.03}Mn_{1.97}O_4$. These coordination shells were also confirmed by Yany *et al.* [4] when studying Li_2MnO_3 electrode structure.

$Li_{1.03}Mn_{1.97}O_4$ material calcined at 380 °C or 450 °C shows the first peak related to the Mn-O coordination shell around 2 Å, with the second peak just below 3 Å related to the Mn-Mn coordination shell. Lee *et al.* [5] reported that the higher the oxidation states of Mn decreases the Mn-Mn bonds which will cause changes in the Mn-O bond distances indicates if there is lithium extraction in the structure during different degrees of oxidation-reduction of $LiMn_2O_4$ From the PDF refinements, the local structure reasonably interprets the experimental G(r) which displayed that lithium, manganese, and oxygen atoms retained their atomic positions of 8a, 16d, and 32e respectively, according to the *Fd*-3*m* symmetry. Here manganese atoms are coordinated to six oxygen atoms with approximately equal Mn-O distances which resulted in the first coordination shell and the second shell is formed by six approximately equal Mn-Mn distances in neighboring octahedral sharing edges of $[MnO_6]$ as discussed by Ammundsen *et al* [3].

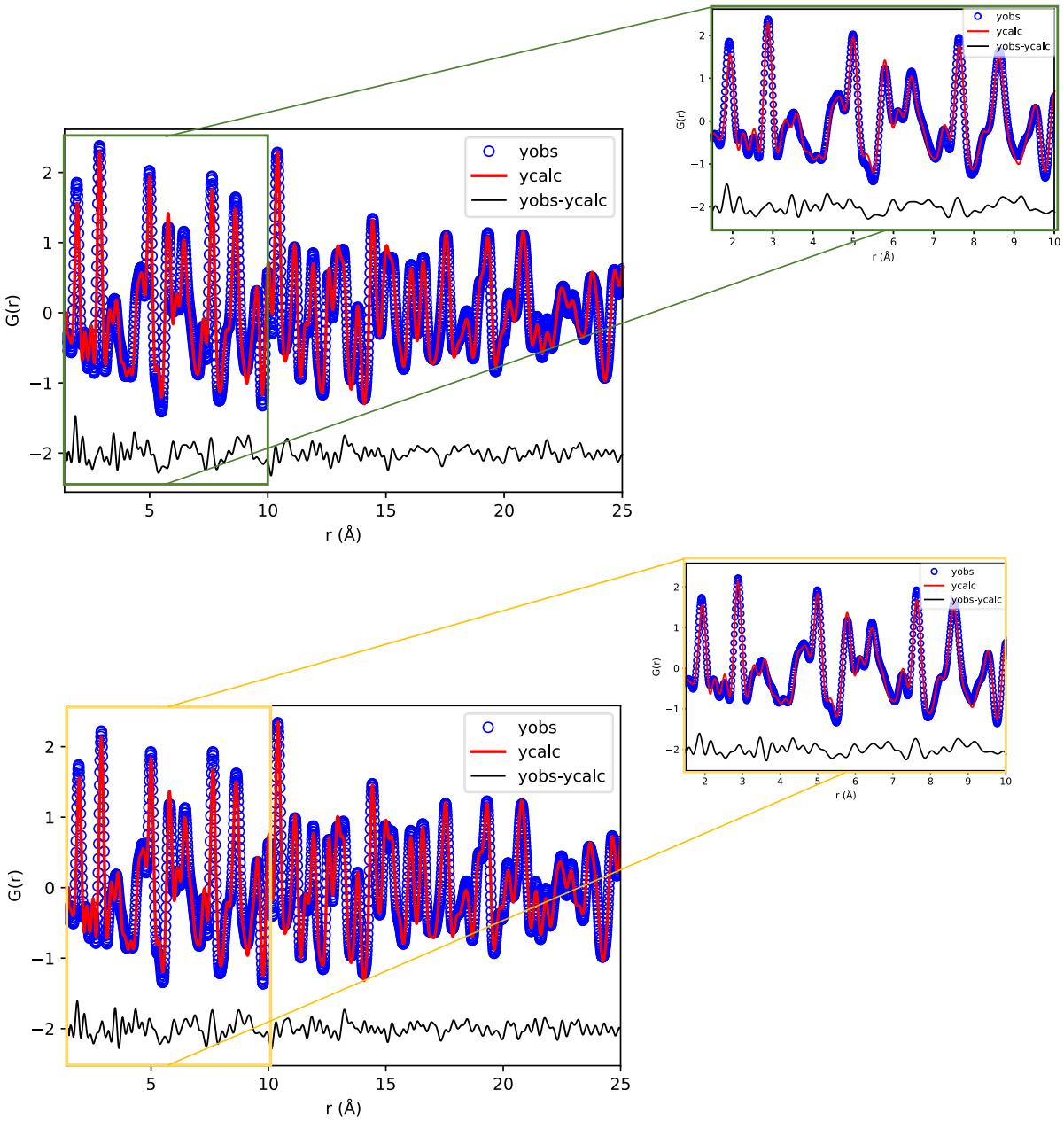

Figure 6.5: Small box refinements of PDF data for $Li_{1.03}Mn_{1.97}O_4$ prepared from [MT]:[Cit] = 1: 1 with space group *Fd*-3*m* of a cubic spinel crystal structure with samples calcined at (a) 380 °C, and (b) 450 °C. The absence of phase correction on the peaks means they are displayed ~0.4 *Å* lower than the structural values.

Both local structure PDF models of 380 °C and 450 °C were in good agreement with the refined structure which results in a reasonable fit based on the statistical Rw in Table.6.5. When observing the PDF models in the high r-value range, it shows that the average structure in XRD and PDF are in good agreement (lower r-values show the local structure and high r-values shows the average structure in PDF).

Table 6.3: Lattice parameters and crystallite size of 1:1 total metal ion to citric acid ratio of $Li_{1.03}Mn_{1.97}O_4$.

Calcination temperature (°C)	Lattice parameter (Å)	Rw (%)
380	8.1652(3)	12.15
450	8.1607(2)	12.02

6.2.2. Al-doped lithium manganese oxide PDF analysis

The PDF refinements of $LiAl_{0.4}Mn_{1.6}O_4$ (from using $[M_T]$:[Cit] = 1:1) is similar to that observed in the undoped material with a cubic spinel phase and space group *Fd*-3*m* without any distinct impurities noted in the average or local structure (Fig.6.6). The local structure interprets the experimental G(r) which displayed that lithium atoms are situated in the 8a sites and aluminium atoms partially replacing some of the Mn atoms in the 16d sites and the oxygen atoms retaining their atomic positions of 32e, the first coordination shell correspond the Mn-O nearest neighbor distance just below 2 Å and based on Diaz-Lopez *et al.* [2] Mn-Mn overlap with Mn-Al overlap just below 3 Å in the second coordination shell based on the *Fd*-3*m* symmetry. For the local structure models, there was good agreement between the calculated and measured structural data. For the PDF results at the high r-values, it shows that the average structure perfectly fit the collected data which reveals an agreement between the XRD and PDF crystallographic information.

The PDF refinement exhibits the lattice dimension contraction as the calcination temperature was increased from 380 °C to 450 °C (Table 6.4), and the lattice parameters obtained by XRD and PDF are in good agreement and show a similar trend which was noticed from the XRD diffraction patterns – the lattice parameters decrease with calcination temperature increase.

Table 6.4: Lattice parameters and Rw for $LiAl_{0.4}Mn_{1.6}O_4$ synthesised using 1:1 total metal ion to citric acid ratio.

Calcination temperature (°C)	Lattice parameter (Å)	Rw (%)
380	8.1581(2)	11.78
450	8.1567(4)	11.65

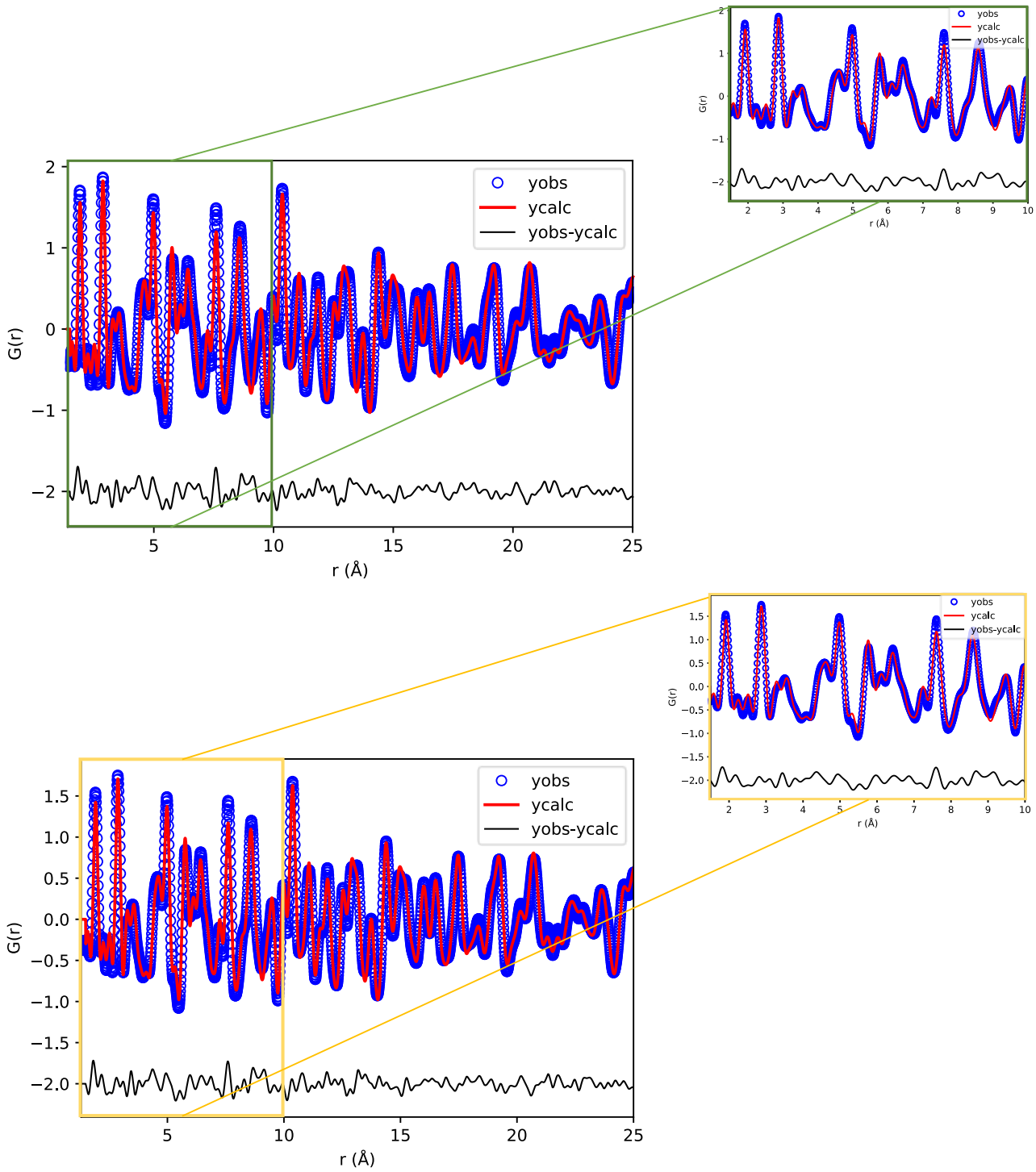

Figure 6.6: Small box refinements of $LiAl_{0.4}Mn_{1.6}O_4$ prepared from 1:1 total metal ion to citric acid ratio with space group *Fd*-3*m* of a cubic spinel crystal structure with samples calcined at (a) 380 °C, (b) 450 °C, the absence of phase correction on the peaks are displayed ~0.4 lower than the structural values.

6.3. Conclusion

The X-ray total scattering local and average structure analysis was achieved by small box modelling showing Mn-O and Mn-Mn bond distances on the first and second coordination shell was similar to those obtained from literature. The local structure refinement of metal oxides prepared using the nitrate precursors exhibits a good agreement between the

experimental G(*r*) and the calculated structural model which confirm a formation of a cubic spinel structure of space group *Fd*-3*m*. $Li_{1.03}Mn_{1.97}O_4$ and $LiAl_{0.4}Mn_{1.6}O_4$ were thus already obtained from calcining precursors at 380 °C or 450 °C with a very slight discrepancies on the local structure. A good correlation between the local and average structure was noticed from the lattice parameters following the Rietveld refinements.

6.4. References

[1] J. Gallo , K. Ohara, E. Carbo-Argibay, S. Kamali-Moghaddam, A. Bansil and K. Pussi, "Structure of manganese oxide nanoparticles extracted via pair distribution functions," *Condensed Matter,* vol. 5, no. 19, pp. 1-10, 2020.

[2] M. Diaz-Lopez, M. Freire, Y. Joyl, C. V. Colin, H. E. Fischer, N. Blanc, N. Boudet, V. Pralong and P. Bordet, "Local structure and lithium diffusion pathways in $Li_4Mn_2O_5$ high capacity cathode probed by total scattering and XANES," *Chemistry of Material,* vol. 30, pp. 3060-3070, 2018.

[3] B. Ammundsen, D. J. Jones and J. Roziere, "Effect of chemical extraction of lithium on the local structure of spinel lithium manganese oxides determined by x-ray absorption spectroscopy," *Chemistry Materials,* vol. 2, pp. 2799-2808, 1996.

[4] Y. Yang, T. Su, y. Jiang, D. Liu, P. Yan, H. Tian and H. Yu, "Atomic pair distribution function research on Li2MnO3electrode structure evolution," *Science Bulletin,* vol. 64, pp. 553-561, 2019.

[5] "Electronic and bonding properties of $LiMn_2O_4$ spinel with different surface orientations and doping elements and their effects on manganese dissolution," *Journal of The Electrochemical Society,* vol. 163, no. 7, pp. 1359-1368, 2016.

Chapter 7: Conclusion

In this investigation, lithium-rich lithium manganese metal oxide ($Li_{1.03}Mn_{1.97}O_4$) and an aluminium doped lithium manganese oxide ($LiAl_{0.4}Mn_{1.6}O_4$), both with a cubic spinel-based structure were synthesized using a sol-gel method and studied in the same conditions. The materials were successfully synthesized using both metal nitrate and metal acetate salts as starting materials, with citric acid as the complexing agent. The metal ions were mixed in correct stoichiometric amounts and dissolved in distilled water before the citric acid was added in varying concentrations. The sol-gel method allowed for a low-temperature, simple, and quick synthesis route that can be easily repeatable.

A mixture of the starting materials formed a gel paste when left on a hot plate at low operating temperatures up to 120 °C in a fairly short period to produce a precursor with good homogeneity. The gel precursor was dried at 140 °C for 5 hours and exhibited a crystalline phase of Δ-aqua-S-citrato(2-)-manganese(II) [$Mn(C_6H_6O_7)(H_2O)$], indicating initial metal-ligand complex formation. The TGA of the dried starting precursors showed multiple decompositions, where the decomposition of organic and nitrate components occur in two separate steps with the first exothermic peak at around 300-350 °C shows the removal of the nitrates and the second indicates the removal of the organic content at around 350-380 °C. It was noteworthy that when the precursor materials are prepared using the nitrate salts, the sought-after metal oxide forms at the moderate temperature of 380 °C, as the TGA indicates that the material is stable with no further mass loss. For precursor materials prepared using the acetate salts, the metal oxide forms at a slightly higher temperature of 400 °C.

The Rietveld refinements of the Al-doped and undoped metal oxides show a comparable response with no apparent consequence on the phase formation, where the cubic spinel crystal structure of space group *Fd*-3*m* was observed when calcined at moderate temperatures, namely 380 °C, 400 °C, 500 °C and 600 °C for nitrate-based precursors. However, when increasing the calcination temperature to 800 °C, the undoped materials form an additional monoclinic phase of dilithium manganate as an impurity, while the aluminium doped material showed structural stability with not additional phases being detected. When calcining the acetate-based precursors below 400 °C, an amorphous material was observed with the sought-after metal oxide only forming at temperature 400 °C as above as supported by the STA data. Increasing the calcination temperature to 800 °C does not show any formation of impure phases.

A slight shrinkage in the lattice dimensions was observed when increasing the calcination temperature which is likely due to more ordering in the unit cell, and this also relates to the crystallite size which increases with increasing calcination/annealing temperature. When comparing lattice dimensions between the undoped and Al-doped samples, it was noted that doping with aluminium reduces the lattice parameters as the smaller Al^{3+} ions partially substitute the larger Mn ions. It was evident that metal oxides prepared from nitrate

precursor of [M_T]: [Cit] = 1: 1 have high crystallinity and retained about 30% mass after decomposition than other materials.

When comparing the analysis of the PDF models against that of the XRD patterns, it was found that they are in good agreement, meaning the local and average structures are consistent. The PDF small box refinements difference plot has resulted in a better-quality fit with fewer discrepancies between the observed and calculated model. In conclusion, this demonstrates that it is possible to use the nitrate salts as starting materials to produce the desired lithium metal oxide at moderate temperatures using a 1:1 total metal ion to citric acid ratio (i.e. excess citric acid is not required).

Future work

Using this approach, 30% of the initial mass (of the dried precursor) was retained, thus further investigation into the *in-situ* XRD measurements as a function of temperature is worth considering to carefully track the phase changes as a function of temperature from room temperature to 850 °C. A flow cell design is worth completing to be able to perform accurate *in-situ* XRD measurements in the laboratory with high signal-to-noise ratio for better understanding of the data.

Appendices

Appendix 1: Furnace Calibration

When working with battery materials, it is critical to accurately control and maintain the temperature of the furnace used when preparing the metal oxides. This calibration aimed to gain confidence in the proportional integral derivative (PID) controller (the digital temperature control of the furnace) by comparing the measurements of the PID controller with an independent measurement taken by another device. During this calibration, a thermocouple connected to a digital thermometer was utilized.

The tube furnace used employs a differential thermocouple which measures temperatures at two regions in the tube and uses the average as the actual furnace temperature. Different heating rates give different error margins between the set temperature and the actual temperature of the furnace. This was observed when heating at a fast rate (20 °C/min), the actual temperature reading surpasses the set furnace temperature by 150-270 °C depending on the set temperature. When heating at a slow rate (5 °C/min) the actual temperature will surpass the set temperature by only 5 to 8 °C depending on high the temperature was set. At higher temperatures (about 600-900 °C) a significant discrepancy was observed resulting in higher error margins compared to the lower temperature range (about 400-500 °C). Therefore, a heating rate of 5 °C/min was always used. The temperature of a tube furnace can also be affected by the environments temperature since the air can easily flow through the tube if the sides are open (even if the furnace room door is closed).

When doing the calibration, the external thermocouple was placed inside the tube, in the middle where the boat crucible is usually placed during the heating process so that the change in temperature was analysed in the same spot where the material to be calcined was placed. The calibration curve for the tube furnace (Fig.A1) shows that when heating at high temperatures there is a slight discrepancy between the temperature from the external thermocouple and the furnace set temperature, however, a straight-line relation was still observed. it is easier to estimate the set temperature was thus adjusted using the relationship below so that the sample is at the wanted temperature:

$$T(set\ temperature) = 0.9582 \times\ (desired\ temperature) - 2.9286.$$

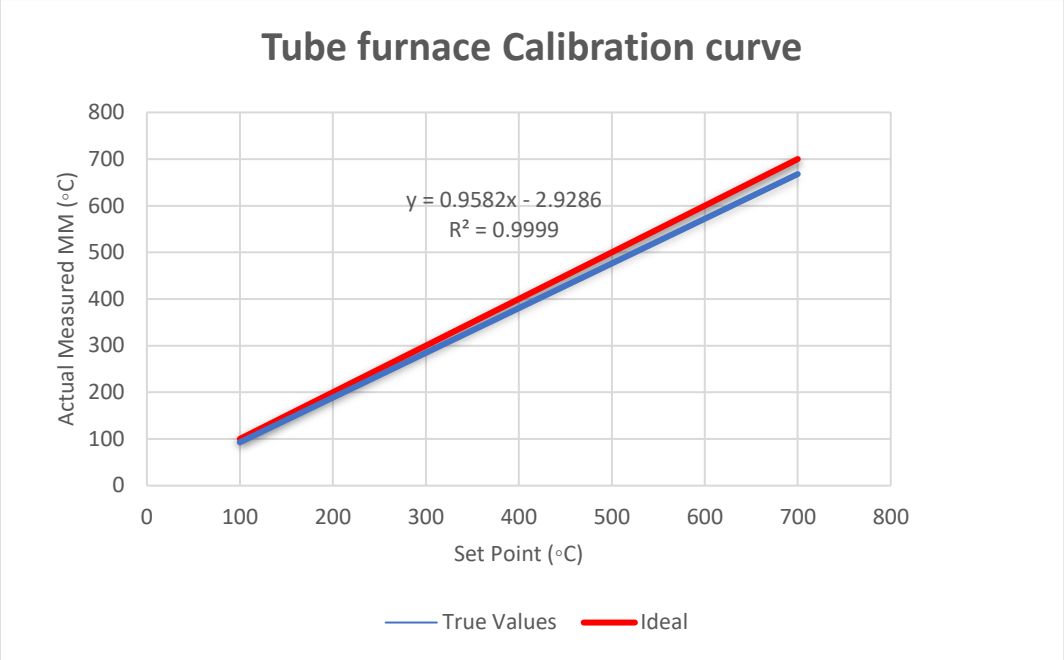

Figure A1: Tube furnace calibration curve showing the true values (Set temperature) and ideal values (desired temperature)

Appendix 2: Flow cell design

Part of this project was to design and construct a versatile flow cell that can be used to do *in-situ* X-ray diffraction measurements of various solid-state materials as a function of temperature. The flow cell will be used in a conventional laboratory powder X-ray diffractometer which has the space and configuration to accommodate it. The idea is to allow for accurate temperature control of the gradient heater that is mounted between the sample capillary. The configuration of the flow cell is such that X-rays can reach a portion of the heated capillary to continuously measuring the data.

The flow cell is designed (Fig.A2.1) with precise measurements of mounting blocks to be assembled by ground rods; the sample capillary is mounted on the Swagelok fitting. The gradient heater was designed by uniform winding of heating wire (kanthal wire) on the ceramic bar and placed the heat shields to minimize heat loss, these heating elements are mounted above and below the sample capillary to better temperature control.

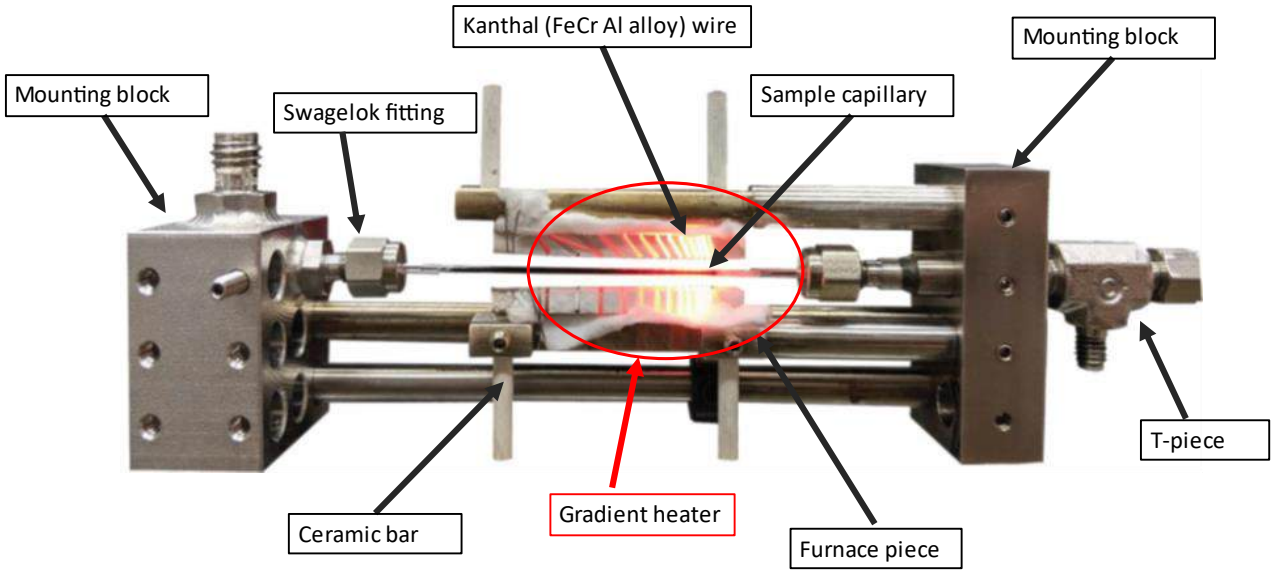

Figure A2.1: A flow-cell design used with associated components/ parts [1].

The flow cell was not completed, but the engineering drawings used to designed parts of the cell (done using Autodesk Fusion 360) are presented in Figures A2.2 -A2.4.

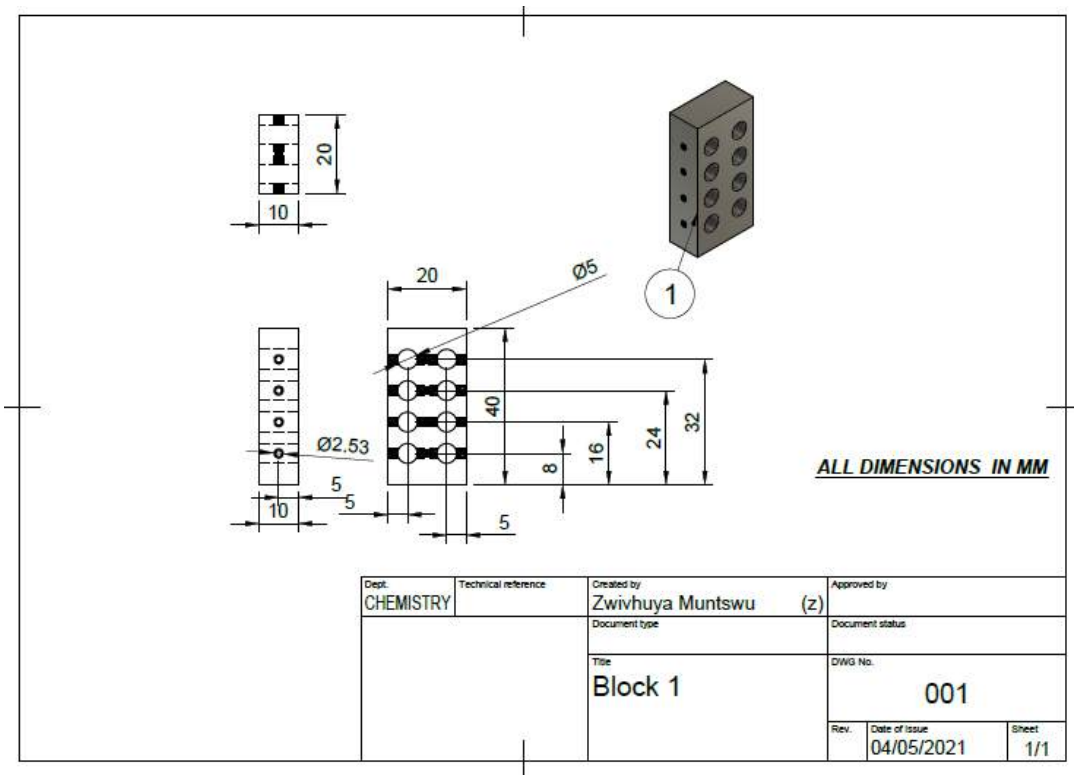

Figure A2.3: Flow cell Block 1 design

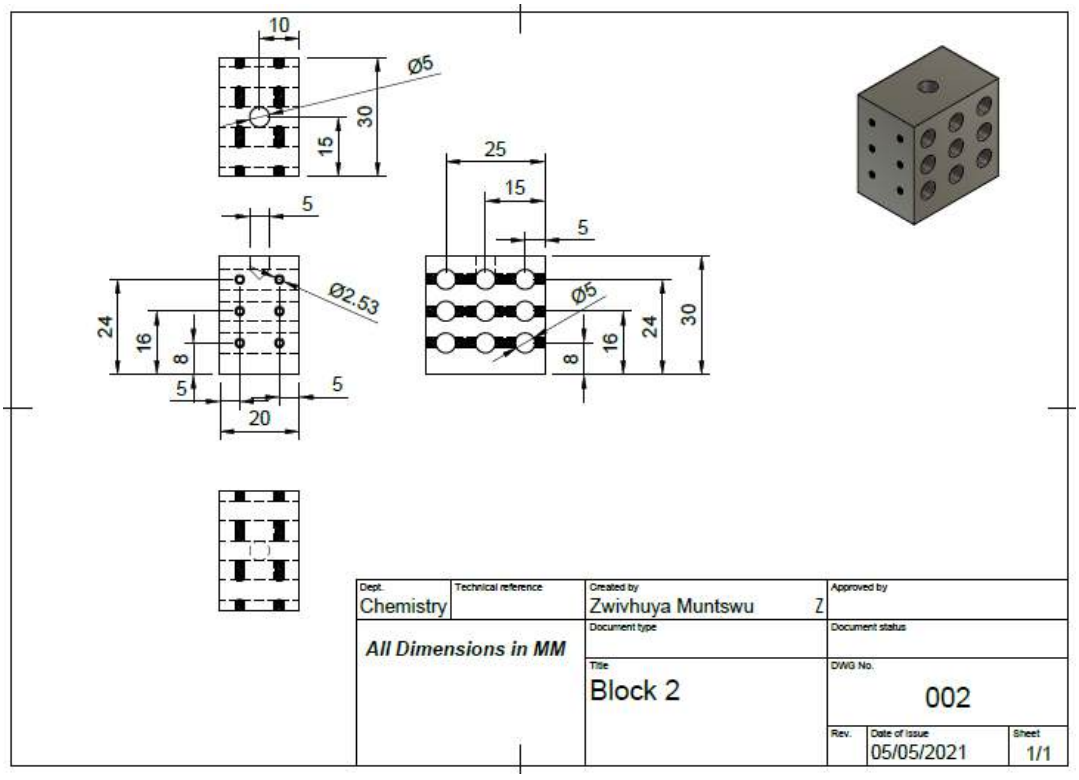

Figure A2.4: Flow cell Block 2 design

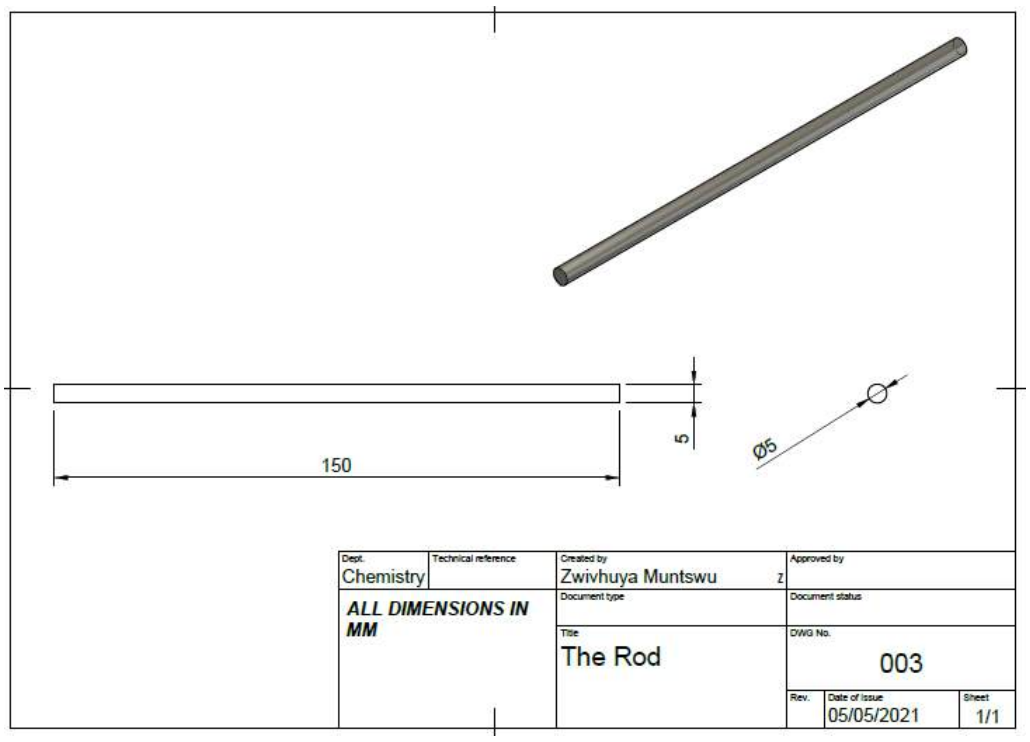

Figure A2.5: Flow cell rod design

After blocks 1 and 2 were designed, they were machined using stainless steel as shown in Fig.A2.5. Kanthal wire was purchased to use as the heating element. This will be formed into a coil which will fit around the capillary which contains the sample. Completion of the flow cell and further testing of the device is still required.

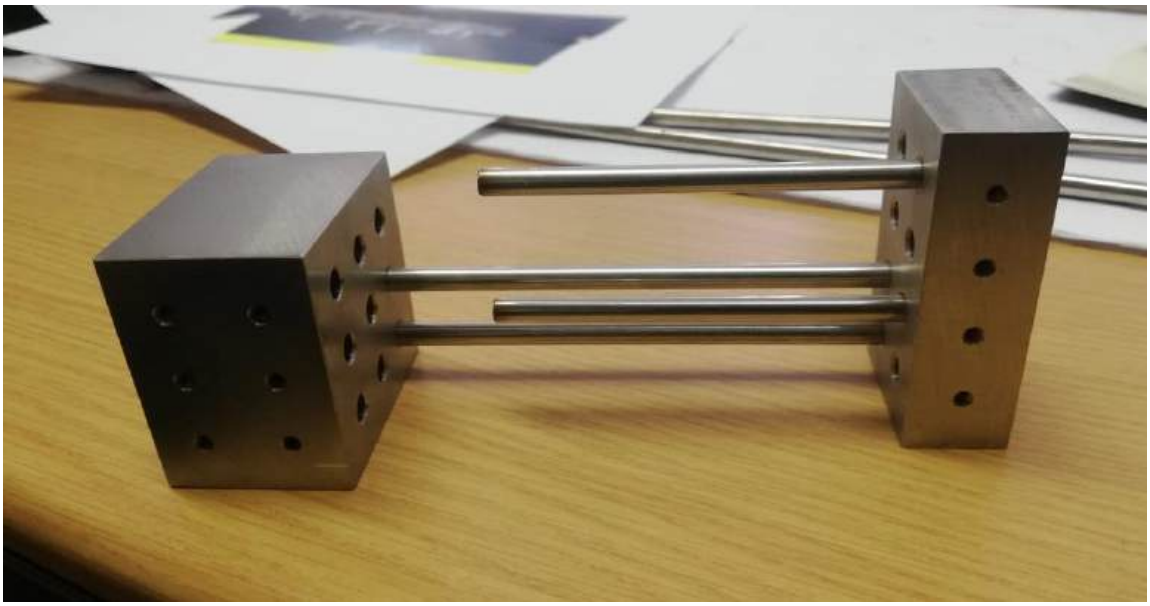

Figure A2.6: A flow cell design incorporating the block designs and a rod

References

[1] D. O'Nolan, G. Huang, G. E. Kamma, A. Grenier, C.-H. Liu, P. K. Todd, A. Wustrow, G. T. Tran, D. Montiel, J. R. Nelson, S. J. L. Billinge, P. J. Chupas, K. S. Thornton and K. W. Chapma, "A thermal-gradient approach to variable temperature measurements resolved in space," *Journal of Applied Crystallography,* pp. 1-9, 2020.